Wide-Bandgap Integrated Photonics for Quantum Technologies

by

Tsung-Ju Jeff Lu

B.S., California Institute of Technology (2013)
S.M., Massachusetts Institute of Technology (2015)

Submitted to the Department of Electrical Engineering and Computer Science
in partial fulfillment of the requirements for the degree of

Doctor of Philosophy

at the

MASSACHUSETTS INSTITUTE OF TECHNOLOGY

September 2020

Author .....
Department of Electrical Engineering and Computer Science
August 28, 2020

Certified by .....
Dirk R. Englund
Associate Professor of Electrical Engineering and Computer Science
Thesis Supervisor

Accepted by .....
Leslie A. Kolodziejski
Professor of Electrical Engineering and Computer Science
Chair, Department Committee on Graduate Students

Wide-Bandgap Integrated Photonics for Quantum Technologies

by

Tsung-Ju Jeff Lu

Submitted to the Department of Electrical Engineering and Computer Science
on August 28, 2020, in partial fulfillment of the
requirements for the degree of
Doctor of Philosophy

Abstract

Development of quantum networks is necessary for quantum communication and distributed quantum computing. This requires the distribution of entanglement across many stationary qubits in the network. Solid state defect quantum emitters (QEs) can function as light-matter interfaces for connecting the internal electron spin states acting as stationary qubits and quantum states of emitted photonic qubits. Entanglement can then be generated between distant spin qubits by heralded optical measurements of the emitted photons over fibers. Thus, a key challenge is the control of many QEs, as well as efficient routing and detection of the spin-state-dependent photons. With QEs being in solid-state, we can achieve the scaling needed through miniaturization of the control and routing components by using integrated electronics and photonics. However, advanced and commonly-used integrated photonic platforms produced in foundries are based on silicon and silicon nitride, which are incompatible with the short wavelength emission of leading solid-state QEs. As such, there is a need for a wide-bandgap integrated photonics platform for quantum technologies.

This thesis first develops photonic integrated circuits (PICs) based on aluminum nitride (AlN) on sapphire, which enables low-loss routing from the visible down to the ultraviolet spectrum. We will then show that thin film AlN is also host to bright, high-purity QEs compatible with monolithic PIC integration. As solid-state emitters in diamond are among the promising qubits for quantum networks due to their efficient optical interfaces and minute-scale spin coherence, we will then present on the large-scale heterogeneous assembly of diamond-waveguide-coupled QEs into AlN photonic circuits with *in situ* wavelength tuning. To demonstrate the versatility of this photonics platform, we will lastly discuss the heterogeneous integration of QEs in 2D materials and detectors. These advances show that AlN is a promising and versatile wide-bandgap integrated photonics platform for quantum information processing.

Thesis Supervisor: Dirk R. Englund
Title: Associate Professor of Electrical Engineering and Computer Science

Acknowledgments

There are many people I would like to thank who made this thesis possible:

I would like to thank my advisor, Professor Dirk Englund, for his guidance, mentorship, and support. It has been a privilege to work with him and always being able to ask him for advice on anything. I am thankful for the opportunity to be involved in many projects that allowed me to explore and grow my scientific interests, as well as develop my skills as a scientist. Seeing him maintain his work ethic, constantly working hard even on weekends and holidays, motivated me to work just as hard.

I would also like to thank Professor Karl Berggren for being on my thesis committee and for the projects we completed together that are part of this thesis. I started collaborating with Professor Berggren since the start of my PhD. For our first collaboration in which we were developing a SNSPD fiber array, he even took the time to work with me personally in the cleanroom and building a projection lithography system. I am beyond thankful and will always remember his direct teaching during my first semester, as well as his mentorship throughout my time at MIT.

I would also like to thank Professor Tomás Palacios for being a member of my thesis committee, my academic advisor, and a wonderful collaborator for my research projects. Professor Palacios' professionalism and ability to be super organized despite managing and leading many things is something I strive to emulate. I am thankful for his expertise and knowledge in AlN and other III-nitride materials that have been integral for my thesis. Lastly, I would like to thank him for making sure that I am on track in my graduate studies and giving me advice on my career.

Next, I would like to express my gratitude for Janice Balzer, David Barnett, Joseph Baylon, Lara Ranieri, and Dorothy Fleischer for their administrative support that have made it possible for everything to progress smoothly during my PhD.

In addition, I would like to thank Jim Daley of the NanoStructures Laboratory for his help and expertise in fabrication, as well as his friendship and constant cheerfulness that never failed to make my day in the cleanroom much brighter. I would also like to thank Eric Lim, Dave Terry, Bob Bicchieri, and the rest of Microsystems Technology

Laboratories for all their help and expertise in fabrication. I would like to thank Mark Mondol for working around the clock to maintain the EBL facilities, as well as being super helpful in debugging any issues regarding e-beam lithography. Developing a reliable fabrication process was a difficult yet essential part in this thesis, so I am grateful to all these people for helping me with this.

I would also like to thank everyone in the Quantum Photonics Laboratory and Quantum Nanostructures and Nanofabrication Group for their help in everything. It was amazing to work with this group of highly intelligent and extremely motivated academics. I particularly want to thank Hyeongrak Choi, Di Zhu, Benjamin Lienhard, Sara Mouradian, and Noel Wan, whom I had the privilege to work with closely on the projects that I will be highlighting in my thesis. It was lots of fun working with them, and I am grateful for their friendships as well. Special thanks to Darius Bunandar, Cheng Peng, Catherine Lee, Jiabao Zheng, Laura Kim, and Kevin Chen for their friendship, help, and advice on various things over the years.

I will also like to thank my wonderful collaborators from Professor Stefan Preble's group at Rochester Institute of Technology and Professor Igor Aharonovich's group at University of Technology Sydney. I would also like to thank Edward Bielejec at Sandia National Laboratories for leading the diamond implantation efforts.

Finally, I would like to thank the people dear to my heart who have been there for me every step of the way, supporting and loving me no matter what. My close group of friends from college –Philip Kong, Arpit Panda, Marvin Gee, Tony Wu, and Chan-Hee Koh– who always brighten up my day with our group chat conversations, offer me advice on anything, and support me through the thick and thin. I am so fortunate to have brothers like them. Lastly and most importantly, I would like to express my utmost gratitude to my mother and father for their love, care, and unconditional support. There is no way I could be where I am in life without them, so this thesis is dedicated to them.

Contents

List of Figures

List of Tables

Chapter 1

Introduction

1.1 Quantum Networks for Quantum Communication and Distributed Quantum Computing

The central challenge in building long-range quantum networks for scalable quantum computing and quantum communication is to distribute entanglement across multiple, individually controllable, quantum memories [1]. One way to experimentally implement this is to connect stationary spin qubit nodes with photonic flying qubits, which are ideal long distance carriers of quantum information that are resistant to decoherence [2]. This requires the development of a light-matter quantum interface that connects the quantum states of photonic qubits to the stationary qubit states of each quantum node. For this, each node would consist of a quantum memory whose register has several ancillary qubits for single qubit and two-qubit gates. Furthermore, having multiple physical ancilla qubits in each node also allows for quantum error correction [3]. With these components, each node functions as a quantum information processor. Then, to entangle two distant stationary spin qubits, we would need spin-state-dependent photon scattering from the two memories. The photons will then be interfered on a beamsplitter that removes information regarding the origin of the scattered photons if the photons are indistinguishable, which means that their wavelength, linewidth, and polarization are identical. Finally, photon detection

collapses the quantum states of the two spin qubits into a non-local quantum superposition, or entangled state. In order to create a quantum network that distributes these quantum entangled states, the main difficulty is to achieve coherent control over the interactions of light and matter at the single-photon level for hundreds and even thousands of qubits across multiple nodes.

1.2 Solid State Integrated Platforms for Scalable Quantum Network Hardware

Atomic systems such as trapped ions and neutral atoms have previously led the way for building such a distributed quantum network due to their exceptional coherence times and optical properties. While proof-of-concept experiments are possible with today's optical components using trapped atoms and ions [4, 5], scaling these systems to tens, hundreds, or thousands of individually controllable quantum memories requires electronic and photonic hardware at very large scales. On the other hand, solid-state quantum emitters have properties resembling those of atoms and ions but do not need to be trapped as they are naturally trapped through a potential created by the semiconductor host environment. Hence, they are promising for building these light-matter interfaces in a scalable and compact hardware using semiconductor engineering and manufacturing. The way these 'artificial atom' quantum emitters function is that a quantum register of electron spin in the solid interacts with nearby nuclear spins in the lattice to provide high-fidelity state manipulation and readout, long-lived quantum memory, and long-distance transmission of quantum states by optical transitions that coherently connect the electron spins and emitted photons. Each quantum emitter is the engine for distributing and processing entanglement between distant stationary nodes in a quantum network.

Atomic color centers in diamond have been shown to have efficient spin-photon interfaces [6] with minute-scale quantum memory times [7], which have allowed them to emerge as leading candidates amongst solid-state atom-like qubits. They have enabled

large-distance quantum networks with demonstration of loophole-free Bell inequality violation between two diamond emitters separated by 1.3 kilometers [8]. In fact, diamond quantum emitters have also recently broken the entanglement rate threshold, making it possible to create entanglement faster than the decoherence time, which is a significant breakthrough for potentially scaling up quantum networks beyond the previous limit of just two remote defect centers [9]. Furthermore, they have recently been used for memory-enhanced quantum communication, enabling quantum communication at a rate that surpasses the ideal loss-equivalent of direct-transmission [10]. The goal now is to develop quantum information processing (QIP) architectures to combine these quantum memories into scalable hardware for applications ranging from multiplexed quantum repeaters [11, 12] to general-purpose quantum computers [13–15]. To do so, we would need to heavily rely on the solid-state aspect of these quantum emitters in diamond to scale these systems beyond the two nodes demonstrated in proof-of-concept experiments so far.

Modern digital computing technologies have developed through constant miniaturization that enables more efficiency and complexity over time. What was once a large, bulky reconfigurable general-purpose digital computer made of vacuum tubes that took up an entire room (Electronic Numerical Integrator and Computer - ENIAC) has transformed into the small and ultra-compact semiconductor computing chips that we have today that are many orders of magnitude more powerful than its predecessor. This was made possible by the invention of solid-state transistors that allowed us to translate bulky computers into an integrated platform. Similarly, the ground-breaking proof-of-concept quantum experiments have mainly involved super complex and large optical setups. While properties like superposition and entanglement make qubits powerful, these properties are also fragile and require phase and amplitude stability for the entire system, making scaling with bulk optics intractable. Motivated by the progress of the semiconductor industry, our goal is to develop solid-state quantum emitters and semiconductor integrated photonics and electronics to miniaturize the functionalities of these bulky setups to a compact chip for scalable quantum technologies capable of controlling, processing, and routing hundreds, thou-

sands, and eventually millions of qubits on a single chip. An integrated platform using nanofabricated photonic components may eliminate bulky free-space optics altogether while greatly reducing optical losses, greatly improving component density, and providing phase stability. Furthermore, an integrated system can be packaged to reduce environmental fluctuations from affecting the quantum states.

1.3 Atomic Defect Centers in Diamond

In order to determine what has to be developed in an integrated hardware for quantum information processors using solid state quantum emitters, we have to understand what their properties are. The intent is for this work to be applicable universally to any quantum emitter because quantum emitter research is a burgeoning field with new promising platforms constantly being discovered that may one day be what is used for quantum information processing. However, we will discuss the spin and optical properties of these leading 'artificial atoms' in diamond and use them for the demonstrations in this thesis.

1.3.1 NV Centers in Diamond

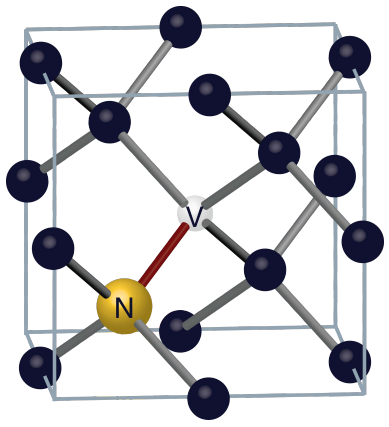

Figure 1-1: Schematic of the nitrogen vacancy center in the diamond lattice.

Amongst the atomic defect centers in diamond, the negatively charged nitrogen vacancy (NV) center in diamond has been the most extensively studied and most

used color center for quantum network architecture demonstrations. The NV center consists of a substitutional nitrogen in a carbon lattice site and vacancy in an adjacent site (Figure 1-1). In the negatively charged state, there are a total of six electrons trapped in the defect, comprised of three electrons covalently bonded to the three adjacent carbons, two unbonded electrons from the nitrogen, and one electron from the diamond lattice conduction band. It is a $S = 1$ system with spin triplet ground state, spin triplet excited state, and long-lived singlet state. Considering spin-spin interaction and spin-orbit interaction, these become a spin-triplet, orbital singlet ground state that can be coupled optically to a spin-triplet, orbital-doublet excited state, with distinct spin-selective, zero-phonon optical transitions resolvable at cryogenic temperatures [16]. The optically addressable spin ground state and excited state levels are then used for storing quantum information [17]. Its electronic spin can be used to mediate coupling to local quantum registers composed of several nuclear spins by hyperfine interaction [7] while also coupling coherently to photonic qubits, essentially acting as a small quantum information processor. NV centers have even been used to demonstrate spin coherence times exceeding 1 second at room temperature [18]. With these properties, most of the proof-of-concept quantum network experiments have been demonstrated using NV centers in diamond. However, only about 3% of the NV's fluorescence is emitted through the zero-phonon line at around 637 nm that coherently couples to the electronic states. The rest of the fluorescence result from decay from the NV excited state that loses energy to the diamond lattice due to excitation of vibrational modes. This results in a broad emission spectrum known as the phonon sideband. These transitions lose information to the diamond lattice, so they do not hold information about the electron spin state and cannot be used for entanglement generation.

Previous demonstrations of entanglement with spin states of spatially separated NV centers in diamond used the Barrett and Kok protocol [19]. In this protocol, both NV centers have to each emit a photon that is entangled with the electronic state. Then, both photons are interfered on a beamsplitter, followed by detections of the photonic state. Detection of exactly one photon projects the two spins into an

entangled state. Then, the entangled state is verified in a following trial by flipping both NV spins and detecting a second single photon, leading the success probability to scale proportionally with the square of the photon-to-detector collection efficiency. This is made worse by the fact that optical fiber links are more lossy in the visible wavelengths that NV centers emit compared to the typical low-loss telecom wavelengths. As such, to extend the spin-photon quantum network to beyond just two NVs would require significant improvements to the spin-photon interface through optical cavities to achieve strong Purcell enhancement [20]. However, this requires precise positional and spectral overlap of the NV with the cavity, leading to even less tolerance and yield in the manufacturing. As such, it may be more straightforward and less of an engineering challenge to find new quantum emitters with inherent spin and optical properties that are more suitable for quantum network applications.

1.3.2 Group IV Color Centers in Diamond

New color centers in diamond, such as the negatively charged silicon vacancy (SiV) and the negatively charged germanium vacancy (GeV) centers, have drawn attention in recent years due to their much larger Debye-Waller factor ($\sim$0.7), which is the fraction of emission emitted into the zero-phonon line. Being structurally-similar defects, SiV and GeV are formed by replacing two neighboring carbon atoms in the diamond lattice with one silicon or one germanium atom, respectively, which situates itself between the two vacant carbon lattice sites. The SiV center is a spin-1/2 system with the electron ground and excited states each having double orbital degeneracy split by spin-orbit coupling and dynamic Jahn-Teller interaction. This results in a pair of split ground and excited states, with the spin-orbit states each doubly degenerate by spin [21]. These eigenstates have optical and phononic transitions that couple only to the orbital degree of freedom and are spin conserving, making it possible to control the defect's spin states by all-optical methods. These spin states also have near-unity spin purity and allow for spin-dependent resonance fluorescence measurement [22], making SIV an excellent spin-photon interface. As the ground and excited states are located within the diamond bandgap, all four transitions between the two ground and

two excited orbital states result in a sharp zero-phonon line at 737 nm. The GeV center has spin and optical properties similar to that of SiV center, with the exception of having its zero-phonon line at 602 nm.

SiV and GeV have lower spectral diffusion due to their D_{3d} point group inversion symmetry that results in highly indistinguishable photon emission with narrow near-transform-limited optical linewidths, which combined with their shorter radiative lifetime and bright photoluminescence, make them ideal for photon-mediated entanglement generation. However, SiV and GeV have short spin coherence times that require them to be operated at mK temperatures [23, 24] or strained to increase the energy splitting of the orbitals [25]. Further studies are being done with SiV, GeV, and other group IV vacancies in diamond to learn how to control and operate them to have higher spin coherence times and coupling to ancilla qubits. However, with the achieved spin coherence times, SiVs have already been used to couple to nearby ^{13}C that can serve as ancilla qubits [26] for quantum memories, gate operations, and error correction.

Due to their optical properties of strong emission into the spin-correlated zero-phonon line, low inhomogeneous distribution, and low spectral diffusion, SiV and GeV are gaining interests for use in quantum networks. Another advantage of SiV and GeV is that they have been shown to maintain their highly coherent optical transitions even when produced through ion implantation [27], unlike NV centers [28], which is important if we want to integrate a single SiV or GeV into a cavity with high positional and spectral overlap. The remaining challenge is to engineer and find ways to control the spin properties of SiV and GeV to be comparable to that of NV centers. There have also been investigations of other group IV defects in diamond in the past year or two, with the expectation of having similar optical properties as SiV and GeV centers due to having the same inversion symmetry and hopes of possibly having spin properties comparable to that of NV centers [29, 30].

1.4 Components for Integrated Quantum Photonics

With so many early pioneering works for using solid-state quantum emitters for quantum networks, what is left now is to scale everything up. Integrated photonics is a promising avenue for reaching the scale of component integration while maintaining performance necessary for quantum information processing through nanofabrication techniques. For this, on-chip entanglement would be necessary with it being imperative to improve the efficiency with which single photons from quantum emitters can be guided into low-loss single-mode waveguides and detected with single photon detectors. Having the capability to perform on-chip entanglement of photons from separate quantum memories would be the basis of building up a multiplexed quantum repeater necessary for quantum networks. A similar architecture can also be used for local quantum information processing.

With 'artificial atoms' in solid state being a key component for integrated quantum photonics, there are many components/functionalities necessary for a full-fledged quantum photonic system that can be used for both building quantum networks and for performing quantum information processing. For example, on-demand single photon sources, filters, and reconfigurable optical circuits comprised of beamsplitters and phase shifters are necessary for linear optic quantum computation and teleportation [31]. The system also requires integrated detectors for efficient state measurements, with which the output electrical signals can be routed to fast electro-optic modulators to perform feed-forward operations. A quantum state storage unit can be composed of an atomic color center quantum memory. In addition, for interfacing with another system or node separated by long distances via an optical fiber, it may be necessary to have wavelength conversion elements using optical nonlinearities. This can also be used for interfacing with different types of emitters to overlap their wavelengths. Single-photon nonlinearities are also necessary for photon-photon interaction and deterministic quantum gates. Finally, we would require large-scale control electronics that would inevitably necessitate fast CMOS logic.

1.5 Hybrid Integration for Quantum Photonics

Impurity spins will satisfy the functionalities of on-demand single-photon sources, photon memories, and nonlinear single-photon switches in an integrated quantum photonics processor, playing the role similar to that of transistors in driving miniaturization while maintaining necessary operations. In order to minimize manufacturing complexities and optical loss in coupling from one component to another, ideally a quantum emitter would be embedded in a material platform that enables stable spin and optical properties, as well as a robust manufacturing of photonic circuits. However, the variety and extent of building blocks suggests that existing integrated photonic components based on a single material platform may be inadequate to build a quantum photonic system. For example, while quantum emitters in diamond are the leading solid-state emitters with long coherence times, with individual diamond cavity systems coupled to artificial atoms now achieving excellent performance, there is no active chip-integrated diamond photonic components and wafer-scale single crystal diamond on a low-index substrate for on-chip photon routing, modulation, and switching in an all-diamond system, which currently prohibits scaling to large scale QIP applications [12–15]. Furthermore, yield becomes an issue when trying to manufacture a large-scale system if some of the building blocks are prone to fabrication non-uniformity or imperfections. One or more faulty components can compromise the capabilities of the whole chip. To date, efforts towards large-scale QIP with color centers in diamond as the core component have been stymied by qubit inhomogeneities, low device yield, and complex device requirements.

A promising method to alleviate these constraints is heterogeneous (or hybrid) integration, which is increasingly used in advanced microelectronics to assemble separately fabricated sub-components into a single, multifunctional chip. In heterogeneous integration, the building blocks of the system are first separately fabricated in materials typically incompatible for direct growth, then they are prescreened and combined in a transfer process. Doing so maximizes the yield, size, and performance of the hybrid chip by combining the best properties of each constituent platform while

circumventing the limitations of each. Heterogeneous integration approaches have also recently been used to integrate photonic integrated circuits (PICs) with quantum devices, including quantum dot single-photon sources [32, 33], superconducting nanowire single-photon detectors [34], and nitrogen-vacancy (NV) center diamond waveguides [35].

The glue that holds everything together is, therefore, an underlying photonic integrated circuit that serves as a backbone carrier to host and connect all the separate components. To harness the potential of quantum phenomena on a large scale, we would need to combine post-selection of only functional quantum components that typically suffer from low production yield with a mature, highly-developed foundry-based photonic integrated circuit technology with high throughput and yield, compatible with CMOS electronics for high speed control, logic, and processing. In fact, the most advanced integrated photonic platforms today are based on silicon or silicon nitride (SiN) that can be produced in existing CMOS foundries.

1.6 Photonic-Integrated Quantum Memories and Photonic Integrated Circuit Platforms

For the application of quantum networks, the most important component is the integration of quantum emitters with long-lived quantum memories since it is what drives everything that we need for remote entanglement. There have been many advances in the hybrid approach involving the integration of quantum emitters with various photonic platforms. For example, there have been demonstrations showing quantum dot quantum memories integrated with advanced photonic platforms using silicon or SiN [32, 36]. However, the spin properties of these quantum memories emitting in the near infrared are poor with short coherence times. There have also been demonstrations of hybrid integration of quantum emitters and atomic quantum memories with many orders of magnitude longer coherence times [35, 37, 38]. However, they have important optical transitions in the ultraviolet (UV) and visible wavelengths in which

the photonic platforms used (SiN and GaP) are less developed, less studied, lossy, or have unwanted high intensity, broad background autofluorescence. The trend seems to be that the higher the coherence time of the quantum memory, the shorter the wavelength of the optical transitions. As such, there is a need to develop a low-loss UV to visible integrated photonics platform that can be leveraged to interface with these leading long-lived quantum memories for scalable quantum technologies.

There are also recent interests of other optically active spins in rare-earth ion dopants in a solid state host, such as Er^{3+} and Yb^{3+} [39, 40], with emission wavelengths in the near-infrared and infrared range. With new quantum technologies emerging constantly, it would be ideal to develop a wide-bandgap photonics platform that would span from UV to infrared so that multiple technologies can potentially be interfaced together on one chip.

1.7 Thesis Motivation and Overview

Integrated photonics confine and propagate light using the same principles as optical fibers, specifically total internal reflection due to the refractive index differences between the higher index core and lower index cladding. For stronger light confinement, which results in higher device densities and smaller footprints, the differences in the refractive indices would need to be higher. Gathering inspiration from the most-advanced existing integrated photonics technology based on silicon-on-insulator (SOI), we want to choose a material platform with an existing industrial base with mature nanofabrication and growth technologies that can be readily leveraged for scaling, so that it would be possible to quickly go from the research development state to commercial viability. For this, we choose III-nitride, specifically aluminum nitride (AlN), which is one of the widest bandgap semiconductors with transparency from 200 nm to 15,000 nm with sophisticated manufacturing driven by large and growing applications in optoelectronics, high voltage power transistors, and microwave amplifiers. AlN also has many great material properties that allow for active photonic devices and methods for quantum emitter control.

With AlN having a refractive index n_{AlN} of around 2.1, we would need to choose a substrate with refractive index smaller than that for light confinement and waveguiding. For the low index substrate, we choose sapphire with $n_{\mathrm{sapphire}} \approx 1.7$, which has an extremely large bandgap of 8.8 eV that has low optical loss from 200 nm to 5000 nm. Another key aspect for this choice of sapphire is that it is one of the most commonly-used substrates for heteroepitaxy of AlN due to the 13% lattice mismatch in the c-plane between AlN and sapphire [41]. 6H-SiC is another commonly-used substrate for heteroepitaxy of AlN with an even smaller lattice mismatch for the c-plane of $< 1\%$ [42], which would lead to a much better crystal quality of the AlN. However, the refractive index of SiC ($n_{\mathrm{6H-SiC}} \approx 2.6$) is much higher than that of AlN.

Figure 1-2 shows a concept overview of the quantum repeater hardware for building a quantum network that would be based on our AlN photonic integrated circuit platform. Ultimately, we imagine the AlN-on-sapphire chip to have a dynamic photonic routing circuit that is composed of an optical mesh of cascaded tunable Mach-Zehnder interferometers with phase shifters for accurately tuning the output splitting, which can be used to interfere any two of the quantum emitters on the chip. These phase shifters are also necessary to help compensate for fabrication imperfections that affect the splitting ratios of a directional coupler beamsplitter. This programmable nanophotonic processor can also be used to implement any arbitrary unitary optical transformations. This chip will also contain electrical wires for qubit spin control. Finally, it would also have on-chip single photon detectors, or it can even be interfaced off-chip with edge couplers to connect to other chips or quantum nodes.

Chapter 2 of this thesis will present on the development of a new integrated photonics platform based on AlN-on-sapphire for the UV to visible spectrum. We will demonstrate low autofluorescence and low defect density in the material platform, as well as low propagation loss in the UV and visible spectrum. Then, we will show the capability to fabricate various essential photonic devices for integrated quantum photonic processes, such as grating couplers, edge couplers, ring resonators, distributed Bragg reflectors, and directional couplers.

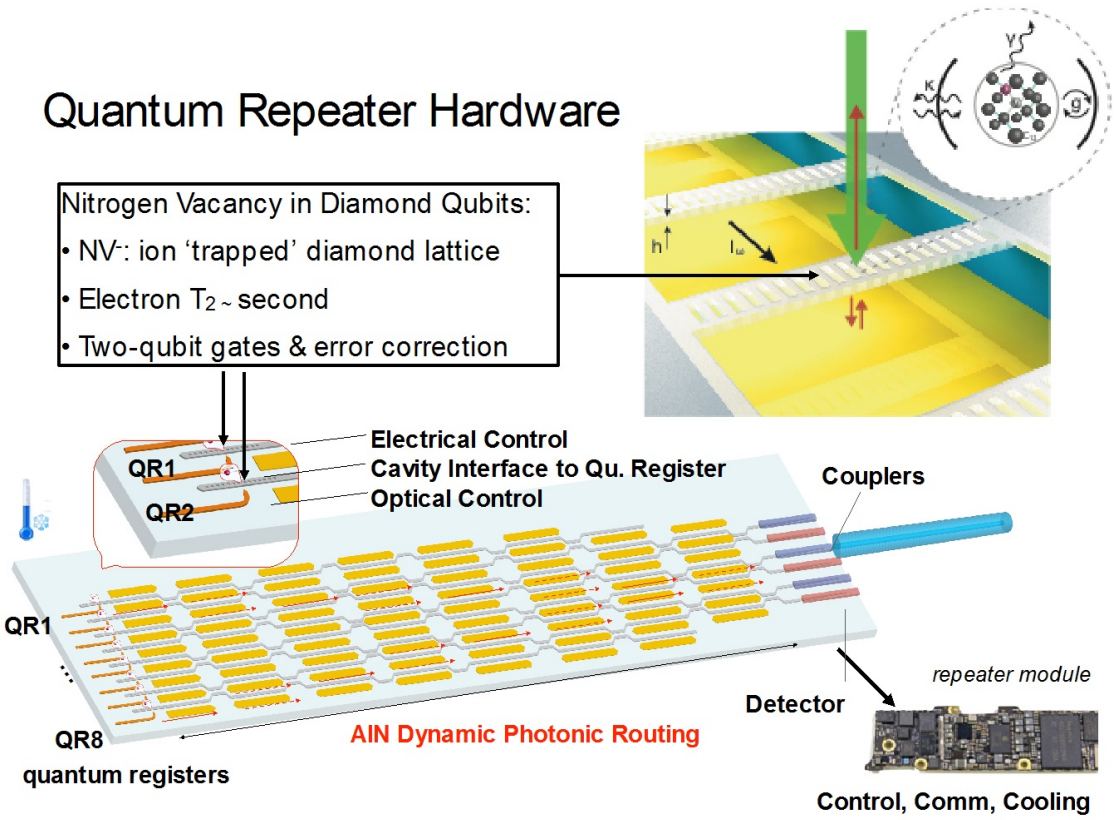

Figure 1-2: Overview of quantum repeater hardware for building a quantum network, which uses NV centers in diamond as quantum registers. However, this hardware architecture can also be applied to other emerging color centers in diamond or even other semiconductor materials. We will use an AlN photonic integrated circuit for dynamic photonic routing, and SNSPDs as on-chip detectors.

As the promising solid-state single photon emitters to-date are atomic color centers in wide bandgap materials such as diamond, silicon carbide, and hexagonal boron nitride, which cannot be grown as sub-micron thin film on low refractive index substrates necessary for photonic integration, there is great interest in discovering quantum emitters in technologically mature thin film wide-bandgap semiconductors such that the optically active defects would have ground and excited states within the bandgap. AlN is one of the widest bandgap semiconductors and theoretical calculations have shown that AlN can serve as a stable environment for well-isolated single photon emitters with optically accessible spin states [43]. Chapter 3 of this thesis will demonstrate the experimental creation and characterization of high-purity single

photon quantum emitters in thin film AlN grown on top of sapphire. The photophysical properties of these emitters will be presented, as well as integration with photonic integrated circuits patterned from the host AlN material. Although spin and detailed optical linewidth measurements are left for future work, these results already show the potential for high-quality QEs monolithically integrated in a wide range of III-nitride device technologies that would enable new quantum device opportunities and industrial scalability.

Chapter 4 shifts the focus to utilizing this AlN photonics platform for the better-studied and leading solid-state quantum memories in diamond. As mentioned previously, heterogeneous integration is recognized as a scalable path to building a large quantum network because one can in principle combine post-selection of qubits with a foundry-based PIC technology. However, previous demonstrations assembled components one-by-one, which presents a formidable scaling challenge. To date, no such hybrid technologies have been achieved beyond the standard 2-5 qubit per chip. Here, we will demonstrate a process for the high-yield heterogeneous integration of large-scale, easily-transferable arrays of diamond nanobeams containing highly coherent color centers onto a backbone of large-scale AlN integrated photonic circuitry, which can be equipped with electrical lines for qubit control. This process is used to realize a 128-channel, defect-free array of germanium-vacancy and silicon-vacancy color centers in an aluminum nitride PIC. The inhomogeneities of individual color center optical transitions can be compensated *in situ* by integrated tuning without linewidth degradation. The ability to assemble large numbers of nearly indistinguishable and tunable artificial atoms into phase-stable PICs marks a key step towards multiplexed quantum repeaters and general-purpose quantum processors.

In Chapter 5, I will also show that this photonics platform can be extended to emerging ultrabright, highly pure on-demand single-photon emitters in 2D materials, particularly room temperature quantum emitters in layered hBN. I will also show fabrication of niobium nitride single-photon detectors on AlN substrates, as well as an architecture for multi-photon coincidence detection for use in a large-scale photonic system, which sets the groundworks for waveguide-integrated detectors onto

this scalable platform.

Finally, in Chapter 6, I will give concluding remarks and perspectives on future directions.

Chapter 2

Aluminum Nitride-on-Sapphire Integrated Photonics

Materials presented in this chapter have been previously published, and the text in this chapter is reproduced from this publication (Optics Express **26** (9), 11147-11160 (2018) [44]).

2.1 Background and Properties of AlN

Aluminum nitride (AlN) is one of the widest bandgap (6.015 eV, ∼205 nm) semiconductors with attractive electronic and photonic properties, including transparency into the ultraviolet (UV) regime (365 nm wavelength and shorter). This broad spectrum makes it attractive for applications including UV spectroscopy [45, 46], optical waveguides for modular quantum computing with atomic memories [13, 47–50], nonlinear photonics throughout the UV to infrared [51], and solar-blind communications [46]. Many atomic transitions are in the UV or visible (VIS) spectrum, including Ytterbium ions ($^{171}Yb^{+}$), Strontium ions ($^{88}Sr^{+}$), Barium ions ($^{138}Ba^{+}$), and nitrogen vacancy (NV) centers in diamond, which have important optical transitions at 369.5 nm, 422 nm, 650 nm, and 637 nm, respectively. Recent work demonstrates the utility of integrated optics to perform quantum coherent operations on the optical qubit transition of $^{88}Sr^{+}$ at 647 nm [38]; the UV transmission of AlN-on-sapphire

would also enable $^{88}Sr^{+}$ initialization at 422 nm or driving the 369.5 nm wavelength of $^{171}Yb^{+}$. Autofluorescence of silicon nitride (SiN) presents a challenge for pumping the diamond NV center at 532 nm [35]; this autofluorescence is greatly reduced in AlN-on-sapphire, opening the path to large-scale photonic integrated circuits for atom-like qubits in diamond.

Electro-optic modulation presents an important capability in many applications, such as architectures for modular quantum computing. AlN has a relatively large electro-optic coefficient, and fast electro-optic modulation (∼4.5 Gb/s) has been demonstrated with AlN's high c-axis electro-optic coefficient (r_{33} = 1 pm/V) using sputtered AlN [52]. Piezo-electric actuation of photonic devices has also been shown with optomechanical resonators [53] and can potentially achieve very high modulation depth [54]. Lastly, AlN has a high second order nonlinear susceptibility $\chi^{(2)}$ (4.7 pm/V) [55, 56], as well as a third order nonlinear susceptibility with Kerr coefficient comparable to that of stoichiometric SiN (the n_2 for transverse electric waveguide mode in the (001) plane is estimated to be $(2.3 \pm 1.5) \times 10^{-15}$ cm^2/W) [57]. These nonlinear properties allow for a number of nonlinear optical processes [58–60], including second harmonic generation [55, 61], sum/difference frequency generation [62], photon pair generation by spontaneous parametric down conversion [63], and four-wave mixing [57, 64]. The combination of the large bandgap with these nonlinear and electro-optic properties make AlN a promising platform for quantum devices and for other high-performance optics applications.

Here, we present an UV/VIS photonics platform based on AlN grown by plasma vapor deposition of nanocolumns on a sapphire substrate. X-ray diffraction shows low defect densities, which will help minimize propagation loss. We demonstrate essential photonic devices including ring resonators, distributed Bragg reflectors, and directional couplers. We show ring resonators with high intrinsic quality factor (Q) in visible ($Q \sim$ 170k, loss $\sim$ 5.3 dB/cm at 638 nm) and record-high quality factor in UV ($Q \sim$ 20k, loss $\sim$ 75 dB/cm at 369.5 nm). We demonstrate both vertical and edge coupling and compare them with simulation results. While autofluorescence is a problem in materials such as SiN, we find it to be low in the AlN on sapphire

platform.

2.2 Material Analysis of AlN-on-Sapphire

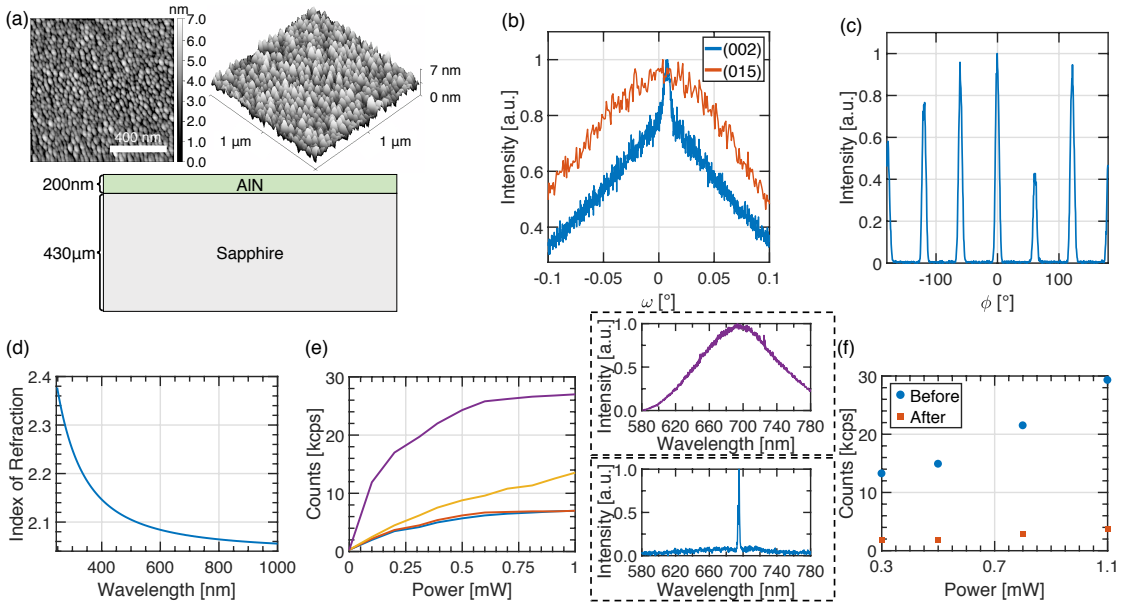

Figure 2-1: Properties of AlN-on-sapphire material. (a) Cross section illustrating each layer of the wafer, along with their respective thickness; top inset: atomic force microscopy scan of AlN film showing the nanocolumn size. Surface roughness is measured to be 0.9 nm RMS with 26.5 nm grain size (b) High resolution x-ray diffraction (002) and (015) ω scan of AlN. (c) (015) ϕ scan of AlN showing six-fold symmetry wurtzite structure. (d) Refractive index measurements using ellipsometry. (e) Background fluorescence from sapphire substrate (yellow), unpatterned AlN (blue), patterned AlN (orange), and stoichiometric silicon nitride (purple). Top inset (purple): Fluorescence spectrum of SiN. Bottom inset (blue): Fluorescence spectrum of AlN. (f) Background fluorescence from SiON top cladding, before (blue circles) and after (orange squares) bleaching.

Figure 2-1a illustrates the commercially available AlN-on-Sapphire wafers from Kyma Technologies, Inc., consisting of 430 µm sapphire (Al_2O_3) with a 200 $\pm$ 10 nm c-plane AlN film on the top layer, which is used for fabricating photonic integrated circuits (PICs) in this work. The c-plane AlN is grown on top of the sapphire substrate by pulsed DC magnetron sputtering, using a process called plasma vapor deposition of nanocolumns (PVDNC^{TM}). This method produces an AlN thin film that is crystalline with the [0001] direction parallel to the growth direction. Atomic force microscopy of

the AlN thin film shown in the inset of Figure 2-1a indicates a flat surface with 0.9 nm RMS roughness. High-resolution X-ray diffraction (HRXRD) measurements in Figure 2-1b indicate the high structural quality of the AlN thin film. The ω scan of (002) and (015) AlN peaks shows full-width-half-maximum (FWHM) of 0.12 degree and 0.20 degree respectively, while previous work of AlN thin films deposited on amorphous silica reported a FWHM of the XRD rocking curve to be less than 2 degrees with a 1 degree FWHM resolution limit in their system [65]. The single crystalline wurtzite structure across the wafer is evidenced by the (015) ϕ scan showing six-fold symmetry [Figure 2-1c]. This flat surface and improved structural quality likely contribute to the low waveguide loss described below. Figure 2-1d plots the measured refractive index of the AlN film spanning from UV to VIS to near infrared wavelengths.

Figure 2-1e shows the power dependence of this platform's background autofluorescence using a scanning confocal microscope with a $\lambda = 532$ nm excitation pump laser (Coherent Verdi). A 0.95 numerical aperture (NA) microscope objective (Olympus UMPlanFl 100x) is used for the scanning confocal microscope, and a 532 nm notch filter as well as a 550 nm long-pass filter are used to filter out the 532 nm excitation pump in the fluorescence collection path. The photoluminescence (PL) is then fiber-coupled from free-space to a single-mode fiber via a 0.4 NA microscope objective (Olympus MA 20). The fiber-collected PL signal is either detected using single-photon avalanche photodiodes (Excelitas) or spectrally resolved on a grating spectrometer (Princeton Instruments, Acton SP2500i). We are using the 4 μm diameter fiber facet as the pinhole for confocal imaging. Since the size of this fiber facet is not matched perfectly to the spot size at the sample plane, we collect a portion of the out-of-focus light. As such, when we measure the AlN autofluorescence, we are also pumping the underlying sapphire that is out-of-focus and collecting a portion of the sapphire PL. This claim is supported by the fluorescence spectrum of the AlN, which is shown in the bottom inset spectrum of Figure 2-1e. The AlN fluorescence spectrum is identical to that of the sapphire (not shown), which is in agreement with the fluorescence spectrum of sapphire found in literature [66]. The narrow luminescence double peaks at around 695 nm correspond to the ruby luminescence from the

$^2E \rightarrow {}^4A_2$ transitions of Cr^{3+} ions that are substitutional in the Al sublattice.

For comparison, Figure 2-1e also shows the autofluorescence results of a SiN sample under the same excitation and collection conditions; the fluorescence spectrum of SiN is also shown in the top inset of Figure 2-1e. The SiN sample has close to four times the amount of fluorescence intensity as AlN; however, the amount of autofluorescence is dependent on the SiN composition and method of deposition [67]. Furthermore, the PL from pumping the AlN is mainly from the underlying sapphire substrate. Spectrally, this sapphire fluorescence is concentrated in a narrow band sapphire Cr line at around 695 nm, which can be easily filtered out by a notch filter. This is more favorable for quantum applications compared to the broadband SiN PL from 620 nm to 780 nm, which overlaps spectrally to NV in diamond spectrum [35]. A low autofluorescence makes AlN promising for interfacing with atomic transitions of ions [68], neutral atoms [69], and atom-like defects in diamond [35]. Ultimately the maximum allowed background count highly depends on the applications and protocol of the experiment. As long as the background fluorescence is optically detuned from the optical transitions of the quantum system one is working with, sufficient filtering can be achieved to improve signal-to-noise ratio.

Initially after deposition, the SiON cladding (to be discussed later) exhibits some fluorescence comparable to SiN, but we found that the SiON fluorescence can be bleached away by optically pumping the material with the excitation laser, as shown in Figure 2-1f. This photobleaching method of the SiON top cladding did not have any effect on the AlN or SiN materials.

2.3 AlN Thin Film Fabrication Process

Figures 2-3, 2-4, and 2-5 demonstrate the various essential optical components, designed for top-cladding with either (i) Poly(methyl methacrylate) (PMMA), which has a refractive index of $n_{PMMA} \approx 1.50$ to 1.49 in the wavelength range of 500 nm to 700 nm, or (ii) silicon oxynitride SiO_xN_y (SiON), with a refractive index matched to the underlying sapphire ($n_{sapphire} \approx 1.76$ to 1.75 in the wavelength range of 360 nm to

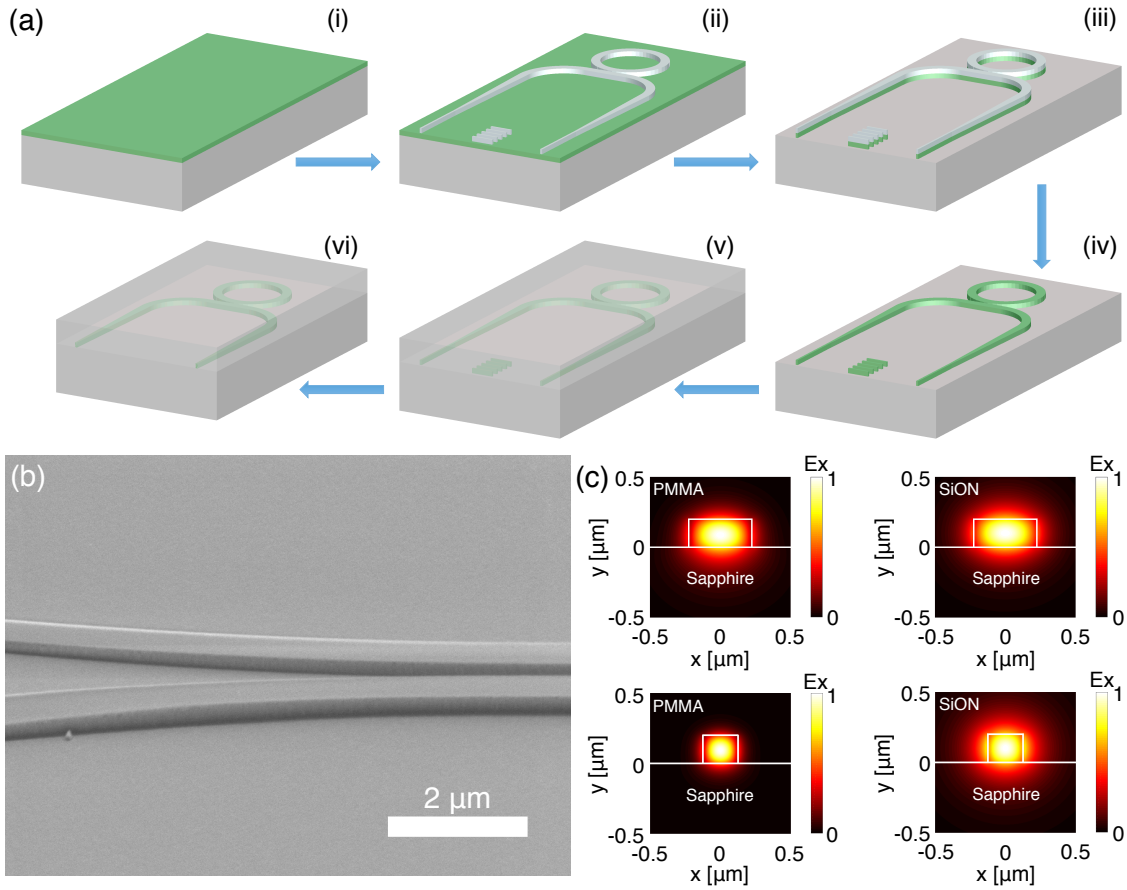

Figure 2-2: (a) AlN on sapphire photonics fabrication process: (i) Start off with an unpatterned AlN-on-sapphire chip diced up from a whole wafer. (ii) Spin coat HSQ (2% XR-1541), pattern using electron beam lithography, and develop using an aqueous mixture of 1 wt % NaOH and 4 wt % NaCl for high contrast. (iii) Etch by ICP-RIE using chlorine chemistry. (iv) Strip HSQ. (v) Clad with silicon oxynitride using plasma-enhanced chemical vapor deposition (PECVD). (vi) Edge polish for making the inverse-tapered edge couplers. (b) Scanning electron microscope (SEM) image of a fabricated AlN waveguide at a 50 degrees tilted view. (c) Transversal component of TE mode in AlN waveguide for PMMA and SiON cladding for 638 nm (top) and 400 nm (bottom) wavelengths. The dimensions of the waveguide for 638 nm wavelength are 450 nm wide × 200 nm thick. The dimensions of the waveguide for 400 nm wavelength are 250 nm wide × 200 nm thick.

480 nm) by adjusting the composition of oxygen and nitrogen to achieve a refractive index between that of silica (1.45) and silicon nitride (2.1). The PMMA cladding is used for the devices and measurements in the VIS wavelength range of 500 nm to 700 nm, while the SION cladding is used for the devices and measurements in the UV wavelength range of 360 nm to 480 nm.

Figure 2-2a outlines the complete fabrication process. The process starts off with an unpatterned 1 cm × 1 cm AlN-on-sapphire chip diced from a whole wafer. Then, hydrogen silsesquioxane (2% XR-1541) is spun on after deposition of a 5 nm thick Cr discharge layer via electron beam evaporation. The hydrogen silsesquioxane (HSQ) film thickness is measured to be ∼70 nm by using an AFM to measure the step feature profile after patterning. The patterns are written with an Elionix ELS-F125 electron beam lithography system at 125 kV. The patterns are developed using a salty developer, which is an aqueous mixture of 1 wt % NaOH and 4 wt % NaCl, for high contrast [70]. The AlN waveguides and photonic components are etched at an etch rate of 200 nm/min by inductively coupled plasma reactive-ion etching (ICP-RIE) using a gas mixture of $BCl_3/Cl_2/Ar$. We do not observe a significant change in the surface roughness from the etching, and a sidewall angle close to 90 degrees is achieved due to the combination of physical sputtering and plasma chemical etching. The $BCl_3/Cl_2/Ar$ chemistry ICP-RIE etch does not result in any noticeable etching of the underlying sapphire substrate. Hence, the underlying sapphire acts as an etch stop layer in which we can overetch the AlN to ensure that it is completely cleared through without creating a sapphire ridge underneath the AlN waveguide structures. The Cr and HSQ are lastly removed with Cr etchant and buffered oxide etch (BOE), respectively. Figure 2-2b shows a scanning electron microscope (SEM) image of the fabricated AlN waveguide. Finally, the waveguides are clad with approximately 3 microns of SION using plasma-enhanced chemical vapor deposition (PECVD) or spin coated with approximately 2 microns of PMMA. In the case where the chip is cladded with SiON, the edges of the chip are mechanically polished back to the inverse-tapered waveguides for edge coupling.

2.4 High Efficiency Off-Chip Coupling Methods

Figure 2-3 highlights two methods to couple light into and from the PIC: grating couplers and inverse-tapered edge couplers. Due to the narrow frequency response of grating couplers, two different grating couplers are used for testing components in the

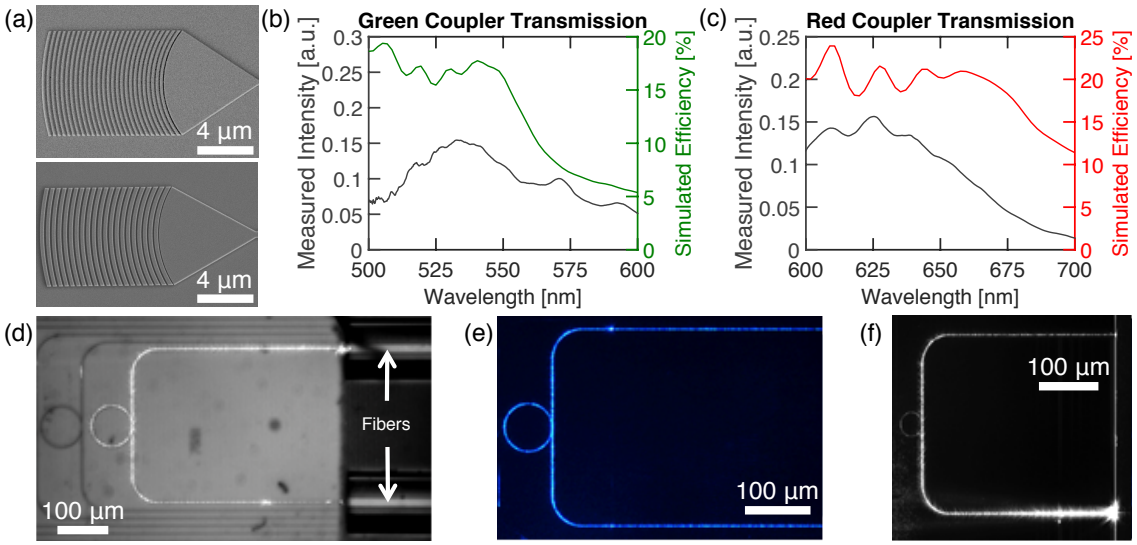

Figure 2-3: (a) SEM images of the grating couplers. First gap of the grating coupler is 60 nm, and the gaps are linearly increasing. Curvatures are set to be matched with mode evolution so that there is no reflection. Top: green spectrum grating coupler. Bottom: red spectrum grating coupler (b) Green line: simulated coupling efficiency vs. wavelength plot of green-spectrum grating coupler optimized for 500 to 600 nm. Black line: measured experimental transmission intensity vs. wavelength plot of green-spectrum grating coupler. (c) Red line: simulated coupling efficiency vs. wavelength plot of red-spectrum grating coupler optimized for 600 to 700 nm. Black line: measured experimental transmission intensity vs. wavelength plot of red-spectrum grating coupler. (d) Fiber edge coupling to the waveguides at 369.5 nm using Nufern SM300 fiber. (e), (f) Free-space edge coupling using aspheric lenses into waveguides that are designed to be single mode in the transverse electric polarization at 468 nm and 369.5 nm, respectively.

visible wavelength from 500 nm to 700 nm wavelength: a green wavelength grating coupler optimized for 500 nm to 600 nm [shown in the top SEM image of Figure 2-3a] and a red wavelength grating coupler optimized for 600 nm to 700 nm [shown in the bottom SEM image of Figure 2-3a]. Figures 2-3b and 2-3c show comparisons between the simulated coupling efficiency spectra and the experimentally measured transmission spectra for the green and red wavelength grating couplers, respectively. The general shape of the experimental grating coupler transmission spectra matches well with the simulated coupling efficiency spectra. The experimental coupling efficiencies are listed in arbitrary units because we do not experimentally mode-match the spatial modes of the grating coupler and collection objective. The peak experimental

transmission intensity for the green wavelength grating coupler is 0.1544 [a.u.] at 532.9 nm, while the peak experimental transmission intensity for the red wavelength grating coupler is 0.1565 [a.u.] at 625.3 nm.

Both green and red wavelength grating couplers are optimized for TE polarization, so the simulated coupling efficiencies model the collection of TE polarized light injected into the 450 nm wide by 200 nm tall AlN waveguide on bulk sapphire and scattered by the grating coupler. For the green wavelength grating coupler, the first gap width is 60 nm and the first grating period is 285 nm. Then, the gap width and grating period both linearly increase from 101 nm and 325 nm to 150 nm and 346 nm, respectively (increasing linearly in each period for 17 periods). Finally, the gratings maintain a gap width of 150 nm and a grating period of 346 nm for the remaining 9 periods. In a similar fashion, for the red wavelength grating coupler, the first gap width is 60 nm and the first grating period is 285 nm. Then, the gap width and grating period both linearly increase from 101 nm and 401 nm to 132 nm and 414 nm, respectively (increasing in each period for 10 periods). Finally, the gratings maintain a gap width of 132 nm and grating period of 414 nm for the remaining 10 periods. For both the green and red wavelength grating couplers, the dimensions of each individual grating period are optimized in order for the spatial mode profile of the diffracted light to be a Gaussian field profile. The grating couplers are also designed to be cladded with PMMA, rather than simple air cladding, in order to increase the out-of-plane coupling efficiency by pulling more of the optical mode away from the underlying sapphire substrate as PMMA has a higher refractive index than air. Both grating couplers are designed for an etch depth of 200 nm in order for ease of fabrication so that the grating couplers and waveguides can be fabricated in the same steps with no additional processing. Therefore, we believe grating couplers with even higher collection efficiency can be achieved with partially etched gratings. All measurements done in the VIS wavelength range of 500 nm to 700 nm use grating couplers for coupling light into and out of the chip.

Next, the fiber edge coupling is shown in Figure 2-3d, with UV fiber (Nufern SM300) and an excitation wavelength of 369.5 nm. Figures 2-3e and 2-3f show free-

space edge coupling using aspheric lenses into waveguides that are designed to be single mode in the transverse electric polarization at 468 and 369.5 nm, respectively. The inverse-tapered waveguides adiabatically transform and expand the AlN waveguide mode to the fiber waveguide mode at the chip's edge facet. As such, for the inverse-tapered edge couplers, a SiON cladding is used in order for the refractive indices of the materials surrounding the AlN waveguide to be to be uniform such that the AlN waveguide mode can be expanded in a circularly symmetric way in order to match to the Gaussian mode of a fiber at the chip's edge facet. All measurements done in the UV wavelength range of 360 nm to 480 nm use edge couplers for coupling light into and out of the chip. It is difficult to quantify the experimental edge coupling loss based on the sources of loss we have. In measuring the transmission loss of sending light into the input edge coupler facet and collecting from the output edge coupler facet, the light propagates along a waveguide that spans across multiple electron beam lithography write fields. At each write field boundary, a dislocation of the waveguide due to stitching errors result in scattering points that contribute to the overall facet-to-facet transmission loss. As such, measuring the transmission loss is not an accurate estimation for the edge coupler coupling loss. However, we are able to achieve at least 40% transmission from input edge facet to output edge facet in our devices.

2.5 High-Q Ring Resonators

Figure 2-2c shows simulated electric field profiles of the AlN waveguide modes for PMMA and SiON cladding for 400 nm and 638 nm wavelengths. The waveguides support a single transverse electric (TE) mode for their respective wavelengths. Wrapping these waveguides into rings produces high Q resonators. The ring resonator measurements are summarized in Figure 2-4. Figure 2-4b shows the response at 369.5 nm of the 40 μm radius ring resonator cladded with SiON around resonance; a Lorentzian fit indicates a Q of >24,000. The resonance in the ring is measured by mapping the intensity of the light scattering from the ring by means of a UV sensitive camera

placed in a microscope above the device. After measuring several devices with increasingly larger waveguide-ring gaps and finding the coupling of the waveguide to the ring decreases each time without transitioning from overcoupled regime to critically coupled regime to undercoupled regime (or at least just from the critically coupled regime to undercoupled regime), we find the smallest waveguide-ring gap resonator to be undercoupled. Since the resonator is undercoupled, the ring resonance cannot be measured directly through an access bus waveguide. Hence, the data shows a resonance peak rather than a dip. Figure 2-4c shows the quality factors of various 40 μm radius ring resonators measured using an optical spectrum analyzer (OSA) for various sampled resonance wavelengths spanning from 380 nm to 480 nm, along with the quality factors at around 369.5 nm using both a frequency doubled pulsed Ti:Sapphire laser (Spectra-Physics Mai Tai) and a continuous-wave (CW) tunable Ti:Sapphire laser (M Squared SolsTiS). The spacings between the sets of sampled wavelengths are not indicative of the ring resonator's Free-Spectral-Range (FSR). Rather, the Free-Spectral-Ranges of the various 40 μm radius ring resonators that we measure from 360 nm to 480 nm span from 0.22 nm to 0.4 nm. If we assume that the propagation loss is dominated by the sidewall scattering loss and linear absorption loss of the material, then we can estimate the propagation loss using the following equation for calculating the loss rate α given the resonator Q, where n_g is the group index [71–75]:

$$Q = \frac{2\pi n_g}{\lambda \alpha} \tag{2.1}$$

Then, the loss can be calculated by:

$$\text{loss} = 10 \log_{10} \left(e^{-\alpha} \right) \tag{2.2}$$

To calculate the loss in units of dB/cm, λ in Eq. (2.1) should be in units of cm. Thus, the Q of >24,000 at 369.5 nm wavelength corresponds to a propagation loss of 75 dB/cm, where we measure the n_g to be 2.45 experimentally from the FSR of the ring by the equation:

$$n_g = \frac{\lambda^2}{(\mathrm{FSR})(L)} \tag{2.3}$$

where L is the length of one round trip around the closed cavity.

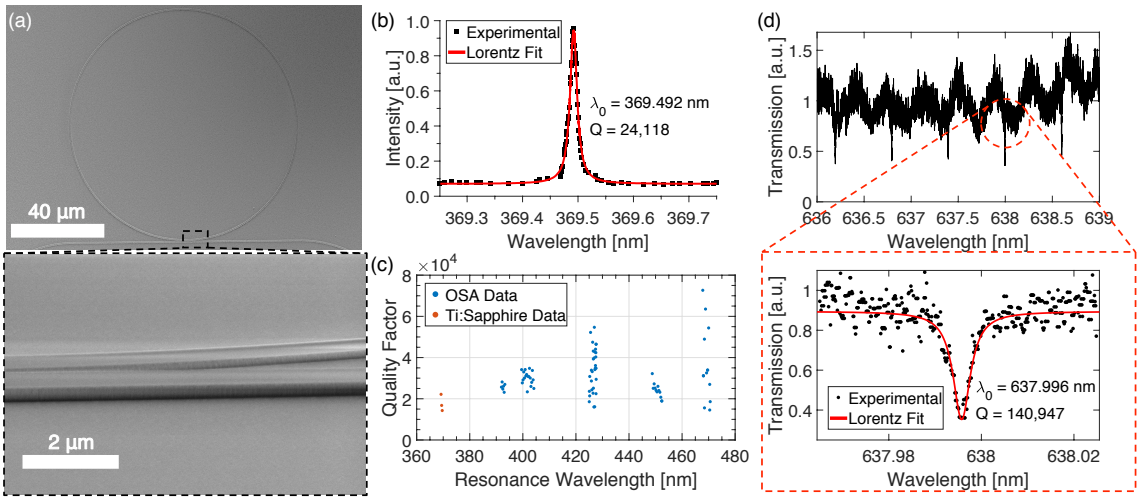

Figure 2-4: (a) SEM of the ring resonator. Inset shows a close up of the ring resonator at a 50 degrees tilted view. The gap between the waveguide and the ring is 300 nm for the undercoupling regime, which was used to verify the unloaded Q. (b) Wavelength response at 369.5 nm of the ring resonator cladded with SiON around resonance. The Lorentzian fitting shows a Q of >24,000. (c) Quality factors of 40 μm radius ring resonators measured using an optical spectrum analyzer (OSA) for wavelengths spanning from 380 nm to 480 nm, along with the quality factors at 369.5 nm wavelength using both frequency doubled pulsed and continuous-wave (CW) Ti:Sapphire lasers. (d) Wavelength response at 637 nm of the ring resonator cladded with PMMA around resonance. The Lorentzian fitting shows a Q of >140,000. Inset shows a zoom-in of the wavelength response.

Figure 2-4d shows the frequency response of a 50 μm radius ring resonator cladded with PMMA around resonance in the red wavelength range. We probe the 50 μm radius ring with an evanescently coupled access waveguide. The Lorentzian fitting shows a loaded Q of >140,000 at 638 nm, and we measure the n_g to be 2.15 experimentally from the FSR of the 50 μm radius ring. In order to obtain the intrinsic Q of the ring resonator, we can use the following [71–75]:

$$Q_i = \frac{2Q_l}{1 \pm \sqrt{T_0}} \tag{2.4}$$

where Q_i is the intrinsic Q, Q_l is the loaded Q, T_0 is the normalized transmitted

power at the resonance wavelength, and the + and − signs correspond to under- and over-coupled regimes, respectively. Since the ring resonator is operating in the undercoupled regime, we find the intrinsic Q to be >170,000, which corresponds to a propagation loss of 5.3 dB/cm.

These ring resonators are useful for measuring the waveguide propagation loss (in the undercoupled regime). In the critically coupled regime, or in a drop-port configuration, they serve as on-chip filters as needed for filtering atomic fluorescence, for example [35]. They can also be used for on-chip photon pair generation [63].

In terms of ring resonator performance, the PMMA cladding should be better than SiON since the PMMA can flow into the gap between the ring resonator and bus waveguide in order to completely fill that up. By nature of PECVD deposition, the SiON cannot completely fill in the gap between the ring resonator and bus waveguide. However, the SiON is necessary for making edge couplers with high coupling efficiency and mode matching to a fiber, so SiON is used for cladding the ring resonators with resonance at around 369.5 nm. Furthermore, since PMMA is a polymer, it is not suitable for UV wavelengths due to autofluorescence.

2.6 High Extinction Distributed Bragg Reflectors and On-Chip Beamsplitters

Distributed Bragg reflectors (DBRs) represent another important PIC component as broadband on-chip reflectors and filters. To further support this point, we develop a distributed Bragg reflector with high extinction for 532 nm for use as on-chip filtering of the excitation pump light used for exciting NV centers in diamond. The DBR has a period of 140 nm with 50% duty cycle, and it is designed to have an adiabatic tapering from the regular waveguide into the DBR in order to have low insertion loss. Also, the DBR is designed to structurally have rounded features for ease of fabrication. Figure 2-5a shows an SEM image of the fabricated DBR. The overlay blue plot in Figure 2-5b shows the simulated transmission spectrum for the DBR, which has 45

dB extinction for the 532 nm green pump light. The black plot in Figure 2-5b shows at least 13 dB extinction experimentally for the DBR. We expect the extinction to be even higher because the attenuated 532 nm signal was at the noise floor of our experimental system.

The decreased transmission of the DBR simulation at wavelengths around 500 nm is due to the third order TE mode at around 500 nm wavelength for the ∼735 nm wide waveguide portions of the DBR. At the wider sections of the DBR, the first order TE mode can couple with this mode, which is leaky since it cannot propagate through the entirety of the DBR due to the fact that the third order TE mode is not allowed at the narrower sections of the DBR.

Figure 2-5c shows a directional coupler with a 50/50 splitting ratio, which is the integrated photonics equivalent of a free space beamsplitter, for the wavelength of 637 nm. The directional coupler is intended to be used with PMMA cladding. Directional couplers coherently couple between adjacent waveguide modes and can be used as a building block for Mach-Zehnder interferometers (MZIs) [76]. Figure 2-5d shows the power at the output two arms of the directional coupler as the length of the straight, parallel waveguides portion of the coupling region (denoted as "Coupling Length") is swept for different devices. The gap between the two straight, parallel waveguides in the coupling region is 200 nm. A coupling length of 14 μm results in a 50/50 splitting ratio. We subtract the power measured at each of the two output ports of the directional coupler by the background noise. Since the power at the output port 2 for a coupling length of 0 μm is at the noise floor of our system, we get that there is zero transmission for port 2. The same can be said about output port 1 for a coupling length of 25 μm.

Theoretically, for a pair of coupled waveguides with the same geometry and dimensions, the fraction of cross-coupled power K is given by the following, where Δn is the effective refractive index difference between the symmetric and antisymmetric supermodes and L is the length of the directional coupler [77]:

$$K = \sin^2\left(\frac{\pi L \Delta n}{\lambda}\right) \tag{2.5}$$

By using a mode solver to calculate Δn and solving for Eq. (2.5) to get 50/50 splitting ratio ($K = 0.5$), we get that L should be 23 µm. However, this does not take into account the coupling from one waveguide into the other as the two waveguides are brought to the desired separation of 200 nm in the evanescent coupling region via waveguide bends. In simulating the full directional coupler structure with the evanescent waveguide coupling region and bent region, we find a coupling length of 14 µm necessary for achieving 50/50 splitting, matching well to the experimental result.

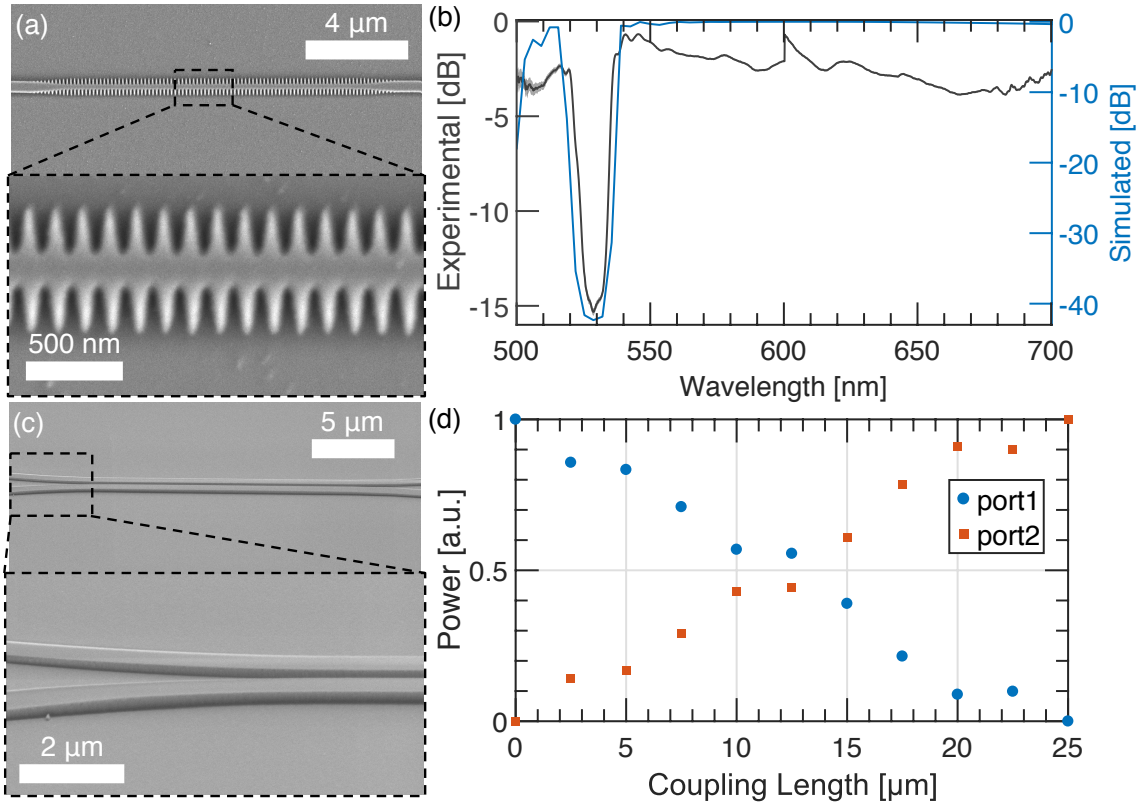

Figure 2-5: (a) SEM of the distributed Bragg reflector (DBR) with adiabatic tapering for low insertion loss. Inset shows a zoom-in of the DBR. (b) Simulated and measured transmission vs. wavelength for the DBR. In simulation, we achieve 45 dB extinction for 532 nm green pump light typically used for NV excitation. Experimentally, we achieve >13 dB extinction for 532 nm. (c) SEM of directional couplers with 50/50 splitting ratio at a 50 degrees tilted view. Inset shows a zoom-in of the directional couplers at a 50 degrees tilted view. (d) Measured transmission power at the two output ports of the directional couplers as a function of coupling length in the straight, parallel waveguides region.

2.7 Conclusions and Outlook

The UV propagation loss shown here at 369.5 nm is several tens of orders of magnitude lower than the propagation loss shown by Stegmaier et al. for 400 nm wavelength in an AlN on SiO_2 platform [78]. Furthermore, the crystalline materials in our AlN on sapphire platform allow for refined Raman and other parasitic processes to be localized and minimized [79]. Although the UV single mode propagation loss presented here is higher than that shown in SiN-on-SiO_2 multimode and planar waveguides for wavelength at the lower end of the visible spectrum [80, 81] and silica-on-silicon waveguides in theory for UV and VIS [82, 83], SiN-on-SiO_2 and silica-on-silicon platforms are limited to passive components and thermo-optic tuners [84]. Furthermore, silica waveguides are typically a couple of microns in dimension with large bend radii and are not ideal for compact, high-density, large-scale photonic integration. Hence, our AlN on sapphire platform, to date, has the record-low waveguide propagation loss down to UV wavelength for active optical materials with $\chi^{(2)}$ properties and supports chip-scale, compact, CMOS-compatible integration [78, 85]. Nonetheless, we believe that there are many sources of loss that can be eliminated or improved upon. One of the main causes for the propagation loss is interface scattering from the roughness of the AlN waveguide sidewalls from etching. To reduce the propagation loss by a few orders of magnitude, one can engineer the waveguide dimensions such that the optical mode overlaps minimally with the sidewalls so that the light scatters minimally from the waveguide's faces [71]. Furthermore, the current waveguide fabrication is optimized for vertical sidewalls so that the photonic components experimentally match well with the simulated design. As such, the reactive-ion etching necessitates a fast physical etch that causes the sidewalls to be rougher than could be possible with a more chemical etch. Sidewall roughness of less than 0.1 nm is often the benchmark for achieving interface scattering close to that of the bulk scattering limit of optical materials [86]. It may be possible to further optimize the etching parameters to reduce loss. In addition, there is an inherent roughness of the top surface of the AlN thin film from the unoptimized growth. As AlN grown on top of sapphire is still

not at the level of silicon on insulator (SOI) wafers made by Smart-Cut® technology used in conventional integrated photonic platforms [87], we expect there to be room for improvements. Finally, the AlN thin film we use is crystalline in the growth direction and polycrystalline in the in-plane direction. Replacing this material with a completely crystalline AlN thin film grown on top of sapphire should result in a lower dislocation density and defect density, thereby improving the purity of our material so that it would behave closer to what is expected of bulk AlN. Furthermore, the crystallinity of single-crystal AlN grown on top of sapphire has been shown to improve significantly by high temperature annealing [88]. The nonlinear susceptibilities $\chi^{(2)}$ and $\chi^{(3)}$ of AlN are material dependent and approximately independent of the film crystallinity, even when taking into account small variation due to crystal stress/strain during growth. However, the effective nonlinearity experienced for nanocrystalline AlN will have a reduced percentage of that intended crystal axis in the field propagation direction of the waveguide mode, thus reducing the effective nonlinearity when compared to epitaxially grown single crystal AlN. As such, further improvements on the crystallinity of AlN thin film grown on top of sapphire would be beneficial for nonlinear applications as well.

Table 2.1 shows a comparison of this work with other previously demonstrated UV/VIS photonics platforms that are chip-scale and highly compact, particularly AlN on SiO_2 and SiN on SiO_2. This work shows the highest demonstrated resonator Q factor in the UV, as well as higher VIS resonator Q factor than in previous AlN on SiO_2 work [51]. As the AlN thin film shown in this work is crystalline with fewer absorptive defects and dislocation density than the polycrystalline AlN in previous work, AlN on sapphire can in principle support wavelength into the deep UV; SiN has been shown to have significant optical absorption in wavelengths less than 470 nm and down into the UV range due to silicon incorporation into the layers inherent in the SiN growth [89]. Due to this, even though state-of-the-art SiN on SiO_2 has lower single mode waveguide loss compared to AlN single mode waveguides in the visible wavelength, AlN photonics platforms have the capability to operate in the UV regime. Furthermore, AlN has a high piezoelectric coefficient and moderately

high electro-optic coefficient compared to materials used in commercially available phase and amplitude modulators, allowing for active optical components. Finally, AlN's high thermal conductivity κ and small thermo-optic coefficient $\mathrm{d}n/\mathrm{dT}$ allows devices to be less sensitive to temperature fluctuations, which is important for its many potential applications that require high-precision manipulation, routing, and read-out.

In conclusion, we have demonstrated a PIC platform based on the crystalline, wurtzite AlN on top of a sapphire substrate. Both AlN and sapphire are wide bandgap (6.015 eV [90] and 8.8 eV [91], respectively) and transparent from the UV to the mid-infrared [52, 92, 93]. We observe record-high quality factors exceeding 20,000 down to 369.5 nm, which corresponds to record-low propagation loss at 369.5 nm for active optical materials that have $\chi^{(2)}$ properties. The nonlinear, electro-optic, and piezoelectric properties of AlN make it a promising active material for controlling and connecting atomic and atom-like quantum memories, as well as for other applications such as UV spectroscopy and solar-blind communications.

	AlN on sapphire (this work)	AlN on SiO_2 [51, 52]	SiN on SiO_2 [94, 95]
Resonator Q factor	Q = 24k (369.5 nm) Q = 140k (638 nm)	Q = 7k (410 nm)[a] [96] Q = 110k (774 nm) [51]	Q = 4.4k (290 nm)[b] [97]
Supporting wavelength	UV (∼210 nm) to IR [52, 92, 93]	UV (∼320 nm) to IR [51]	VIS (∼470 nm) to IR [80]
Crystallinity	Crystalline	Polycrystalline (c-axis grown)	Stoichiometric
Active properties	electro-optic: r_{33} = ∼1 pm/V piezoelectric: d_{33} = ∼5 pm/V [93, 98, 99]		electro-optic: 8.31 fm/V [100]
Single mode WG loss	75 dB/cm (369.5 nm)[c] 5.3 dB/cm (638 nm)[c]	650 dB/cm (400 nm) [78] 6.4 dB/cm (774 nm)[c]	< 1 dB/cm (532 nm) [101] 1.5 dB/cm (850 nm) [102]
Thermal properties (waveguide material)	κ = 285 W/m·K dn/dT = 2.32×10^{-5}/K [52]		κ = 1.4 W/m·K dn/dT = 1.0×10^{-5}/K [103]

[a] AlN disk resonator on Si pedestal

[b] Disk resonator

[c] Loss estimated from resonator Q factor

Table 2.1: Comparison of different UV/VIS photonics platforms.

2.8 Supporting Information

This section includes useful technical details for this chapter.

2.8.1 AlN Photonics Fabrication Recipe

While mentioned briefly earlier. Here, we will give a detailed list of the steps and tools with known model numbers that were used for the AlN photonics fabrication

recipe.

1. Spin coat Shipley Microposit S1813 positive-tone photoresist on an as-received AlN-on-sapphire whole wafer at 3000 rpm for 60 seconds with an acceleration of 1000 rpm/s, followed by baking at 85°C for 3 minutes. This is an uniform protective layer for dicing the wafer into smaller chips.

2. Using an automatic dicing saw (DISCO DAD-3240), dice the whole wafer into 1 cm $\times$ 1 cm chips.

3. Clean the 1 cm $\times$ 1 cm unpatterned chips with sonication in acetone for 10 minutes, methanol for 5 minutes, and isopropyl alcohol for 5 minutes.

4. Use the electron beam evaporator (Temescal VES2550) to deposit 5 nm of Cr on top of the AlN layer at a rate of 1 Å/s.

5. Treat the chip with oxygen plasma treatment under 100 W for 3 minutes to improve electron beam adhesion.

6. Spin coat hydrogen silsesquioxane (HSQ) (2% XR-1541) at 2000 rpm for 60 seconds with an acceleration of 1000 rpm/s, with no subsequent baking.

7. The HSQ patterns are written with an Elionix ELS-F125 electron beam lithography system at 125 keV using a dose of 10,000 $\mu C/cm^2$ and 1 nA beam current.

8. Develop in salty developer, which is an aqueous mixture of 1 wt% NaOH and 4 wt% NaCl (for high contrast) for 2 minutes 40 seconds, followed by 10 minute rinse in deionized water to stop development and ensure cleaning away of any residual salt. Then immerse in isopropyl alcohol for 1 minute, followed by gentle nitrogen air drying to not damage the structures.

9. After HSQ mask patterning, the pattern is first transferred to the Cr layer at an etch rate of 55 nm/min for 1 min to ensure complete breakthrough of the Cr layer by electron cyclotron resonance reactive-ion etching (ECR-RIE) (Plasmaquest Series 11 Model 145) using a gas mixture of Cl_2/O_2 (3:1 ratio) at

300 W ECR power, 30 W RF Bias power, 10 mTorr pressure, and 25°C. After this step, the side view of the chip looks like the following:

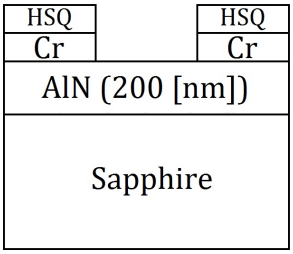

Figure 2-6: Side view of chip after HSQ patterning and Cr dry etch.

10. Then, the AlN waveguides and photonic components are etched by inductively coupled plasma reactive-ion etching (ICP-RIE) (SAMCO 200iP) using a gas mixture of $BCl_3/Cl_2/Ar$ in two steps. The first step is for etching the native aluminum oxide at an etch rate of 5 nm/min using BCl_3 /Ar (2:1 ratio) at 120 W ICP power, 40 W RF Bias power, 7.5 mTorr pressure, and 40°C for the sample holder. The second step is for etching the AlN at an etch rate of 200 nm/min using Cl_2/Ar (4:1 ratio) at 360 W ICP power, 100 W RF Bias power, 5 mTorr pressure, and 40°C for the sample holder. We do not observe a significant change in the surface roughness from the etching, and a sidewall angle close to 90 degrees is achieved due to the combination of physical sputtering and plasma chemical etching.

11. HSQ is removed with 10 seconds in buffered oxide etch (BOE), followed by rinsing in deionized water for at least 10 minutes while cleaning up the acid bench. Then, Cr is removed with a 1 minute dip in Cr-7 etchant, followed by 5 minutes in deionized water to clean off the Cr-7, followed by 1 minute in isopropyl alcohol. Then, gentlly air-dry the chip with nitrogen to not damage the structures.

12. To clad the chip with PMMA, A11 PMMA is spun on at 4000 rpm for 60 seconds with an acceleration of 1000 rpm/s, followed by baking at 180 °C for 2 minutes. Otherwise, SiO_xN_y is cladded with the recipe listed in the next section.

13. Prior to edge polishing, the chip is spin coated with photoresist to protect the top surface from polishing debris. Then, the edge polishing is done with standard mechanical polishing process performed with an Allied Multiprep Polisher by sequentially reducing the grit sizes (30 μm to 0.1 μm) until the polished facet is within the edge coupler taper region. Following polishing, the chips are soaked in acetone for 1-2 minutes to strip the resist and remove polishing particulates, followed by a rinse of methanol or isopropyl alcohol. More details provided in reference [104].

2.8.2 SiO_xN_y Cladding Recipe

The waveguides are clad with approximately 3 microns of SiO_xN_y using plasma-enhanced chemical vapor deposition (PECVD) by the parameters shown in Table 2.2 using an Oxford 100 PECVD system, with deposition rates determined with test silicon samples prior to actual deposition.

LF Power (W)	Pulse Time (s)	HF Power (W)	Pulse Time (s)	Chamber Pressure (mTorr)	Chamber Temperature (°C)	SiH_4 (sccm)	NH_3 (sccm)	N_2O (sccm)	N_2 (sccm)
160	12	200	8	1900	350	20	70	50	1425

Table 2.2: SiON Process Conditions in Oxford 100 PECVD System

2.8.3 Ion Milling for Edge Coupler Fabrication

While conventional mechanical polishing to make edge couplers in our photonics platform is possible, the process sometimes suffers from delamination of both the highly-stressed SiO_xN_y cladding material and sometimes the edges of the waveguides due the lateral shear forces of mechanical polishing. Edge coupling of fibers to integrated photonic waveguides can in theory allow for low loss, large bandwidth coupling, but it also depends strongly on the facet's polishing quality. The imperfect edge polishing

results in facets where it may then be impossible to directly couple to the chip by fiber or using free-space optics due to significant scattering sites or distortions in the waveguide facet optical mode, leading to mode mismatch at the edge interface. As such, it is necessary to develop an alternative process for producing edge couplers with high yield repeatably. Plasma etching the edge facets is not possible due to the high chemical etch resistance of sapphire compared to AlN and SiON. Hence, we considered ion milling to produce optical-grade quality facets in our photonics platform. This work was led by our collaborators in Professor Stefan Preble's group at Rochester Institute of Technology [104].

After the last step of the AlN photonics fabrication recipe listed above in which the chip is mechanically edge polished after deposition of SiO_xN_y in the step prior, the stress in the SiO_xN_y cladding would sometimes lead to facet and waveguide damage during polishing like what is shown in Figure 2-7a. As a result of the damage to the facet, waveguide, and cladding in some areas, neither fiber coupling nor free space coupling were possible. These chipped facets were then salvaged by ion milling.

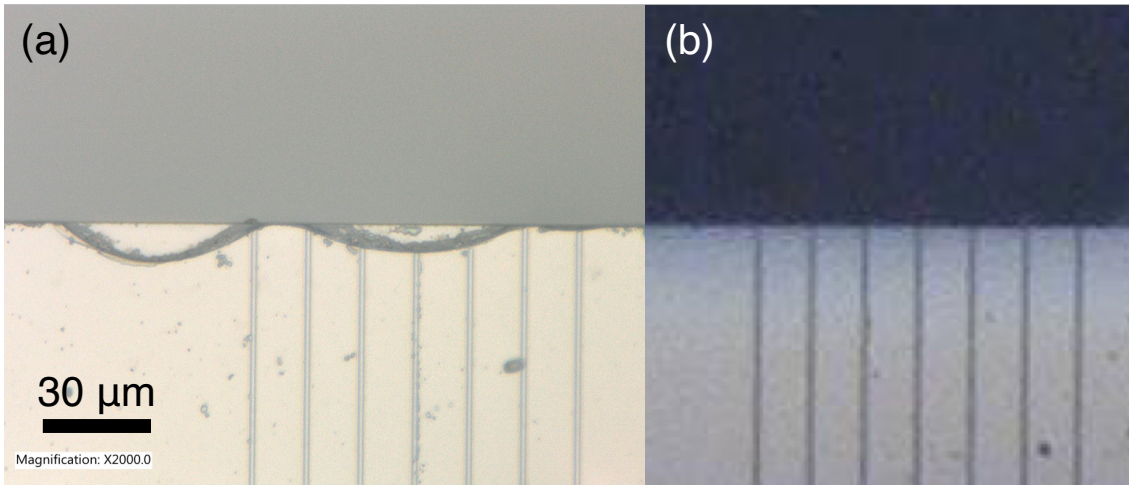

Figure 2-7: (Left) 2000x optical micrograph of the chipped facet from conventional mechanical edge polishing. Notably the cladding and waveguide often delaminate together which prevents direct end-fire fiber coupling and free space coupling. (Right) 2000x micrograph of the same optical chip with an ion milled facet suitable for fiber or free space coupling.

The chips were ion milled using a JEOL IB-09100CP cross-section polisher. The process is as followed:

1. Mount with wax on the metal chuck of the ion mill.

2. Align the chip such that 40 μm to 60 μm of the chip edge containing the waveguide edge tapers is exposed for milling.

3. Set the accelerating bias to 6.5 keV, with 6 to 7 sccm of Ar gas. Etch for 3 hours to polish a facet region that is 1 mm wide by at least 70 μm deep to fit a bare SM300 fiber that has a 125 μm diameter.

4. Remove the chip and soak in acetone for 1-2 minutes to remove the mounting wax, followed by a rinse with methanol then isopropyl alcohol.

The resulting is shown in Figure 2-7b, where there are minimal defects at the facet due to the absence of pressure that the chip typically experiences during mechanical polishing that may cause delamination, chipping, and cracking of the SiO_xN_y cladding and AlN waveguide. Figure 2-8 shows a cross-section profile of the facet after ion milling, highlighting the smooth optical-grade quality of the ion-milled facet. After reclamation of the facet with this method, we can then couple to waveguides that we could not previously couple to. This process can be used as an alternative polishing method resulting in facets that are comparable to, if not better than, conventional polishing methods, but this process is also much more reproducible with high yield. However, this process takes 3 hours to polish a region that is only 1 mm wide and does not result in a flat, uniform edge facet, so this may have to be developed further if we would like to use this method to produce an array of edge couplers to directly couple to a fiber array. Nonetheless, it is a very useful method to salvage test devices that would otherwise be useless.

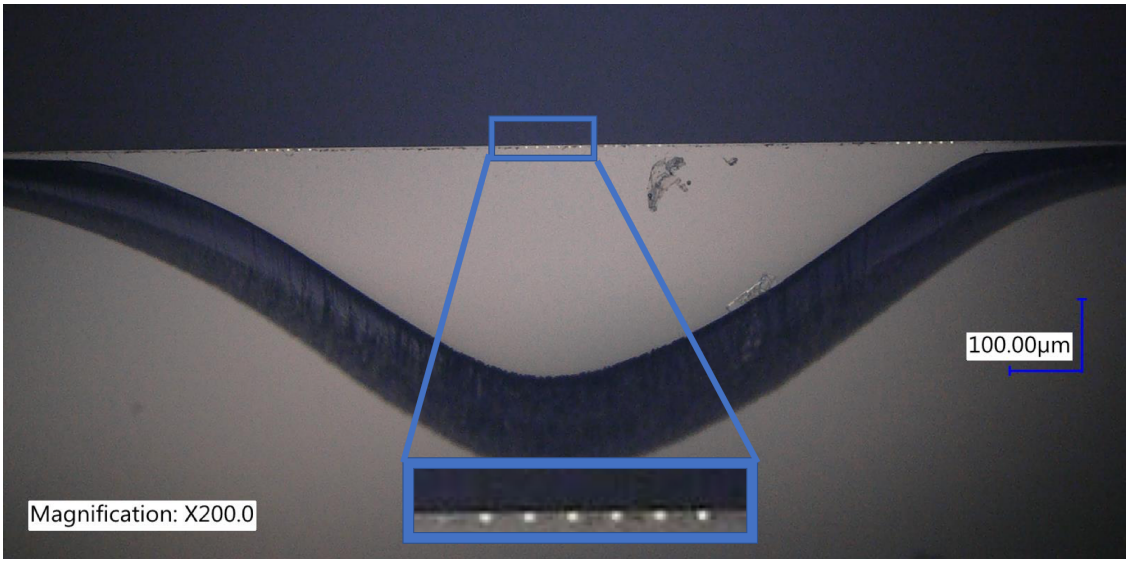

Figure 2-8: 200x optical micrograph of ion milled facet. (Inset) Waveguides array along the top edge.

Chapter 3

Bright high-purity quantum emitters in aluminum nitride integrated photonics

Materials presented in this chapter have been previously uploaded onto arXiv, and the text in this chapter is reproduced from this arXiv preprint (arXiv:2006.16276 (2020) [105]).

3.1 Background on Single Photon Emitters Based on Atomic Defects

Quantum emitters (QEs) with on-demand single photon emission are central building blocks for photonic-based quantum communication and quantum computation [2, 6]. Over the past decade, crystal defect centers in wide-bandgap semiconductors have emerged as excellent solid-state QEs. In particular, a variety of color centers in diamond [17, 29, 30, 106, 107], 4H silicon carbide (SiC) [108, 109], and 6H SiC [110] have been demonstrated to have stable optical transitions coupled to long-lived spin ground states at room and cryogenic temperatures, resulting in spin-dependent single photon emission. The spin-photon interface provides access to electron spin states or

indirectly to nuclear spin states, which can serve as quantum memories for quantum information processing [1, 111] and quantum-enhanced sensing [112].

Although these QEs in diamond and SiC have the leading properties amongst solid-state emitters, there is a lack of active chip-integrated photonic components and wafer-scale thin film single-crystal diamond or SiC on low-index insulator, which limit the scalability of monolithic quantum information processing architectures in these materials. Hence, there is increased interest in exploring QEs in other material systems that can support both high-quality QEs and monolithic integration of wafer-scale photonic integrated circuits (PICs). Recently, alternative wide-bandgap materials such as two-dimensional hexagonal boron nitride (2D hBN) [113], gallium nitride (GaN) [114], and aluminum nitride (AlN) [115] have attracted attention as potential host materials for quantum emitters due to their single-crystal heteroepitaxy of thin film materials or the possibility to be integrated to any PIC platform in the case of 2D hBN [116]. Theoretical calculations show that AlN can serve as a stable environment for hosting well-isolated QEs with optically addressable spin states [43], though experimental demonstrations of such QEs are outstanding. In contrast to diamond or SiC, which have strong covalent bonds, AlN is an ionic crystal with piezoelectric properties that may offer strain-based acoustic control for quantum spins [117].

AlN is widely used in optoelectronics [51], high power electronics [118], and microelectromechanical systems [119], resulting in a large, continuously expanding industry bolstered by mature fabrication and growth technologies. AlN's optical transparency is bounded at the short-wavelength side by an exceptionally large bandgap of 6.015 eV (corresponding to ultraviolet) and extends to the mid-infrared spectrum [90]. Its high thermal conductivity (κ = 285 W/m·K) and small thermo-optic coefficient (dn/dT = 2.32$\times$ 10^{-5}/K) enable AlN devices to operate with long-term optical and physical stability [52]. The wide bandgap and the availability of highly crystalline AlN thin films grown on low-index sapphire substrates, has enabled excellent AlN-based PIC platforms (Chapter 2 of this thesis [44]), with a wide variety of nonlinear optical effects such as parametric frequency conversion [63], sum/difference frequency gener-

ation [62], electro-optic modulation [52], and frequency comb generation [62]. Here, we report on two types of bright room-temperature QEs emitting in the orange visible spectrum integrated in a scalable AlN-on-sapphire PIC platform, as shown conceptually in Figure 3-1a, made possible by overcoming several material and processing challenges. Well-established fabrication processes for AlN PICs shown in previous works [44, 116, 120] enable engineering of QE-based quantum photonic devices tailored to any application needs.

3.2 Material processing and quantum emitter creation in AlN

Our studies used wurtzite-phase AlN thin film on sapphire (Al_2O_3) (Kyma Technologies, Inc.) with an AlN thickness of 200 nm. These samples were grown by plasma vapor deposition of nano-columns (PVDNC) with a macro defect density of less than 10 per cm^2. The crystal orientation is along the c-axis ($00.1 \pm 0.2°$), as indicated in the black inset in Figure 3-1a.

To create vacancy-based emitters, we ion-implanted the sample using a He ion microscope (Zeiss ORION NanoFab) at a He ion fluence of around 10^{15} ions/cm^2 with an accelerating voltage of 32 keV, followed by annealing in an argon environment at ambient pressure, which prevents AlN surface oxidation that occurs in ambient air at temperatures above 700°C [121].

We investigated different annealing recipes with maximum temperatures between 500°C and 1000°C. As seen from the atomic force microscope scans in Figure 3-1b, the 1000°C annealing reduced the root mean square surface roughness five-fold from 2.724 nm to 0.541 nm. The nano-columns maintain the hexagonal crystal structure after annealing, indicated in the cutouts in Figure 3-1b, suggesting that the sample polytype remained wurtzite.

We characterized these samples by photoluminescence (PL) imaging in a confocal microscope setup, using 532 nm laser excitation (Coherent Verdi G5 laser, power

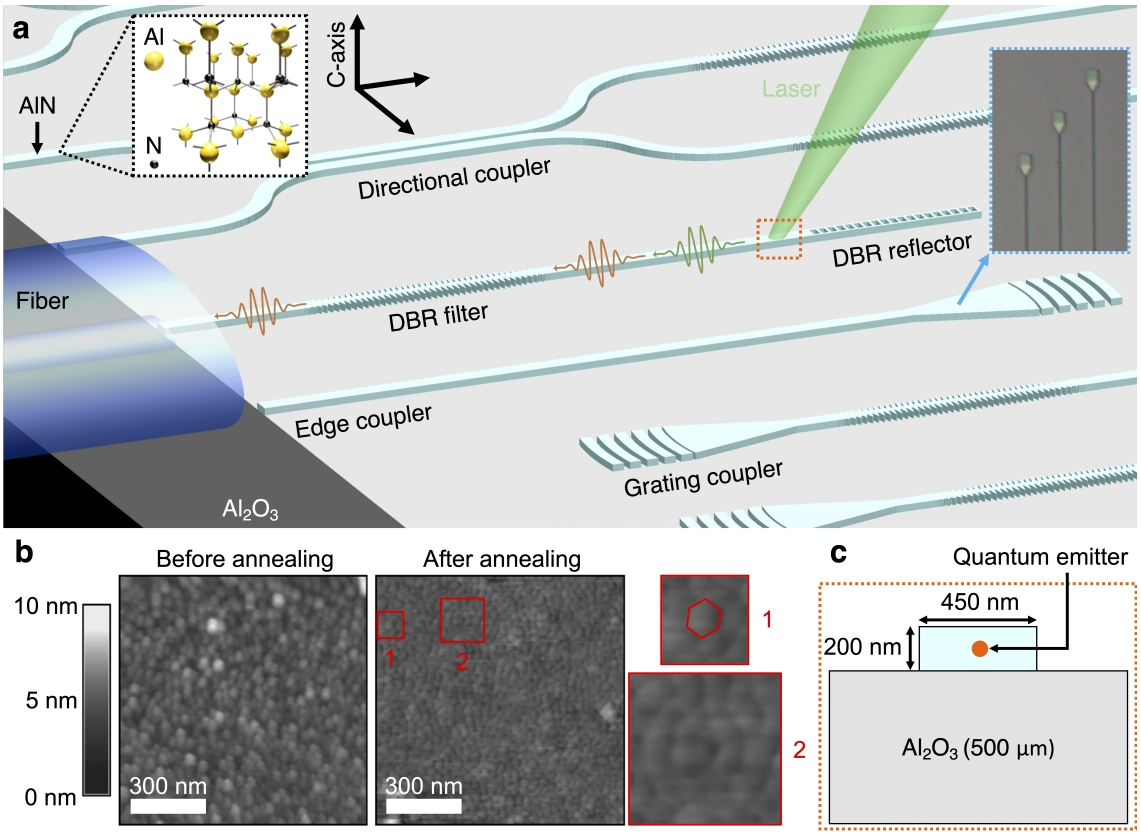

Figure 3-1: Quantum emitters in aluminum nitride integrated photonics. (a) Scalable AlN-on-sapphire photonic integrated circuits with integrated quantum emitters. Black inset: Wurtzite crystal structure of aluminum nitride (yellow: aluminum atom, black: nitrogen atom). Blue inset: Microscope image of the fabricated QE-integrated waveguides, where the grating couplers are used for visual feedback during fiber edge coupling. (b) Atomic force microscopy of a sample before and after annealing. Cutout 1 indicates the hexagonal structure of the nano-columns is maintained after annealing. Cutout 2 shows reduced surface roughness, slightly smaller grain size, and smoothing of the AlN film columnar structure with improved orientation alignment to the c-axis, indicating an improved crystallinity to the AlN Film. (c) Close-up cross-section of the single-mode AlN-on-sapphire waveguide, which is 450 nm in width by 200 nm in height. The quantum emitter is embedded within the AlN waveguide (not necessarily in the exact center as shown).

before the objective ∼1 mW) through a 0.9 NA microscope objective (Nikon). The PL was filtered with a 560 nm long-pass filter and detected with avalanche photodiodes (APDs by Excelitas) via single mode fibers. These measurements showed a spatially uniform PL background, but no resolvable isolated QEs, for AlN samples annealed up to 700°C; this background PL is reduced more than a hundred-fold and QEs are

detectable in samples annealed at 1000°C, which is the material processing condition used for the samples that are studied in the rest of this work.

The observed PL background reduction in combination with the lower surface roughness suggests an improved crystal structure, characterized by higher-uniformity nano-columns. We tentatively attribute the reduced background to fewer unwanted defect centers in the bulk and on the surface of the material.

3.3 Spectral Analysis of Quantum Emitters

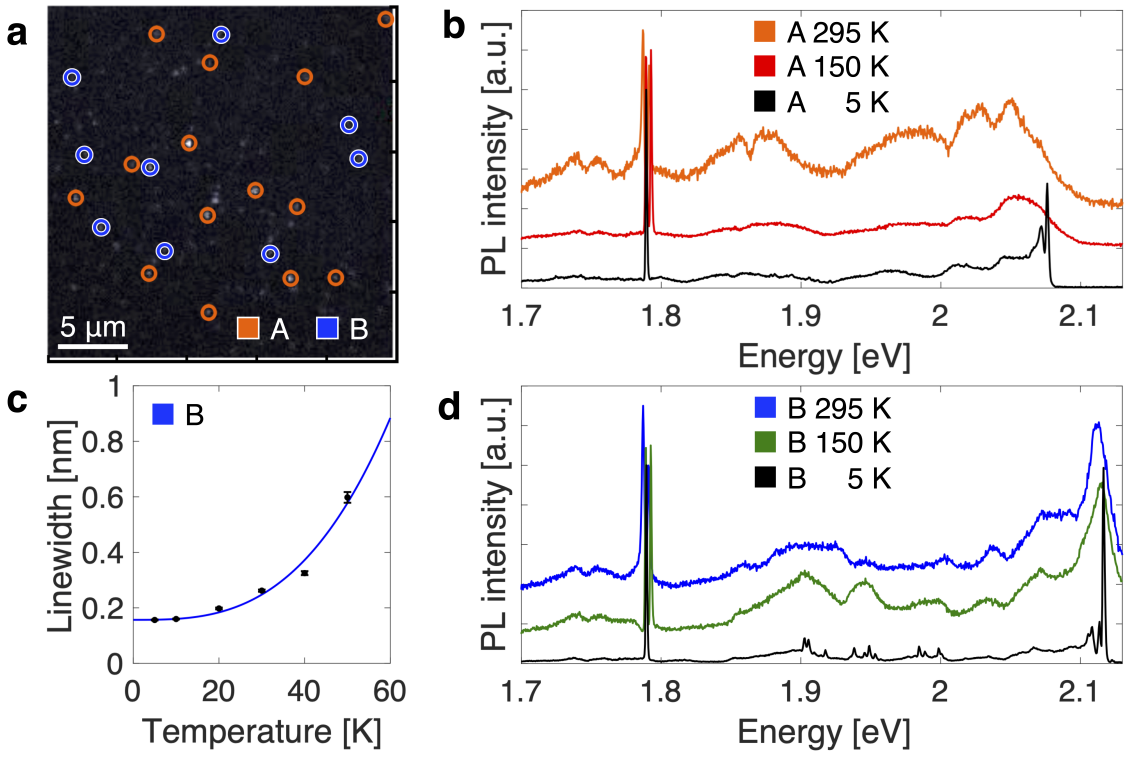

Figure 3-2: Spectral analysis of quantum emitters in thin-film w-AlN. (a) Quantum emitter density in a 25 µm × 25 µm area (white scale bar: 5 µm). Two types of emitters with orthogonal polarization states are identified, labeled as "A" and "B". (b) Temperature-dependent PL spectra of a representative type A quantum emitter (black: 5 K, red: 150 K, orange: 295 K). The spectra for 150 K and 295 K are offset vertically for clarity. (c) Temperature dependence of the type B quantum emitter's zero-phonon line linewidth. (d) Temperature-dependent PL spectra of a representative type B quantum emitter (black: 5 K, green: 150 K, blue: 295 K). The spectra for 150 K and 295 K are offset vertically for clarity.

The room-temperature PL scan of a representative AlN sample after 1000°C an-

nealing (Figure 3-2a) shows a dark background with bright, micron-spaced bright spots. Analysis of the PL spectra, photon statistics, emission lifetime, and polarization reveal these spots to be two orthogonally polarized classes of QEs labeled "A" and "B" (see Figure 3-4d), as detailed next.

At room temperature, both types of QEs emit in a broad spectrum covering from 580 to 650 nm, as seen in the curves labeled as 295 K in Figure 3-2b,d (spectra taken with Princeton Instruments Isoplane SCT320 spectrometer with a resolution of 0.07 ± 0.01 nm). The lines at 1.79 eV are caused by Chromium ion related impurities in sapphire [122] that we filter in following measurements with a 690 nm shortpass filter.

We performed low-temperature PL measurements to study phonon coupling characteristics in a closed-cycle helium cryostat (Montana Instruments) with a built-in confocal objective (NA = 0.9), and we used the same 532 nm laser for excitation and APDs for detection as previously stated. Figure 3-2b,d shows low-temperature PL spectra of a type A and B QE, respectively, at 5 and 150 K. Common to all 5 K spectra is a strong zero-phonon line (ZPL) peak, accompanied by a red-shifted satellite peak.

The temperature dependence of the ZPL linewidth gives information about the interaction between the defects and host crystal lattice, as well as the emitter dephasing mechanisms. Figure 3-2c shows the temperature dependence of the emitter linewidth approximated from Lorentzian fits for a type B emitter. We determine a linewidth of 0.16 ± 0.01 nm at 5 K, which is not limited by the spectrometer resolution (∼0.07 nm). A T^3 function fits the linewidth broadening with increasing temperature, similar to the silicon vacancy (SiV) and other defects in diamond [123]. The T^3 dependence results from field fluctuations caused by phonon-induced dislocations of crystal defects and color centers [124], allowing us to conclude that these AlN QEs are point defects.

The Debye-Waller factor (DWF) indicates the extent of electron-phonon coupling for the emitter. We estimate it from DWF = $I_{\mathrm{ZPL}}/I_{\mathrm{TOT}}$, where I_{ZPL} is the ZPL PL emission and $I_{\mathrm{TOT}} = I_{\mathrm{ZPL}} + I_{\mathrm{PSB}}$ is the total PL emission calculated by combining

the ZPL PL emission I_{ZPL} with the phonon broadened PL I_{PSB}. Here, we fit the ZPL and PSB peaks with separate Lorentzian fit functions. At cryogenic temperatures we determine the DWF to be 15 ± 2%.

3.4 Photon Statistics Characterization of Emitters

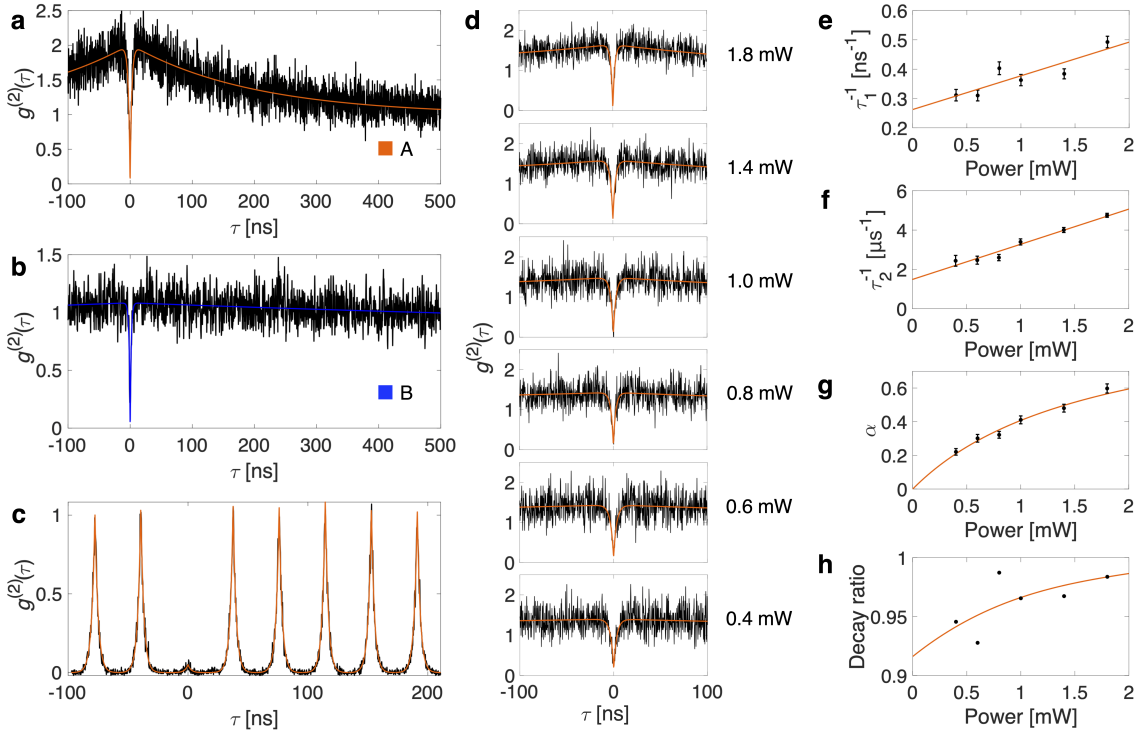

Figure 3-3: Photon statistics characterization of quantum emitters. Continuous wave excitation second order autocorrelation histogram with (a) $g^{(2)}(0) = 0.08 \pm 0.06$ for a type A emitter and (b) $g^{(2)}(0) = 0.09 \pm 0.08$ for a type B emitter. (c) Pulsed excitation second order autocorrelation histogram for a type A emitter with $g^{(2)}(0) = 0.05 \pm 0.002$. (d) Power-dependent second-order autocorrelation histograms for a type A emitter. Power-dependence of the reciprocal values of fitting parameters (e) τ_1 and (f) τ_2 in the second-order autocorrelation fits. The plots are linearly fitted (orange) and reflect the decay rates of the excited and metastable states, respectively. (g) Power-dependence of the fitting parameter α, which is representative of the non-radiative transitions via the metastable state. (h) Power-dependence of the decay ratio, which is defined as the ratio between the decay rate from the excited state to the ground state compared to the sum of all first order decay rates from the excited state.

We measured the second-order autocorrelation photon statistics of the emitters

with a Hanbury Brown Twiss (HBT) interferometer. Figure 3-3a,b show the normalized second-order autocorrelation histograms for representative type A and B emitters, respectively, under 532 nm, 1 mW continuous-wave (CW) excitation at room temperature. The type A emitter has $g^{(2)}(0) = 0.08 \pm 0.06$ while the type B emitter has $g^{(2)}(0) = 0.09 \pm 0.08$, confirming that the emission is predominantly single photon emission for both types of emitters ($g^{(2)}(0) < 0.5$). The histogram in Figure 3-3a indicates a strong bunching near $\tau = 0$, whereas the histogram in Figure 3-3b has weak bunching. This photon bunching feature suggests the presence of a dark metastable state. Figure 3-3c shows second order autocorrelation histogram of a representative type A emitter under pulsed excitation at room temperature with the laser set at a central frequency of 532 nm, 10 nm bandwidth, and 26 MHz repetition rate. Pulsed excitation resulted in further improved single photon purity of $g^{(2)}(0) = 0.05 \pm 0.002$.

A typical two-level model does not explain the bunching behavior near $\tau = 0$ in the second-order autocorrelation histograms. We therefore adopt the next-simplest level diagram shown in Figure 3-4a: a three-level system with pump-power dependent transition rates. This models the essential features we observe and allows comparison with other well-studied emitters. Equation 3.1 shows the three-level model for fitting the experimental $g^{(2)}(\tau)$ data:

$$g^2(\tau) = 1 - (1 + \alpha) \exp(-\frac{|\tau|}{\tau_1}) + \alpha \exp(-\frac{|\tau|}{\tau_2}) \tag{3.1}$$

where τ_1, τ_2, and α are the excited state lifetime, metastable state lifetime, and fitting parameter. Figure 3-3d shows the power-dependent second-order autocorrelation histograms for a type A emitter, which are used to evaluate the electron dynamics. We mainly focus on a type A emitter for these measurements due to its photostability compared to type B emitters, as shown in Figure 3-4e.

Fitting parameter τ_1 describes a two-level system with transitions between the ground state and a single excited state. Figure 3-3e shows a plot of $1/\tau_1$ vs. excitation power, which can be linearly approximated as indicated by the orange fit. τ_1 at zero excitation power gives the lifetime of the excited state [125, 126]. Hence, the linear

fit in Figure 3-3e yields a lifetime of about 3.8 ns. The second fitting parameter τ_2 describes the metastable state behavior. τ_2 at zero excitation power gives the lifetime of the metastable state, which we found from the fit in Figure 3-3f to be about 673 ns. The last parameter α, plotted as a function of excitation power in Figure 3-3g, is representative of the amount of bunching caused by the metastable state non-radiative transition. The stronger the bunching, the higher the probability of intersystem crossing. Furthermore, the smaller the α, the more the emitter behaves as a two-level system.

Figure 3-3h shows as a function of excitation power the decay ratio, defined as the ratio of the decay rate from the excited state to the ground state versus all first order decay rates from the excited state (decay rate from the excited state to the ground state and decay rate from the excited state to the metastable state). The decay ratio from the excited state to the metastable state is constant for an ideal three-level model. Our experimental decay ratio versus power agrees with that, showing that the three-level system describes the type A emitter well and higher order levels transitions can be neglected.

3.5 Photophysical Characterization of Emitters

We use fluorescence lifetime measurements to compare with the lifetime values found previously to see how well the three-level system models our emitters. We can use the single exponential equation $I(t) \sim \exp(-t/\tau)$ for fitting the time-dependent PL intensity for the single state decay, in which τ represents the lifetime of the excited state. Figure 3-4b shows the excited state lifetime measurement using a pulsed excitation laser with central wavelength of 532 nm, 10 nm bandwidth, pulse length of 1 ns, and 39 MHz repetition rate. The single-exponential fit indicates an excited state $|e\rangle$ lifetime of 3.1 $\pm$ 0.1 ns for the type A emitter and 1.7 $\pm$ 0.1 ns for the type B emitter. The measured lifetime of the type A emitter is consistent with the lifetime values extrapolated from the power dependent $g^{(2)}(\tau)$ measurements, supporting that a three-level system is a suitable model for the type A emitters.

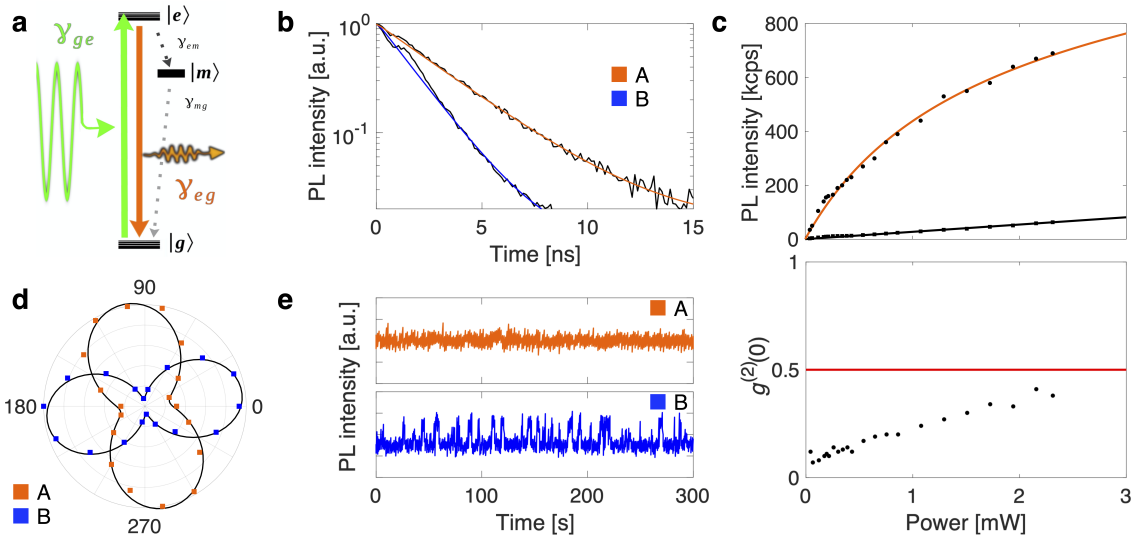

Figure 3-4: Photophysical properties of emitters. (a) Graphical illustration of a three-level system. (b) Excited state lifetime measurements fitted with a single exponential decay function, showing an excited state lifetime of 3.1 ± 0.1 ns for type A emitters (orange) and 1.7 ± 0.1 ns for type B emitters (blue). (c) (top) PL intensity saturation response of a type A emitter exceeding 1 million counts per second at saturation, with a saturation power of 1.5 mW (data with orange fit). The data with black fit shows the associated background. (bottom) Plot of $g^{(2)}(0)$ as a function of excitation power, showing the high single photon emission purity up to twice the saturation power. Red line indicates the cutoff of $g^{(2)}(0) < 0.5$, indicating single photon emission. (d) Polar plots of PL as a function of linear excitation laser polarization. The emitters are split into two classes of emitters: one with a linearly oriented emission polarization orthogonal to the excitation spectrum (type A) and one with a linearly oriented emission polarization parallel to the excitation (type B). (e) Top: long-time photostability of a type A emitter. The emitter did not show any evidence of blinking or bleaching during the course of the experiments. Bottom: photostability of a type B emitter, showing blinking at sub-second timescales.

Figure 3-4d shows the polar plots of the excitation-polarization-dependent PL intensity (without background subtraction) of both types of emitters fitted with a quadratic sinusoidal fit function $\sin^2(\theta+\phi)$, where the angular parameter θ represents the rotation of the linearly polarized pump laser and ϕ represents the orientation of the emitter relative to an arbitrary axis. Both types of emitters are shown to be single linearly polarized dipoles. Type A emitters have excitation and emission polarizations orthogonal to each other, while type B emitters have excitation and emission polarizations parallel to each other.

We next measured the PL intensity of the emitters as a function of the excitation power (with optimized polarization) to find the emitters' maximum emission rates. We used a second room temperature confocal microscope setup for these measurements, designed for efficient PL collection by using a Nikon 1.3 NA oil immersion objective for excitation and collection, as well as using a dichroic filter with 552 nm cut-off wavelength and a 560 nm longpass filter to remove the excitation laser and Raman lines. Figure 3-4c (top) shows the saturation behavior of a type A emitter and the associated background.

Equation 3.2 describes the typical function for fitting the emission count rate I as a function of the measured excitation power P for a three-level system:

$$I(P) = I_\infty \frac{P}{P_{\text{sat}} + P} + \alpha P + \beta \tag{3.2}$$

where I_∞ is the emission rate at saturation, P_{sat} is the excitation power at saturation, α is the linear power-dependent background slope, and β is the constant dark counts. We use Equation 3.2 to fit the intensity saturation behavior measurement plotted in Figure 3-4c (top), which shows that the PL intensity exceeds 1×10^6 cps at saturation, with a saturation power of 1.5 mW. Figure 3-4c (bottom) shows the $g^{(2)}(0)$ of the corresponding second-order autocorrelation measurements for each of the excitation powers used in Figure 3-4c (top), indicating single photon emission characteristics for the emitter up to excitation powers of 3 mW, or twice the saturation power.

3.6 Photonic Integration of Emitters

Next, we created these QEs in AlN-on-sapphire PICs fabricated by a combination of electron beam lithography and dry etching (see Methods). The blue inset in Figure 3-1a is a microscope image of the fabricated QE-integrated waveguides coupled off chip with edge couplers; the grating couplers are used for visual feedback during fiber edge coupling. Using the same room-temperature confocal microscopy setup with 0.9 NA objective described above for laser excitation, we used a cleaved Nufern UHNA3

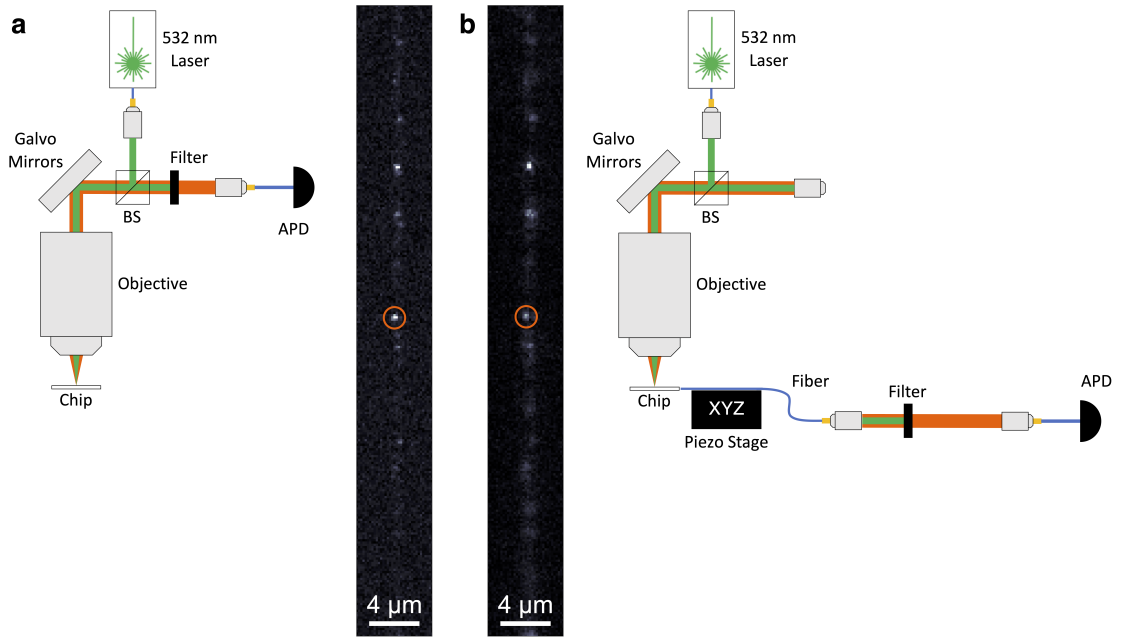

Figure 3-5: Photonic integration of emitters. Confocal PL scan of AlN waveguide populated with quantum emitters throughout, with (a) confocal collection and (b) waveguide collection for detection. The circled emitter is the emitter that is studied in the photon-intensity correlation measurements. Diagrams of the respective measurement setup is shown for each confocal PL scan for clarity.

fiber mounted on a XYZ piezo stage for edge-coupling to the AlN edge couplers, as illustrated conceptually in Figure 3-1a. Our edge coupler design was not optimized to mode match with the UHNA3 fiber. We expect the experimental coupling efficiency to be less than 7% due to it being sensitive to the edge coupler polishing quality [120].

The confocal PL scan in Figure 3-5a with confocal collection for detection of an AlN waveguide indicates QEs throughout, while Figure 3-5b shows the same confocal PL scan with waveguide edge coupler collection into the UHNA3 fiber for detection. A comparison between the scans shows that all emitters are coupled into the waveguide. We use the circled emitter for the subsequent photon intensity correlation measurements.

We observe strongly antibunched emission from waveguide-coupled emission (Figure 3-6a) and cross-correlation measurements (top versus waveguide collection, Figure 3-6b) with 532 nm, 1 mW CW excitation at room temperature without background correction. Despite the rather low estimated edge-coupling efficiency of 7%, we ob-

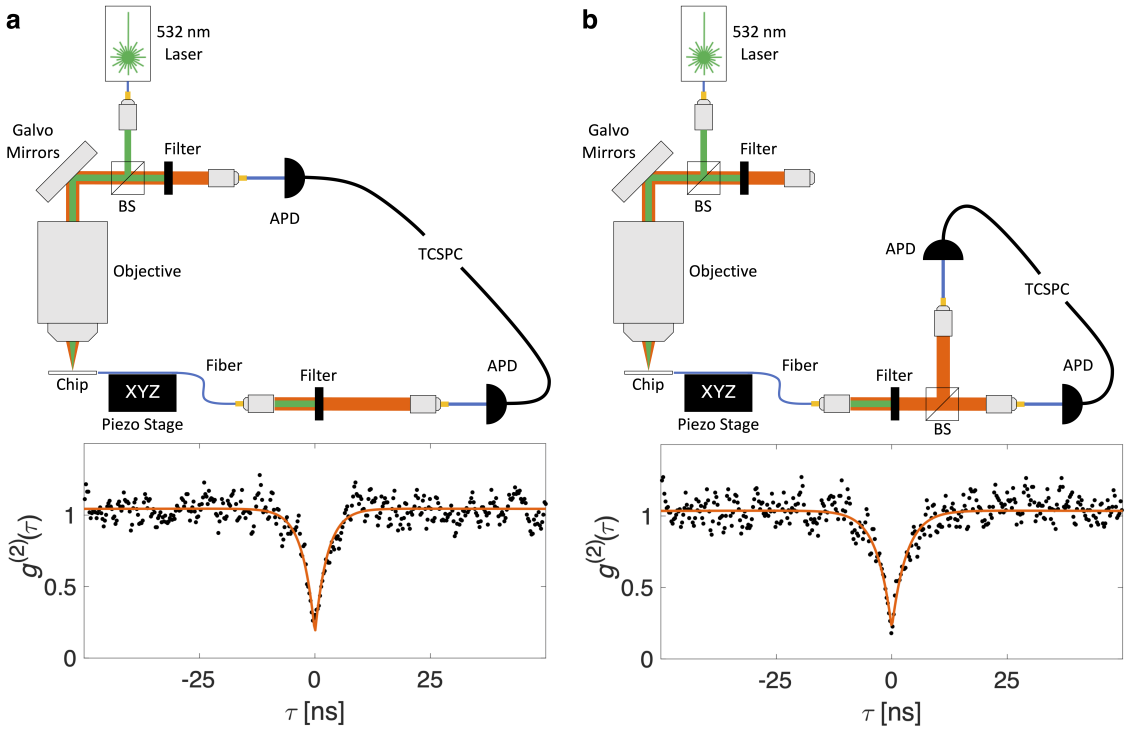

Figure 3-6: Waveguide-coupled emitter photon statistics measurements. (a) Cross-correlation measurement of the emitter under 532 nm excitation between the photons collected via the confocal setup and the photons collected through the waveguide, with $g^{(2)}(0) = 0.17 \pm 0.07$, confirming the photons collected from the waveguide while exciting the emitter originates from the emitter. The upper diagram shows the measurement setup used for the cross-correlation measurement. (b) Autocorrelation measurement of the emitter via waveguide collection only, with $g^{(2)}(0) = 0.21 \pm 0.08$. The upper diagram shows the measurement setup used for the autocorrelation measurement.

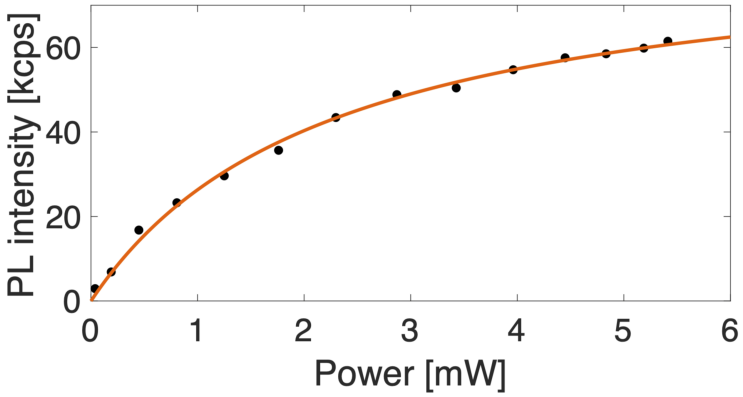

Figure 3-7: PL intensity saturation response of an emitter with waveguide collection, with counts exceeding 8.6×10^4 cps at a saturation power of 2.3 mW.

serve a high count rate exceeding 6×10^4 cps out of the waveguide (Figure 3-7), with 8.6×10^4 cps at a saturation power of 2.3 mW.

We show in Figure 3-8 several exemplary devices realized on the same AlN-on-sapphire platform, though not characterized in this study. Distributed Bragg reflectors can be used as directional reflectors (red boxes) to direct all the emission towards one side of the photonic circuit, as well as spectral filters (green boxes) to filter out excitation light that is scattered into the waveguide. After the spectral filter, the emission can be either first split by an on-chip beamsplitter or directly coupled off the chip via edge couplers or grating couplers that can be placed anywhere throughout the chip (blue boxes).

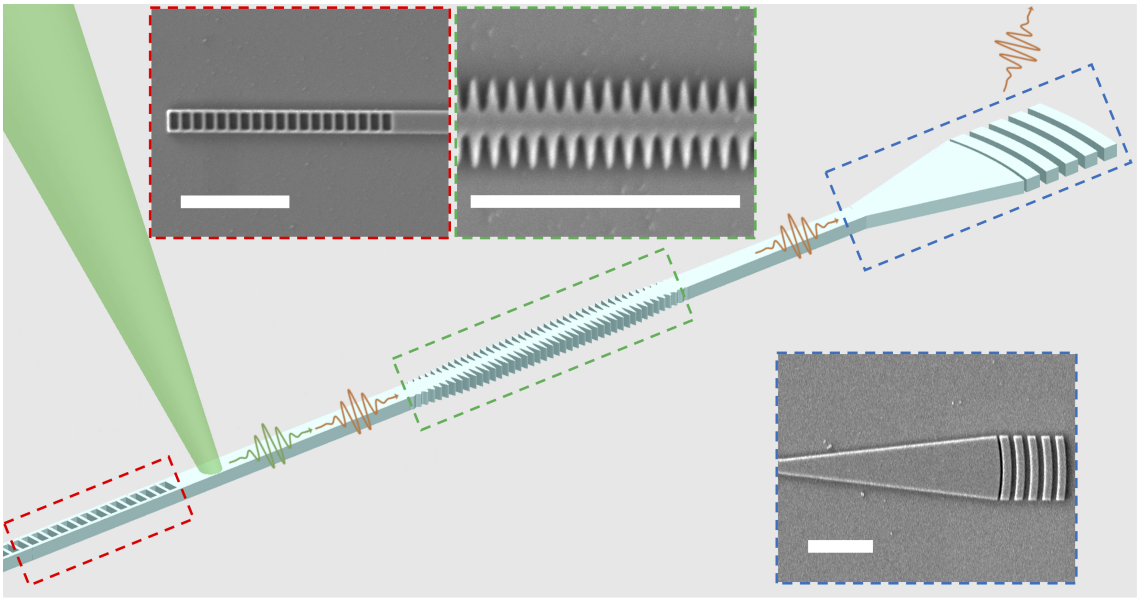

Figure 3-8: Conceptual diagram of an AlN PIC with distributed Bragg reflectors as filter (green) and directional reflector (red), as well as grating coupler (blue) for dense population of read-out channels on the chip. Insets are SEM micrographs of the fabricated structures, with scale bars in each being 2 μm.

3.7 Conclusions and Outlook

While we observed the formation of the QEs after He-ion implantation and annealing, both type A and B QEs are also observed for samples that did not undergo He-ion implantation, albeit at a lower density, making it likely that the emitter type is either

intrinsic or vacancy-based. Some sort of marker indicators on the bulk sample that are inert and do not degrade with the material treatments are needed to do a more careful study on the He-ion dose's effect on the QE formation and properties. As our emitters are in a 200 nm thick AlN film, we speculate from their stronger blinking behavior that type B emitters may be closer to the surfaces [113].

There have been many previous works reporting on quantum emitters in other nitride materials with emission wavelengths covering a wide wavelength range similar to the emitters in this work [113, 114, 127]. However, even with extensive theoretical density functional theory (DFT) modeling, the origin of these other emitter defects is not fully understood [128]. Our QEs in thin film AlN offer insights and potential future research directions to reveal the origins of similar QEs that have been observed in both monolayer and microns thick bulk nitride materials, such as the possibility of direct 3D atomic reconstruction by scanning transmission electron microscopy [129].

In conclusion, we demonstrated quantum emitters in a 200 nm thin-film AlN grown on top of sapphire, with count rates exceeding 1 million cps at saturation and high purity even at room temperature. We also showed that these QEs can be readily integrated in AlN-on-sapphire PICs using conventional AlN fabrication processes for patterning photonic components. While further studies are needed to investigate the predicted spin-dependent transitions coupling to spin qubits, strain-driven spin control, and other avenues towards spectrally narrower emission, the integration of stable QEs into AlN-on-sapphire PICs already opens the prospect of stable single photon sources integrated monolithically with optical modulators [52], AlN-integrated single photon detectors [130], and frequency conversion devices [59]. Furthermore, this work shows the potential of integrating high-quality QEs to a wide range of technologies comprised of the aluminum gallium nitride (AlGaN) family of materials that, thanks to their exceptional optical and electronic properties, as well as a large and growing industrial base, already form the state-of-the-art for applications in UV lasers, piezoelectric actuators and filters, high-power and high-speed electronics, and solid state lighting [131–133].

3.8 Supporting Information

This section includes useful technical details for this chapter.

3.8.1 Material Processing

We ion-implanted the samples using a He ion microscope (Zeiss ORION NanoFab) at a He ion fluence of around 10^{15} ions/cm^2, with acceleration voltage of 32 keV, similar to previous methods for creating isolated defects in hBN [134]. We found that this He ion implantation by itself significantly increased the overall AlN PL but did not increase the detectable emitter density. Instead, annealing the AlN samples after He ion implantation creates resolvable photostable QEs. Each sample is annealed in an ambient pressure argon environment. The sample is increased with a slope of 2°C/s under continuous gas flow. The temperature is kept constant for 30 min once the maximum defined temperature is reached before cooling down to room temperature again. The samples do not reveal any isolated QEs due to a resulting spatially uniform background fluorescence after annealing up to 700°C. The background PL intensity decays exponentially in time when optically pumping the material with the 532 nm excitation laser. Increasing the maximum annealing temperature yields faster exponentially decaying background fluorescence under optical excitation. Isolated and photostable QEs start being detectable at annealing temperatures above 800°C.

3.8.2 AlN Photonics

Development of integrated photonic circuits relies on the use of thin film high index material on a low index substrate. As we show that our material treatment results in the creation of high-purity quantum emitters in a thin AlN film with just 200 nm thickness, we further investigate whether the emitters can survive nanofabrication processes and be integrated with PICs. After emitter formation using the He ion implantation and annealing procedures described above, we fabricated PICs into the AlN thin film by using the electron beam lithography and chlorine reactive ion etching process developed previously in Chapter 2 [44]. Then, S1813 photoresist served as a

protective layer for mechanical edge polishing, which we applied by spin coating the S1813 photoresist at 3000 rpm for 60 seconds with an acceleration of 1000 rpm/s, followed by baking at 110°C for 5 minutes. We diced the chip using an automatic dicing saw (DISCO DAD-3240) and polished the chip by sequentially reducing the grit sizes (30 μm to 0.1 μm) until the polished facet was within the edge coupler taper region to produce optical-grade facets for edge coupling (Allied MultiPrep Polishing System 8). Finally, sonication in N-Methyl-2-Pyrrolidone (NMP) for 30 minutes removes the S1813 protective layer and debris caused by dicing and mechanical polishing.

3.8.3 Experimental Setup

The room temperature characterizations were performed using a confocal microscope. A green 532 nm laser (Coherent Verdi G5 laser) was used for excitation, with photoluminescence scans taken with a galvanometer mirror scanner in a 4F configuration. We measured second-order autocorrelation photon statistics of the emitters with a free-space Hanbury Brown Twiss (HBT) interferometer and detection using fiber-coupled Excelitas avalanche photodiodes (APDs). To measure the excited state lifetime of single emitters, we used time-correlated single photon counting (PicoHarp 300) and a pulsed laser source (SuperK). For low temperature measurements, we used a closed-cycle helium cryostat with a base temperature of 4 K (Montana Instruments) with a built-in objective (NA = 0.9) and detection using free-space Excelitas APDs for confocal microscopy. Spectra were taken with a Princeton Instruments Isoplane SCT320 spectrometer with a resolution of 0.07 ± 0.01 nm. A third confocal microscope setup with NA = 1.3 oil-immersion microscope objective and free-space APDs was used for high efficiency collection measurements.

3.8.4 PIC to Fiber Edge Coupling

Our edge coupler design was not optimized to mode match with the UHNA3 fiber, which is multimode at our wavelengths of interest. The theoretical out-coupling efficiency into the fundamental fiber mode from the 450 nm × 200 nm AlN waveguide is

on average 32% for over the span of 590 nm to 690 nm in wavelength when coupled optimally for 640 nm; there is also 2% coupling into higher order modes. The theoretical efficiency was calculated using 3D Finite-Difference Time-Domain (FDTD) method (Lumerical Inc.). We expect the experimental coupling efficiency to be less than 7% due to it being sensitive to the edge coupler polishing quality [120]. Experimentally, we placed a half-wave plate before the objective of the confocal microscope in order to minimize the laser coupling into the waveguide mode.

Chapter 4

Large-Scale Integration of Quantum Memories in Diamond to AlN Photonic Circuits

Materials presented in this chapter have been previously published, and the text in this chapter is reproduced from this publication (Nature **583** (7815), 226-231 (2020) [120]).

4.1 Background on Color Centers in Diamond

Artificial atom qubits in diamond combine spin clusters with minute-scale coherence times [7] and efficient spin-photon interfaces [6], making them attractive for processing and distributing quantum information [1, 2]. In particular, proposed quantum repeaters for long-range, high-speed quantum networks will require hundreds or more memory qubits [1, 11, 12], whereas error-corrected quantum computing may require millions or more [13–15, 47]. However, a critical barrier standing in the way of large-scale quantum information processing (QIP) is the low device yield of functional qubit systems. Furthermore, although individual spin-photon interfaces can now achieve excellent performance, the lack of active chip-integrated photonic components and wafer-scale single-crystal diamond currently limit the scalability of monolithic dia-

mond QIP architectures. A promising method to alleviate these constraints is heterogeneous integration, which is increasingly used in advanced microelectronics to assemble separately fabricated sub-components into a single, multifunctional chip. Such hybrid fabrication have also recently been used to integrate PICs with quantum modules, including quantum dot single-photon sources [32, 33, 135], superconducting nanowire single-photon detectors (SNSPDs) [34], and nitrogen-vacancy (NV) center diamond waveguides [35]. However, these demonstrations assembled components one-by-one, which presents a formidable scaling challenge, and they did not provide for spectral alignment of artificial atoms. Here, we introduce the 'quantum micro-chiplet (QMC)' framework that greatly improves the yield and accuracy of heterogeneously integrated nanoscopic devices. Specifically, this assembly process enables the construction of a 128-channel photonic integrated artificial atom chip containing diamond quantum emitters with high coupling efficiencies, optical coherences near the lifetime limit, and tunable optical frequencies to compensate for spectral inhomogeneities on chip.

4.2 Hybrid Architecture Based On Large-Scale Integrated Photonics

Figure 4-1 illustrates the heterogeneous integration process. The multi-chip module consists of a waveguide layer in single-crystal AlN for low-loss photonics [44, 136], micro-chiplet sockets to optically interface with separately fabricated diamond QMCs, and electrical layers for controlling color center transitions. This PIC platform is compatible with additional components, such as on-chip electro-optic modulators [52] and SNSPDs [34, 130, 137] for photon switching and detection in a quantum photonic chip. Figure 4-2 highlights the flowchart of the large-scale heterogeneous integration process, showing that the multi-chip module and QMCs for heterogeneous integration are co-designed iteratively to optimize the integration mechanism, as well as to be flexible for whatever functionalities are required for the quantum node.

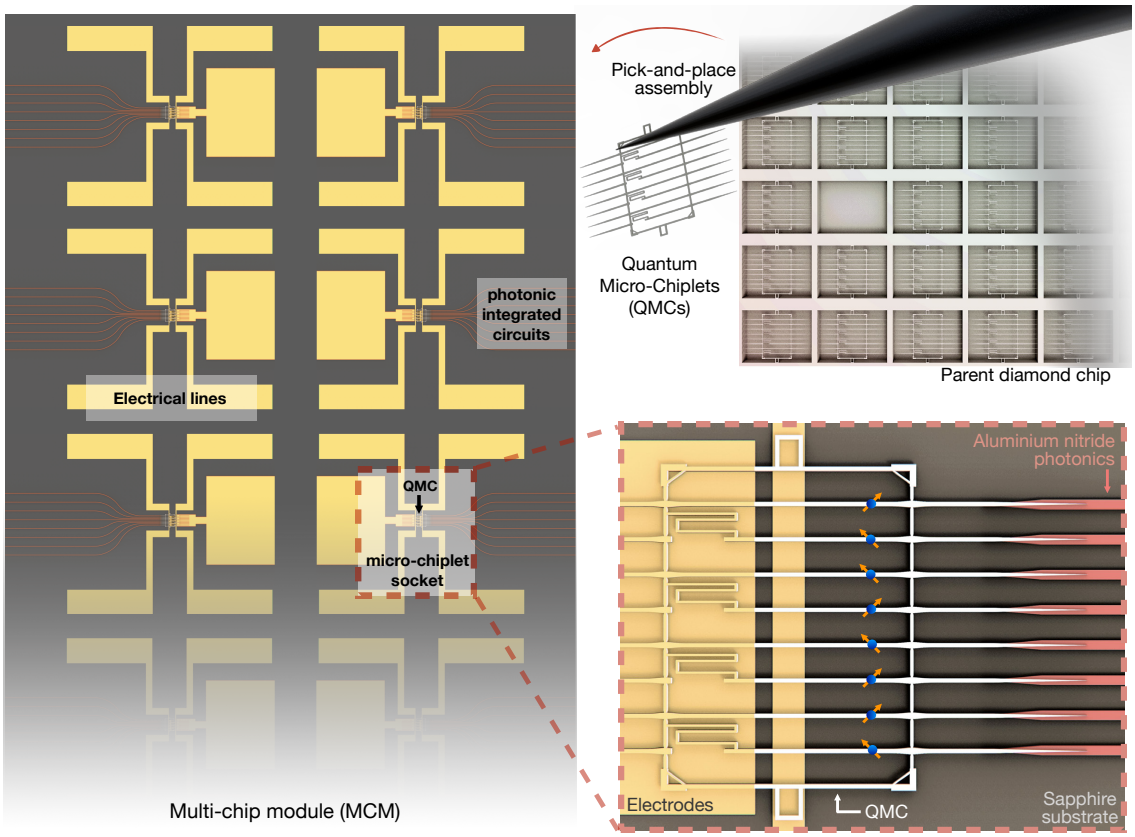

Figure 4-1: Scalable integration of artificial atoms with photonics. The separate fabrication of sub-components before their final assembly maximizes the yield, size, and performance of the hybrid emitter-photonics chip. A pick-and-place method transfers pre-screened QMCs from their parent diamond chip into a socket containing efficient photonic interfaces, as well as electrical wires for controlling color centers.

The large optical transparency of the QMC and PIC materials make them compatible with a variety of quantum emitters. In this work, we consider the negatively charged GeV and SiV centers in diamond with zero-phonon line transitions at 602 nm and 737 nm, respectively, because of their stable optical and spin properties, even in nanophotonic devices [23, 24, 106, 107, 138, 139].

4.3 Fabrication of Diamond-AlN Hybrid System

The process begins with relieving the strained surface of the single-crystal diamond plate (Element6) by plasma etching the first 10 μm of diamond in Ar/Cl_2, followed

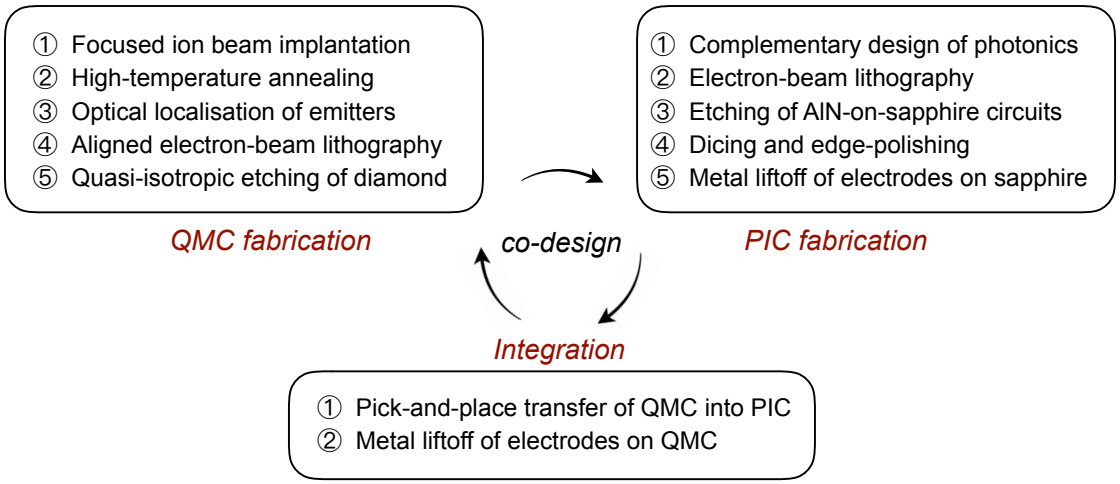

Figure 4-2: Flowchart for large-scale heterogeneous integration.

by another 5 μm etching in pure oxygen plasma. We used a focused ion beam (FIB) tool at the Ion Beam Laboratory (Sandia National Laboratories) to implant Ge ions (spot size ∼35 nm × 43 nm) and Si ions (spot size of ∼50 nm × 45 nm) at an effective areal dose of 2-6 × 10^{11} ions/cm^2 and 4.5-9 × 10^{11} ions/cm^2 [140]. The Ge (Si) ion energy is 200 keV (170 keV), which corresponds to an implantation depth of 74 ± 12 nm (113 ± 19 nm) from stopping and range of ions in matter (SRIM) simulations [141]. We implanted the Ge^+ and Si^+ ion into a 1 μm pitch square array in a single-crystal diamond substrate, followed by high temperature annealing at 1200°C in an ultrahigh vacuum furnace. Finally, we cleaned the diamond in a boiling mixture of 1:1:1 sulphuric acid, nitric acid, and perchloric acid. This process generates spots of tightly localized GeV centers (depth of ∼74 nm, vertical straggle ∼12 nm, lateral FWHM distribution ∼40 nm) and SiV centers (∼113 nm, ∼19 nm, ∼50 nm). We analyzed the conversion yields of GeV and SiV centers by counting the absence of fluorescent spots in our implantation region (1 μm-pitch, square grid) using photoluminescence (PL) microscopy. A Poisson distribution $P(k)$, with mean number of color centers λ and number of observed emitters per spot k, models the stochastic emitter creation process. From the mean $\lambda = -\log(P(0))$ and our implantation dose, we estimate the conversion yield of GeV (SiV) centers to be ∼1.9% (3.2%). We located and mapped the fabricated quantum emitters relative to prefabricated alignment

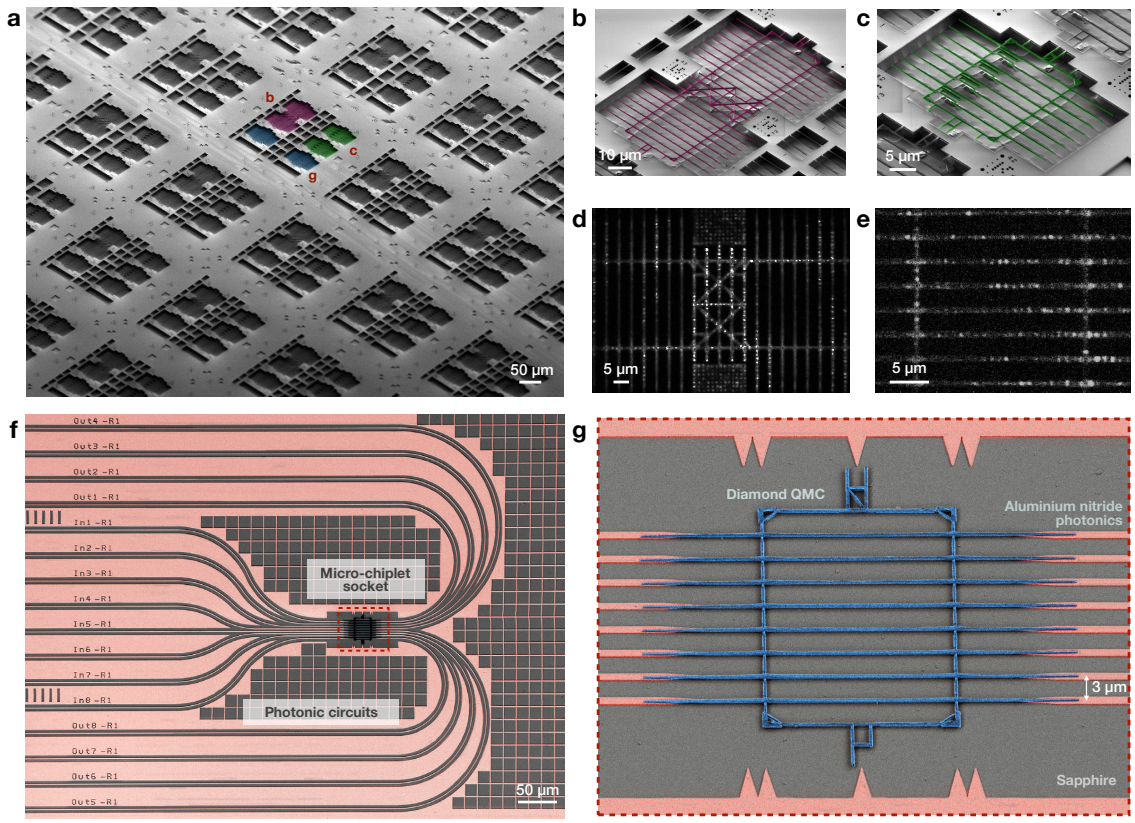

Figure 4-3: Fabrication and integration of QMC with integrated photonics. (a) SEM overview of the parent diamond chip containing over 500 micro-chiplets for heterogeneous integration. (b) A 16-channel QMC. (c) An 8-channel QMC with varying mechanical beam rigidity. (d) PL map of GeV centers (bright spots) in a 16-channel QMC. (e) PL map of SiV centers (bright spots) in a defect-free 8-channel QMC. (f) An AlN-on-sapphire integrated photonics module that interfaces with the diamond QMC placed in the chiplet socket. (g) Close-up SEM of the diamond QMC and AlN photonic interfaces.

markers using a wide-field and confocal scanning microscope as shown previously [142]. To demonstrate the microchiplet principle in this study, we registered the qubit grid, rather than each emitter's location. In particular, we determined the global displacement of the emitter grid from the implantation process and used this offset in our subsequent electron-beam lithography of QMCs.

After ion implantation and optical registration, we fabricated the QMCs over the emitter arrays using a combination of electron-beam lithography (EBL) and quasi-isotropic etching [143, 144]. In particular, we deposited 180 nm of silicon nitride (SiN)

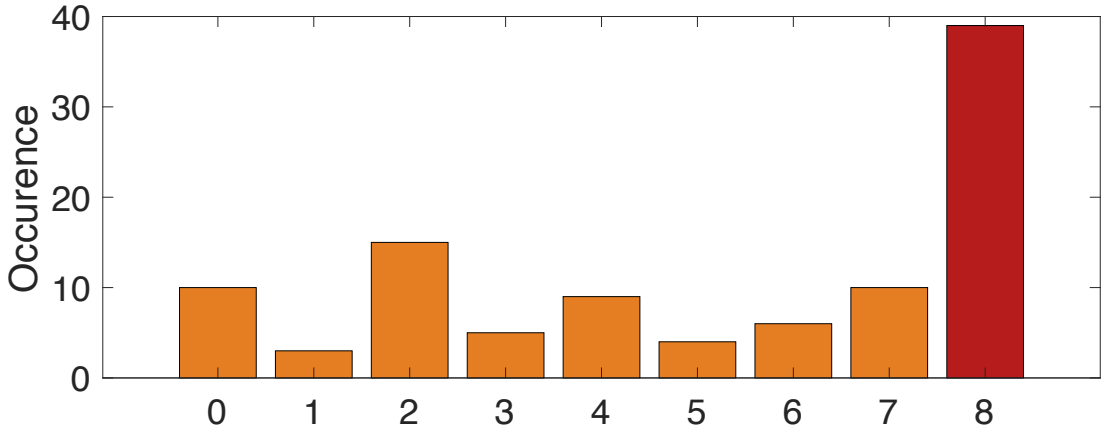

Figure 4-4: Histogram of number of emitter-coupled waveguides within a QMC.

hard mask using plasma-enhanced chemical vapor deposition. We patterned the SiN hard mask using ZEP-520A electron-beam resist with ESpacer conductive polymer and CF_4 reactive-ion etching (RIE). Subsequently, we used inductively-coupled RIE to transfer the pattern from SiN into the diamond layer. Following oxygen etching of the diamond, we deposited 15 nm of conformal alumina via atomic layer deposition (ALD). After a brief breakthrough etch of alumina, we etched the chip in zero-bias oxygen plasma to isotropically undercut the diamond QMCs. Finally, we removed the SiN and alumina masks in hydrofluoric acid. We again annealed the device at 1200°C using the above ultrahigh-vacuum, high temperature annealing recipe, followed by a clean in a boiling mixture of 1:1:1 sulphuric acid, nitric acid, and perchloric acid.

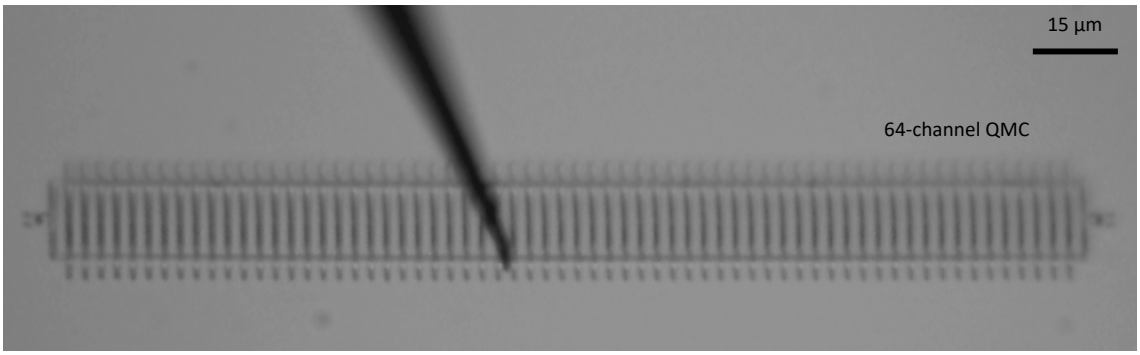

Figure 4-5: Integrating a 64-channel QMC

Figure 4-3a shows a scanning electron microscope (SEM) image of various suspended chiplets containing 8- or 16-channel waveguide arrays connected by diamond

'trusses', as seen in the close-up SEM images in Figure 4-3b,c and Figure 4-3g, respectively. Using PL spectroscopy, we investigated the occurrence of "defect-free" (i.e. they have one or more stable color center per waveguide) 8-channel QMCs, as summarized in Figure 4-4. From this histogram, we estimate the probability of creating defect-free QMCs to be 39%, despite a misalignment between the FIB mask and the QMC patterns. The defect-free yield of the 16-channel QMCs was lower as these are more susceptible to misalignment, so we did not use them in this study. We note that this success probability depends on a variety of factors, including the alignment accuracy of the FIB implantation, the relative calibration between EBL and FIB, as well as the optical registration process. By deterministically placing each element of the QMC over pre-localized single emitters [142, 145–148], it should be possible to boost the yield towards unity, allowing hundreds or thousands of quantum channels per chiplet. Such approaches may also be critical for reducing the proximity of nanofabricated surfaces to emitters and for coupling to photonic crystal nanocavities. Structurally, much larger arrays are fabricable and integrable: we successfully transferred QMCs with as many as 64 waveguide components (see Figure 4-5).

We fabricated the PIC that the QMCs are later transferred to on a wafer of single-crystal AlN on a sapphire substrate using EBL and chlorine reactive ion etching. AlN-on-sapphire is a suitable platform for linear and nonlinear quantum photonics because of its large bandgap (∼6.2 eV), high material nonlinearities [52, 57, 59, 99], and low narrowband background fluorescence in the spectrum (600-760 nm) of GeV and SiV centers [44]. In this work, we used a wafer of 200 nm thick single-crystal AlN on a sapphire substrate (MSE Supplies, grown by hydride vapor phase epitaxy). Prior to processing of the AlN PIC, we patterned gold alignment markers to use for alignment between the photonic layer and the metal layers for strain tuning. We defined the AlN photonic circuitry using EBL (ZEP-520A electron-beam resist and ESpacer conductive polymer) and chlorine-based inductively-coupled plasma reactive-ion etching (ICP-RIE) developed previously in Chapter 2 [44]. Then, S1813 photoresist served as a protective layer for mechanical edge polishing. We then diced the chip using an automatic dicing saw (DISCO DAD-3240). Finally, we polished the chip in order to

produce optical-grade facets for edge coupling (Allied MultiPrep Polishing System 8). Finally, sonication in N-Methyl-2-Pyrrolidone (NMP) removes the S1813 protective layer and debris caused by dicing and mechanical polishing.

The fabrication of the metal electrodes and contact pads on top of the PIC substrate immediately followed the patterning of the thin-film AlN and preceded the chip dicing and edge polishing. The PIC substrate metal layer was defined by liftoff of 50 nm Au on top of 5 nm Ti using a single layer of A6 950K PMMA electron-beam resist (450 nm thick), which was aligned relative to the AlN PIC with metal alignment markers. Then, the fabrication of the AlN photonic circuitry proceeded to dicing and polishing, followed by integration of the QMC. After pick-and-place transfer of the QMC to the micro-chiplet socket, we used a targeted electron-beam metal deposition process to place platinum on the periphery of the QMC for electrical connection (FEI Helios NanoLab 600 DualBeam). This process also locked the QMC into place before resist spin-coating. Finally, we defined the metal electrode layer on top of the QMC by liftoff of 15 nm Au on 5 nm Ti using a single layer of A11 950K PMMA (2 μm thick).

Using piezo-controlled 3-axis and rotation micro-manipulators, we aligned and transferred QMCs into the micro-chiplet sockets with a placement success rate of 90%. Figure 4-3f shows one of twenty micro-chiplet sockets connecting 8 input and 8 output waveguide arrays to an 8-channel QMC. In addition to the AlN waveguides, the QMC also rests on top of multiple small AlN pedestals to prevent bowing of the diamond structures and stiction with the underlying sapphire substrate. In the case of an inaccurate placement, both the QMC and socket can be reused simply by picking the QMC and re-attempting the placement process. Experimentally, we have transferred a variety of arrays, ranging from single-channel devices all the way to 64-channel QMCs (see Figure 4-5). We expect computer-controlled placement and self-alignment locking features to improve the transfer rate and to potentially fully automate the process.

The diamond waveguides (width 340 nm, height 200 nm) transfer light into the AlN waveguides (width 800 nm, height 200 nm) through inverse tapered sections with

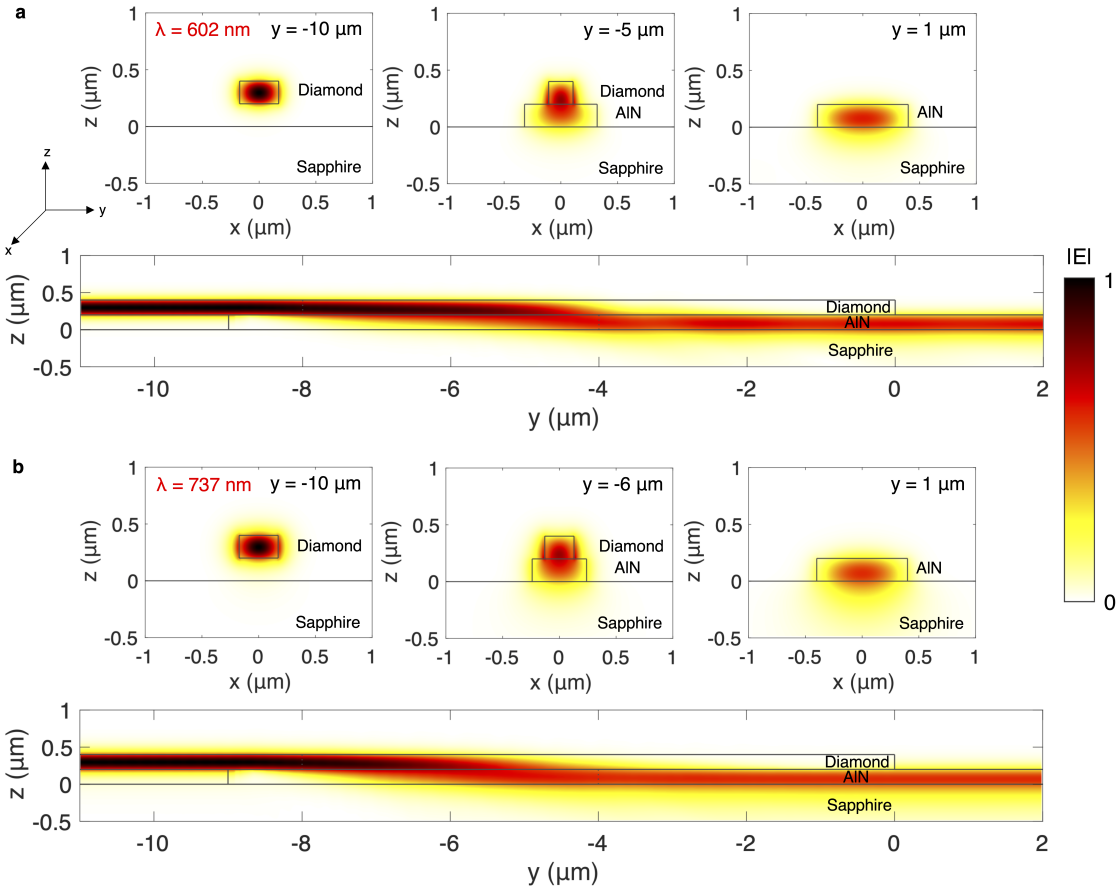

Figure 4-6: FDTD simulation showing propagation of light from the diamond waveguide into the AlN waveguide for: (a) 602 nm wavelength (corresponding to the GeV color center ZPL) and (b) 737 nm wavelength (corresponding to the SiV color center ZPL).

simulated efficiency of 97% (98%) at 602 nm (737 nm) wavelength. Figure 4-6a(b) shows the normalized |E| field of 602 nm (737 nm) wavelength transverse electric (TE) light coupling from the diamond waveguide (340 nm x 200 nm) to the bottom AlN waveguide (800 nm x 200 nm), calculated using the 3D finite-difference time-domain FDTD method (Lumerical Inc.). The light transfers adiabatically via tapered sections in the diamond waveguide and AlN waveguide. Here, the coupling region is 9 μm long, with a diamond taper length of 8 μm and AlN taper length of 5 μm. The top insets show 2D transverse cross sections of the light propagation. The cross sections at y = −10 and y = 1 μm correspond to the fundamental TE mode of the diamond waveguide and AlN-on-sapphire waveguide, respectively. The cross section at y =

-5 μm (y = -6 μm) is the point where half of the light launched from the diamond waveguide is transferred to the AlN waveguide at 602 nm (737 nm) wavelength. The light from the diamond waveguide couples to the AlN waveguide with 97% (98%) efficiency at these wavelengths, with all of the light coupling preferentially to the AlN fundamental TE mode and negligible coupling to higher order modes. This optimized device geometry was determined by optimizing for the coupling efficiency from the fundamental TE mode of the diamond waveguide to the fundamental TE mode of the AlN while sweeping the diamond taper length, the AlN taper length, and the overlap region between the diamond and AlN waveguides.

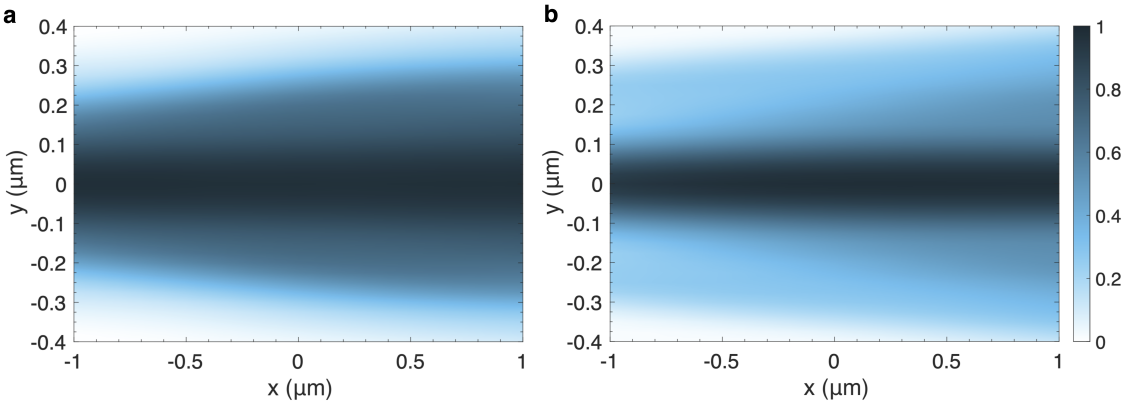

Figure 4-7: Coupling efficiency of TE mode light from the diamond waveguide into the AlN waveguide as a function of offset to the optimum alignment for: (a) ZPL of GeV centers at 602 nm and (b) ZPL of SiV centers at 737 nm.

The SEM image of an assembled device in Figure 4-3g shows a transverse placement error of (38 ± 16) nm. For such typical errors, simulations indicate a drop in coupling efficiency to 93% (89%) at 602 nm (737 nm) wavelength (see Figure 4-7). Hence, we have a 0.46 dB tolerance in the coupling efficiency within our transfer placement accuracy. By directly measuring the PIC-diamond-PIC transmission efficiency, we found the interlayer coupling efficiency to be greater than 34%, which was lower than simulations likely due to scattering at the interfaces and the QMC cross-junctions.

We find that the transfer of the QMCs is substantially easier than for individual waveguides [35] due to its rigidity and many alignment features. The successful

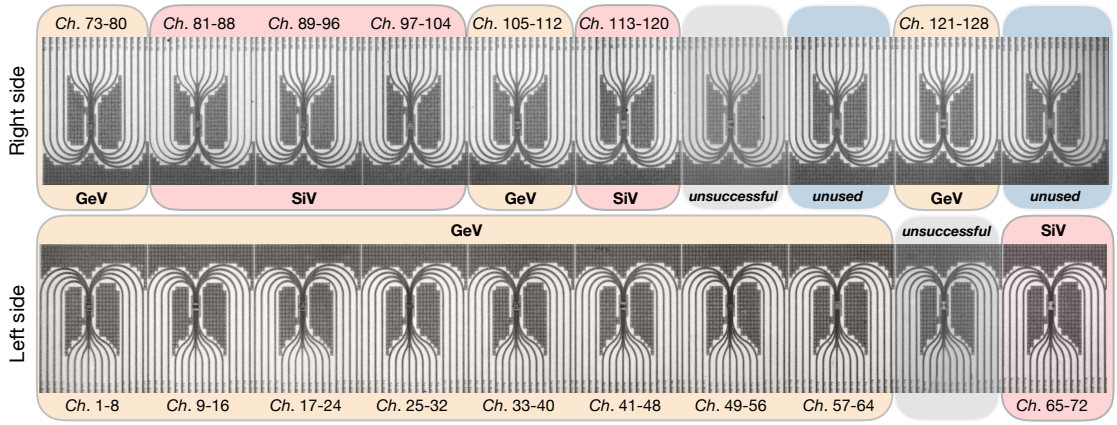

Figure 4-8: Optical image of sixteen QMC-populated micro-chiplet sockets containing GeV or SiV centers. The 'unsuccessful' modules indicate failed QMC placements.

transfer of 16 defect-free chiplets results in a 128-channel photonically integrated quantum emitter chip (see Figure 4-8), as characterized below.

4.4 Integrated Quantum Photonics with GeVs and SiVs in Hybrid System

We performed experiments in a closed-cycle cryostat with a base temperature below 4K (Montana Instruments) with a top-access microscope objective (Mitutoyo 100x ULWD, NA = 0.55), as illustrated in Figure 4-9a. We used 3-axis nanoposition steppers (Attocube ANP-x,z-50) and scanners (Attocube ANS-x,z-50) for edge coupling of optical fibers (lensed fiber with a spot size = 0.8 μm at 633 nm, or a Nufern UHNA3 fiber) to the PIC. The optical fiber labeled ① couples pump light (fluorescence) to (from) the QMC via the AlN waveguides. The microscope objective also provides optical access to the QMC, e.g., to a color center (optical interface ②) or a scattering site (③).

We couple laser and PL to and from AlN-on-sapphire waveguides using lensed fibers (Nanonics Imaging Ltd., SM-630 with spot size = 0.8 ± 0.3 μm, working distance = 4 ± 1 μm) for cryostat experiments and ultra-high NA fibers (UNHA3) for room temperature experiments. Under our single-mode operation at 602-737 nm,

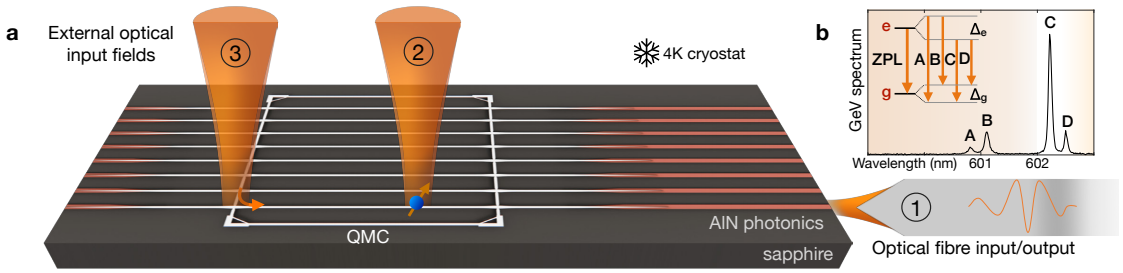

Figure 4-9: Integrated quantum photonics with color centers. (a) Experimental setup in a 4K cryostat showing the input and output optical interfaces ①, ②, and ③. (b) Energy level and spectrum of a GeV center. Resonant excitation probed transition C, which is the brightest and narrowest line.

the in-coupling efficiency is the same as the out-coupling efficiency of AlN waveguide to lensed fiber, which we find to be 51%-57% using the 3D-FDTD method. In practice, the PIC-fiber coupling efficiency, which we find to be 11% in our devices, is sensitive to the edge coupler polishing quality. For the high-NA fiber, which is multimode at our wavelengths of interest, we find the numerical out-coupling efficiency to the fundamental fiber mode to be 25% (34%) at 602 nm (737 nm); there is also 1% (3%) coupling into higher order modes.

Figure 4-9b shows the energy level and emission spectrum of a single GeV when pumped through ② and collected through ①. Off-resonant excitation using 532 nm light with off-chip pump filtering in this configuration enables the rapid identification of single emitters (indicated by a photon intensity autocorrelation function $g^{(2)}(0) < 0.5$). For PL spectroscopy, we filtered the fiber-coupled fluorescence in free space using bandpass filters – Semrock FF01-605/15 for GeV centers and FF01-740/13 for SiV centers. We off-resonantly pumped GeV (SiV) using 532 nm (660 nm) lasers. Figure 4-10a(i) shows a typical photon antibunching ($g^{(2)}(0) = 0.19(7)$) from a single GeV center (Channel 41) pumped near saturation, without background or detector jitter correction. Resonant excitation is achieved using a tunable laser (MSquared SolsTiS with an external mixing module) and filtering the resonance excitation laser from the fiber-coupled fluorescence in free space using bandpass filters – Semrock FF01-647/57 for GeV centers and FF01-775/46 for SiV centers. Under the resonant excitation at 602 nm of the GeV transition C (see Figure 4-9b) of the zero-phonon line (ZPL), the

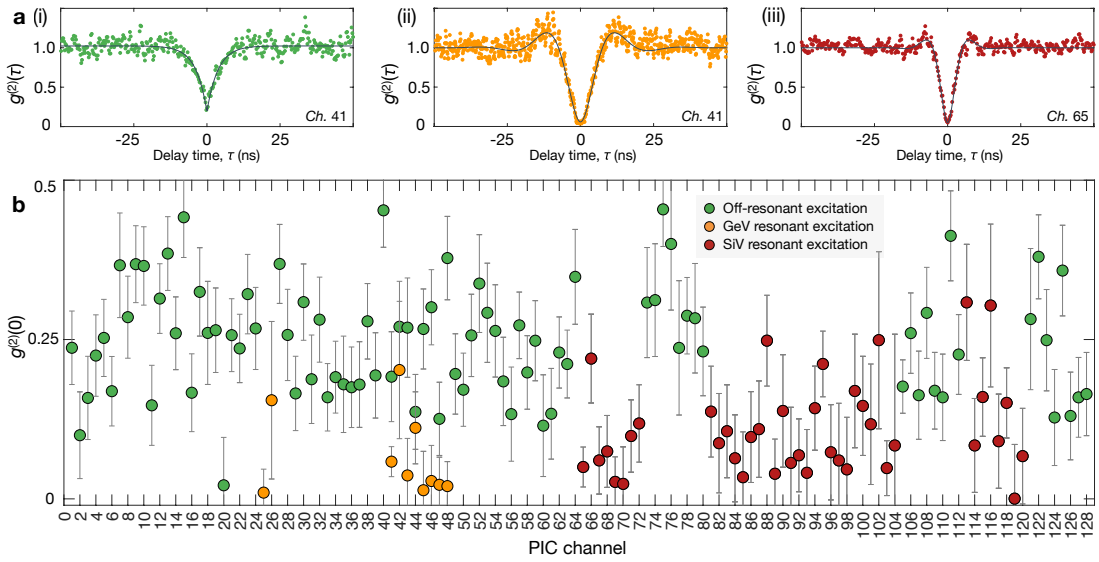

Figure 4-10: (a) Auto-correlation measurements of a single GeV in Channel 41 under (i) off-resonant 2 mW, 532 nm excitation and under (ii) resonant excitation at 602 nm. (iii) Auto-correlation measurement of a single SiV in Channel 65 under resonant excitation at 737 nm. (b) Waveguide-coupled single photons from every integrated GeV and SiV channel in the PIC.

photon purity improves to $g^{(2)}(0) = 0.06(2)$ (Figure 4-10b(ii)). Similarly, in Channel 65 we measured anti-bunched photons with $g^{(2)}(0) = 0.05(3)$ from a single SiV center under resonant excitation at 737 nm (Figure 4-10b(iii)). In all 128 integrated waveguides, shown in Figure 4-8, we identified single GeV and SiV emitters using top excitation ② and fiber-coupled waveguide collection ①, as summarized by their photon statistics in Figure 4-10b.

4.5 High Purity Single Photons from Optically Coherent Waveguide-Coupled Emitters

Next, we investigated the optical coherence of a GeV center using all-fiber spectroscopy. Figure 4-11a shows the photoluminescence excitation (PLE) spectrum of the Channel 41 GeV as we scanned a resonant laser across its ZPL (transition C) with both excitation and detection through the fiber interface ①. For PLE measurements, we used acousto-optic modulators to excite emitters with a resonant pulse and

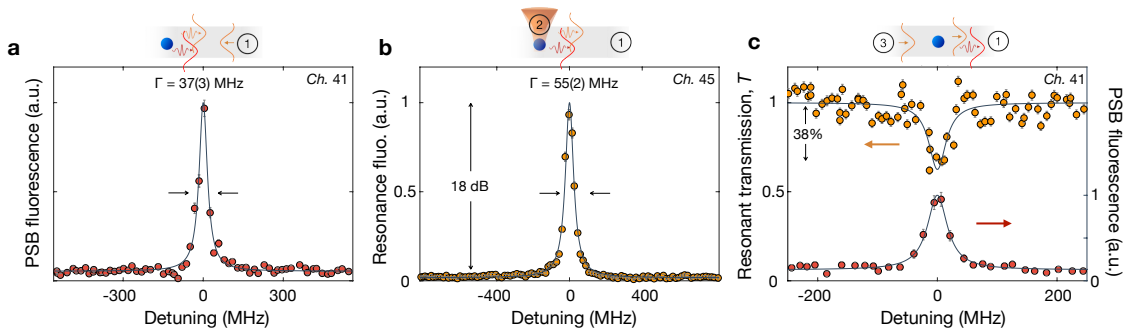

Figure 4-11: Defect-free arrays of optically coherent and efficient waveguide-coupled emitters. (a) Photoluminescence excitation (PLE) spectrum (FWHM linewidth Γ = 37(3) MHz, indicated by the arrows) of a single GeV in channel 41 with all-fiber excitation and detection of the phonon sideband (PSB) fluorescence routed on-chip via ①. (b) Excitation via ② and fluorescence detection via ①. This geometry allows GeV resonance fluorescence detection at least 18 dB above background, without spectral, temporal, or polarization filtering. (c) In transmission, a single GeV center causes coherent extinction of $\Delta T/T$ = 38(9)% (orange curve, Γ = 35(35) MHz); the PLE spectrum is shown in the red curve (Γ = 40(5) MHz).

an optional 532 nm charge repump pulse. Despite the presence of another emitter spectrally detuned by 50 GHz in the same waveguide, resonant excitation allows the selective addressing and readout of single emitters. The measured linewidth of $\Gamma = \Gamma_0 + 2\Gamma_d$ = 37 MHz (3 MHz fit uncertainty) is near the lifetime limit $\Gamma_0 = 1/2\pi\tau$ = 24(2) MHz, obtained from the excited state lifetime τ. To measure the excited state lifetime of single emitters, we used time-correlated single photon counting (PicoHarp 300) and a pulsed laser source (SuperK, filtered to 532 ± 20 nm). We fitted the lifetime curves of the emitters in Figure 4-11a with biexponential terms to account for fast laser decay and the slower fluorescence decay time constant (see Figure 4-12).

The PIC geometry also enables the direct detection of ZPL resonance fluorescence without any spectral, temporal, or polarization filtering, even under resonant excitation. We placed a half-wave plate before Channel ② to minimize laser coupling into the waveguide mode. Figure 4-11b plots the resonance fluorescence obtained for top excitation (②) and waveguide collection without filtering in the detection via ①. By polarizing the pump E-field along the waveguide axis to minimize excitation of the TE waveguide mode, this cross-excitation/detection configuration achieves a ZPL intensity 18 dB above background, comparable to free-space diamond entanglement

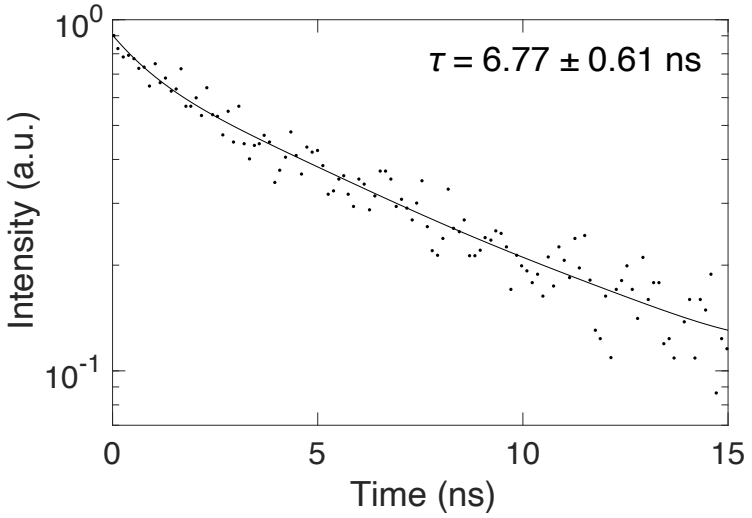

Figure 4-12: Fluorescence decay of the GeV in Channel 41 measured using time-correlated single photon counting.

experiments using cross-polarization and time-gated detection [149].

According to FDTD simulations, an ideal emitter in the optimal configuration has a spontaneous emission coupling efficiency of $\beta = 0.8$ into the diamond waveguide. Experimentally, we measured this efficiency by measuring the transmission of a laser field through a single GeV center (Figure 4-11c). The extinction in the resonant transmission spectrum arises from the interference between the scattered and incoming optical fields, and its depth depends on the dipole-waveguide coupling $\beta = \Gamma_{wg}/(\Gamma_{wg} + \Gamma')$, where Γ_{wg} is the emission rate into the waveguide mode and Γ' the decay rate into all other channels. For the measurement in Figure 4-11c, we first characterized the saturation response of the emitter when excited via ③. At the low-excitation limit, the cooperativity C can be extracted from $T \approx (1 - \beta)^2 = (1 + C)^{-2}$. By also accounting for line broadening of $2\Gamma_d/\Gamma_0 = 0.33(14)$, we determined β via [150]:

$$T = 1 - \frac{(\beta - 2)\beta}{(1 + 2\Gamma_d/\Gamma)(1 + S)} \tag{4.1}$$

which reduces to the usual expression [151] $T \approx (1 - \beta)^2$ in the absence of broadening and far from saturation $S \ll 1$. In this experiment, we operated at $S \approx 10^{-2}$, and all

errors denote the fit or propagated uncertainties.

By injecting a laser field through ③ and monitoring the transmission T via ①, we observed an extinction of $1 - T = 0.38(9)$ when on resonance with the GeV center. This extinction places a lower bound of the emitter-waveguide cooperativity at $C = 0.27(10)$ and $\beta = 0.21(6)$. By accounting for residual line broadening and for the ZPL emission fraction ($\sim$0.6), the dipole-waveguide coupling efficiency is at least 0.55(18). The discrepancy of the experimental corrected $\beta = 0.55(18)$ with the simulated $\beta = 0.8$ using the 3D FDTD method arises from three possible sources: (1) angular and positional misalignment of the dipole in the waveguide, (2) finite population in the upper ground state and emission into transition D, and (3) possible non-radiative processes.

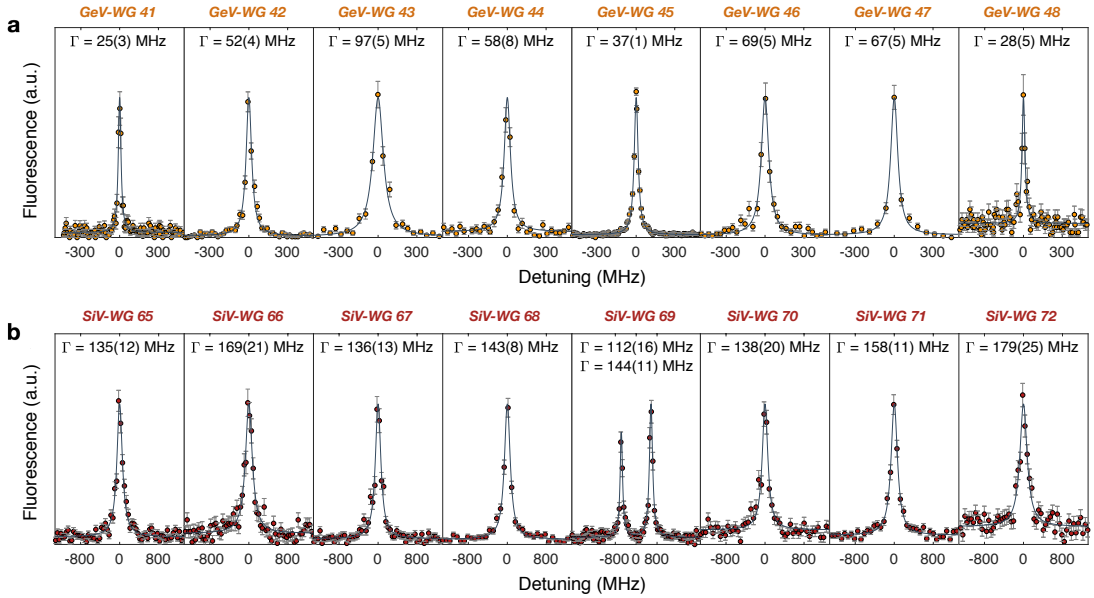

Figure 4-13: (a) PLE spectra of GeV centers in each waveguide of a characteristic 8-channel GeV QMC, with a mean (± standard deviation) linewidth of $\Gamma = 54$ (± 24) MHz. (b) PLE spectra of SiVs in an 8-channel SiV QMC, with a mean linewidth $\Gamma = 146$ (± 20) MHz. We interpret the two lines in Channel 69 as PLE spectra from two distinct SiV centers [$g^{(2)}(0) = 0.69(7)$ under off-resonant excitation (not shown)]

The excellent coherence of the GeV center in Channel 41 is not unique. Figure 4-13a reports the linewidths of every channel in a characteristic 8-channel GeV diamond chiplet, all measured through the on-chip routing of fluorescence into an optical

fiber. We find a mean ± standard deviation normalized linewidth of $\Gamma/\Gamma_0 = 1.7 \pm 0.7$, with GeV channels 41, 45, and 48 exhibiting lifetime-limited values of 1.0(2), 0.9(1), and 1.0(2), respectively. From these measurements, we also obtained the inhomogeneous ZPL transition frequency distribution of 85 GHz. In these PLE measurements, we averaged each spectrum over ∼5 minutes (5000 experiments), demonstrating the emitters' long-term stability after heterogeneous integration. Similarly, as shown in Figure 4-13b, we also find uniformly narrow lines from SiV centers across a QMC, with linewidths within a factor of $\Gamma/\Gamma_0 = 1.6 \pm 0.2$ from SiV centers in bulk diamond [152], and with an inhomogeneous frequency distribution of 30 GHz.

4.6 Controlling the GeV Optical Transitions via Strain

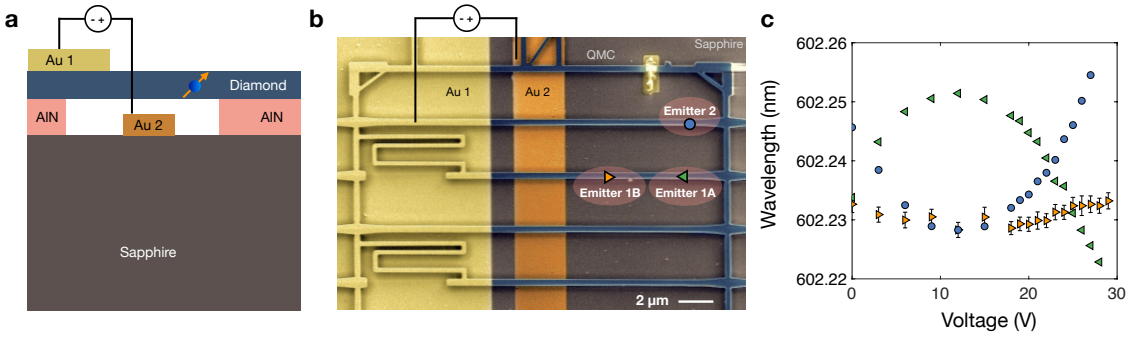

Figure 4-14: Controlling the optical transitions of color centers on a PIC. (a) We applied a DC bias between the metal layer Au 1 on diamond and metal Au 2 on the substrate to electrostatically actuate the QMC. (b) SEM image of the device. In this experiment, we investigated the optical response of emitters 1A, 1B, and 2 to strain. (c) Intra-waveguide Emitter 1A and Emitter 1B overlap spectrally at 24.5 V. Inter-waveguide overlapping between Emitter 2 and Emitter 1A (1B) occurs at 2 V (12 V). Error bars for Emitter 1A and Emitter 2 are smaller than the data points.

To overcome the inhomogeneous spread in transition frequencies, we implemented a strain-tuning scheme using the electrical layers in our PIC. The fabricated device (Figure 4-14a,b) uses a QMC that consists of waveguides with different lengths and beam rigidities (Figure 4-15). Strain is applied by a capacitive actuator consisting of

one gold electrode (Au 1) on the QMC layer, separated transversely by 1.5 μm from a gold ground plane (Au 2) on the sapphire substrate.

4.6.1 Strain tuning scheme of QMC on PIC

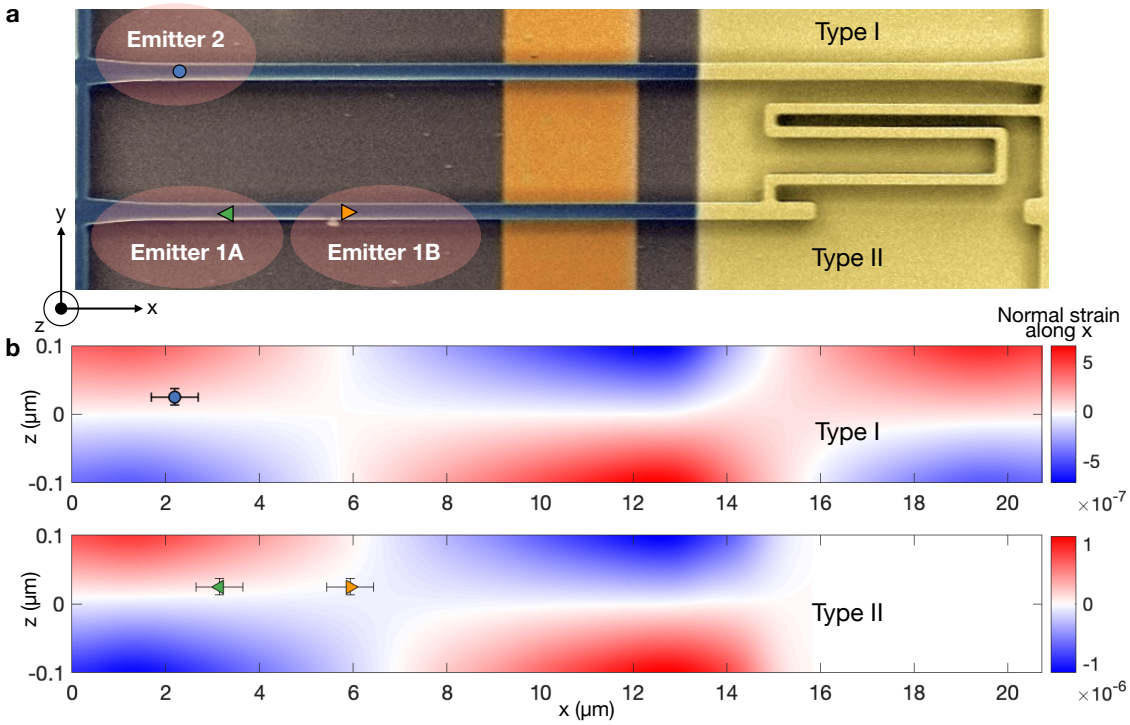

Figure 4-15: Scheme for strain-tuning emitters in a PIC platform. (a) Scanning electron micrograph image of Type I and Type II waveguides considered in this experiment. (b) Strain distribution along the waveguides and emitters considered in Figure 4-14. Horizontal error bars indicate the lateral uncertainty in the position of emitters and vertical error bars indicate the ion implantation straggle.

We introduced different optical responses to our emitter-QMC by changing the length of their constituent waveguides. Here, we used waveguides of length 20 μm (Type I) and length 15 μm (Type II). To be compatible with the QMC framework, we included a flexible bridge between Type II waveguides and the QMC body (see Figure 4-14a and Figure 4-15a). Figure 4-15b confirms the difference in strain response at 30 V (modeled using COMSOL Multiphysics) between Type I and Type II waveguides.

4.6.2 Experimental response of optical transitions to strain

A bias voltage deforms the waveguide so the associated strain modifies the orbital structures and the optical transitions of embedded color centers [153–155]. This device geometry enables tuning ranges up to 100 GHz, which is larger than the inhomogeneous distribution and only limited by stiction between the QMC and the substrate (detailed below). For strain tuning experiments, we used a programmable voltage source (Keithley 2400) and observed negligible leakage currents (<0.2 nA) for all applied voltages in this experiment (up to 35 V).

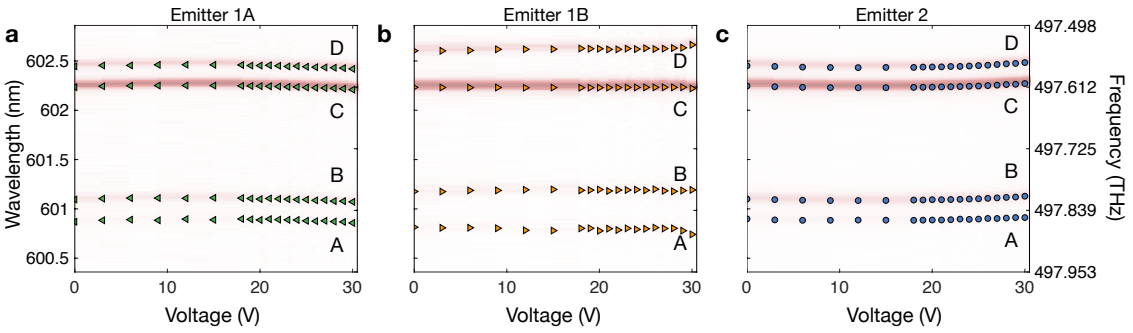

Figure 4-16: Spectral shift of GeV centers in response to strain fields. Strain spectroscopy of (a) Emitter 1A (b) Emitter 1B, and (c) Emitter 2

We consider single GeV centers (Emitter 1A, Emitter 1B, Emitter 2A) indicated in Figure 4-14a, b and Figure 4-15a. Figure 4-16 plots the spectral response of the optical transition lines up to an applied voltage of 30 V. From the increasing line splitting of the orbital ground states Δg, i.e. between lines C & D (as well as A & B), we find that Emitter 1B is a dipole whose axis lies in the transverse plane [25, 153, 154] of the waveguide. Based on their unidirectional shift of all four lines, Emitters 1A and 2 are dipoles oriented in the longitudinal cross-sectional plane of the waveguide [25, 153, 154]. In particular, the global blue-shift of the lines of Emitter 1A indicates that it resides in a region with compressive strain (i.e. below the neutral axis of the mechanical beam). Conversely, the optical lines of Emitter 2 red-shifts with applied voltage, indicating that it resides in a region with tensile strain, which is located above the neutral axis of the waveguide. Table 4.7 summarizes the tuning ranges for the two brightest transitions C and D at 30V. Due to differences in dipole

positions and orientations, we can spectrally overlap the optical transitions of, for example, emitters 1A and 1B in one waveguide at a bias of 24.5 V, as shown in Figure 4-14c. Alternatively, they can also be selectively aligned with that of emitter 2, initially detuned by ∼10 GHz in another waveguide channel, at distinct voltages.

Emitter	$\Delta\nu^{C}_{30V}$ (GHz)	$\Delta\nu^{D}_{30V}$ (GHz)	$\Delta\nu^{C}_{32V}$ (GHz)	$\Delta\nu^{D}_{32V}$ (GHz)
1A	24	24	100	97
1B	11	50	17	50
2	19	25	95	130

Table 4.1: Shift of optical transitions at 30 V and 32 V

Figure 4-17 shows the robustness of the strain-tuning mechanism as we repeatedly applied voltages from 10 V to 26 V. Above 30 V, we see over 100 GHz of tuning of the two brightest transitions C and D for Emitter 1A and Emitter 2; however, we note that in this regime there was hysteresis possibly due to stiction with the underlying gold and substrate about 150 nm and 200 nm away, respectively. Nevertheless, for the purpose here, we were able to spectrally overlap any pair of the three emitters with less than 25 V. Revised electrode, QMC, and/or PIC designs in future microchips should be able to extend the spectral shift of individually tunable waveguides. We note that the small 'pull-in' voltage in our experiment appears earlier than it does in simulation (over 250 V) – possibly due to the surface conductivity of diamond [25, 156].

4.6.3 Stability of optical transitions under strain

We investigated the optical stability of an emitter during spectral tuning via strain. Here, we monitored a GeV in another chiplet with an identical electrode configuration (the earlier device used for Figure 4-14 and Figure 4-15, 4-16, and 4-17 is no longer available due to an accident). Figure 4-18 shows the center frequency shift (bottom)

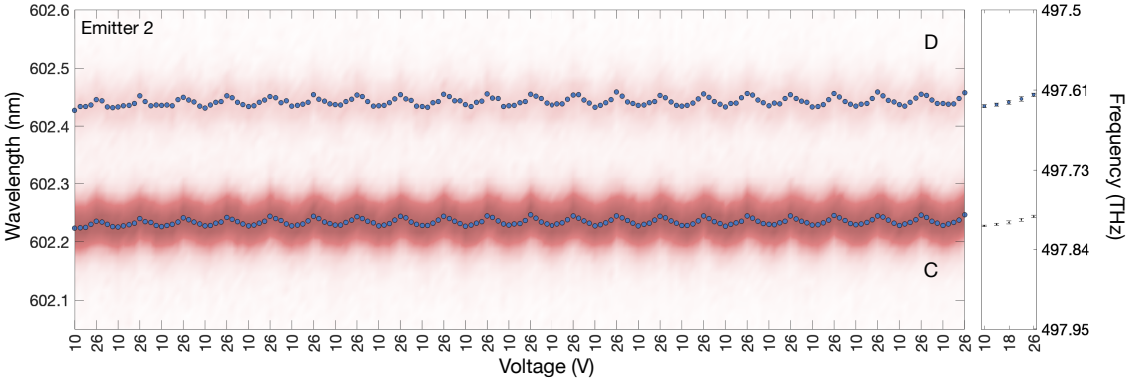

Figure 4-17: Reproducible spectral shifts between 10 V to 26 V.

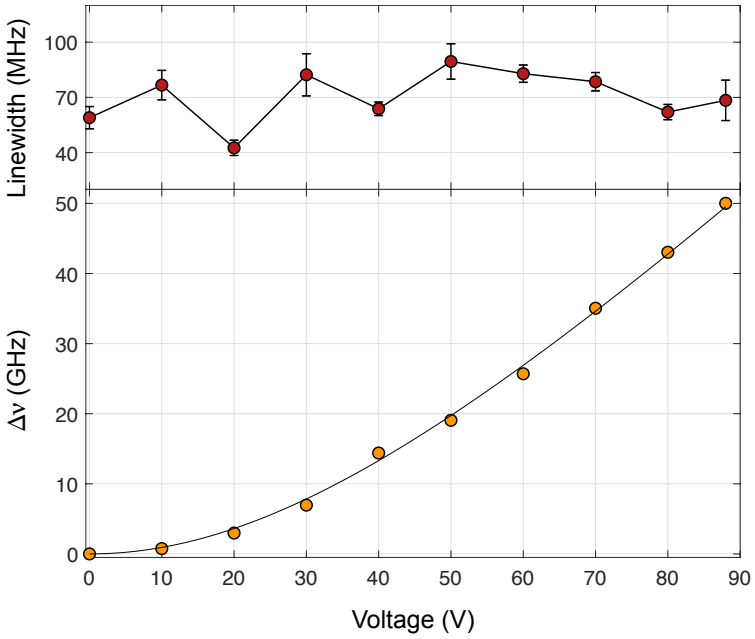

Figure 4-18: Optical properties during strain tuning. Top: PLE linewidths as a function of voltage. Bottom: Corresponding frequency shift, $\Delta\lambda$, of the ZPL transition.

of the ZPL transition and its linewidth (top) as a function of voltage. In these PLE linescans under strain, we averaged each spectrum over 2000 experiments ($\sim$3 minutes) and did not observe significant degradation in the linewidth. We then tracked the ZPL at various voltage biases under repeated PLE measurements over 3 hours of continuous measurement without feedback. Figure 4-19 shows the long-term ZPL stability to within 150 MHz for spectral tuning up to 6.8 GHz. At higher tuning ranges, the linewidths was unchanged but there was an increase in spectral diffusion of the center frequency, likely due to an induced permanent dipole moment

that increased susceptibility to charge fluctuations [25, 157]. Nevertheless, at a tuning of 20 GHz, the FWHM of the inhomogeneous distribution remained under 250 MHz, which is within a factor of 4 of the initial linewidths of ∼60 MHz.

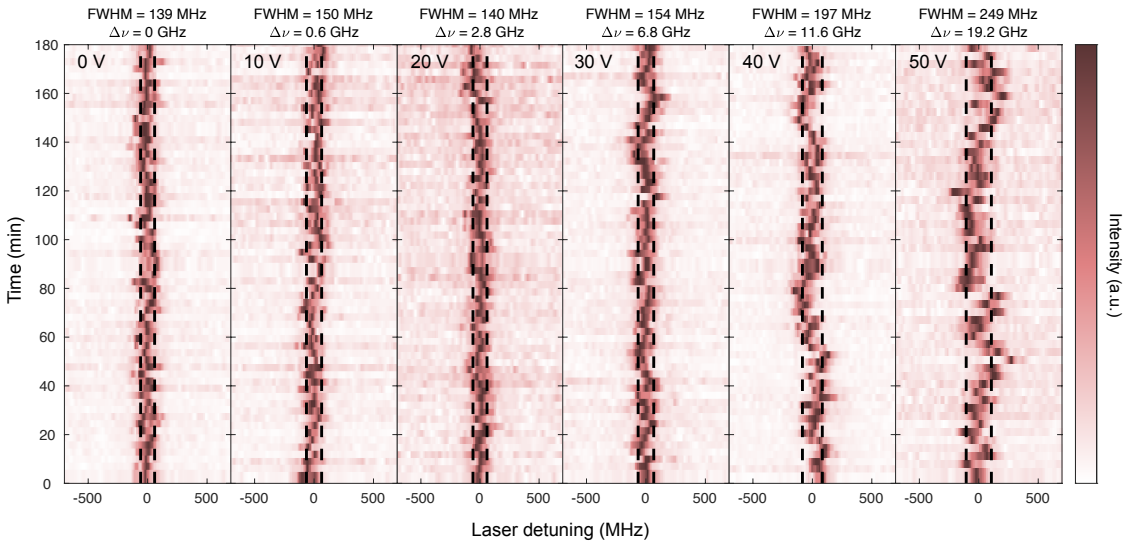

Figure 4-19: Stability of the ZPL transition frequency during strain tuning. Each time slice corresponds to a single PLE linewidth measurement averaged over 3 minutes.

Although not demonstrated here, an array of electrodes could provide closed-loop tuning [155] on each waveguide-coupled emitter to generate indistinguishable photons for Hong-Ou-Mandel interference [158] using on-chip beamsplitters. Based on the emitter linewidths measured here over minutes without feedback, we estimate high-visibility interference of 0.9 (0.8) for stable GeV (SiV) emitters such as those in Channel 41 (69) and a visibility of 0.58 ± 0.24 (0.63 ± 0.07) when averaging over all emitters in Figure 4-13a(b). The optical coherence and photon indistinguishability, which is critical for entangling operations, can be improved, for example, through the Purcell effect by coupling to photonic cavities [159].

4.7 System Efficiency and Improvement Strategies

Figure 4-20a shows the response from an idealized emitter system, fitted to $F = F_{\text{sat}}P/(P_{\text{sat}} + P) + cP$, where P is the continuous-wave 532 nm excitation pump

power, cP is the linear background, $P_{\text{sat}} = 1.2$ mW is the saturation power, and F is the measured ZPL fluorescence at the detector and $F_{\text{sat}} = 1.11$ mega counts per second (Mcps). Table 4.7 shows an average saturated count rate of (0.64 ± 0.36) Mcps from an array of GeV-waveguides in a QMC.

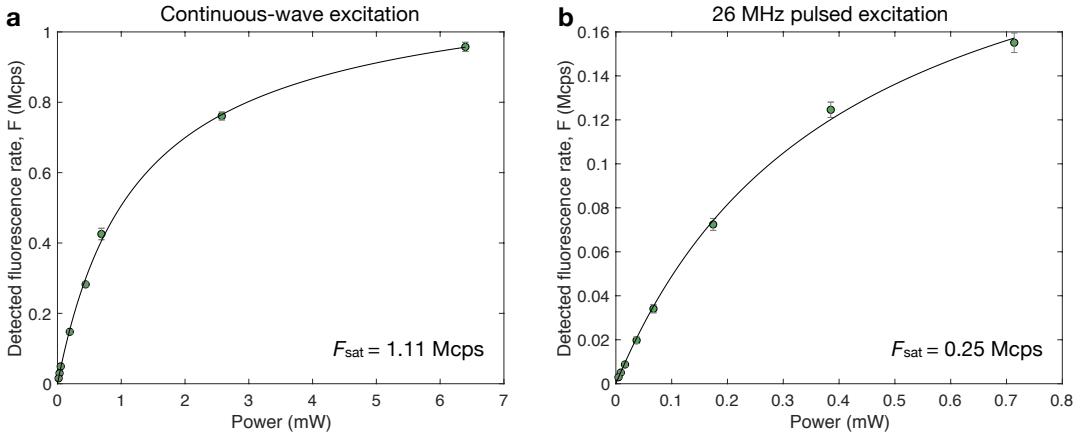

Figure 4-20: Saturation response of a single GeV center. (a) Continuous-wave 532-nm laser excitation (b) Pulsed laser excitation at 532 nm with a repetition rate of 26 MHz.

Counts	41	42	43	44	45	46	47	48
Saturated Counts $\times 10^6$ cps	0.20(3)	0.94(24)	0.21(7)	0.80(9)	0.61(2)	0.91(13)	1.11(23)	0.31(09)

Table 4.2: Saturation count rates from single GeV centers in a QMC

To independently measure the system efficiency at the detector, η, we used a pulsed source (SuperK Extreme, 532 ± 20 nm) with a repetition rate of 26 MHz. From the saturation response (Figure 4-20b), we determined $F_{\text{sat}} = 0.25$ Mcps and $\eta = 0.72\%$. This experimentally determined efficiency is within a factor of 5 from the independently calculated $\eta = 0.5\beta\eta_{\text{PIC}}\eta_{\text{fiber}}\eta_{\text{setup}} \approx 2.6\%$, where ($\beta$, η_{PIC}, η_{fiber}, η_{setup}) $\approx$ (0.55, 0.34, 0.33, 0.58) are the dipole-waveguide, η_{PIC} the diamond-PIC, η_{fiber} the PIC-fiber, and η_{setup} the external setup detection efficiencies. Here, the factor of 0.5 accounts for the present configuration in which we collected the photon emission in

one direction only. In these saturation experiments at room temperature, we used a lensed fiber with 2.5 µm spot size at 1550 nm, which we find to have $\eta_{\mathrm{PIC}} \approx 33\%$. We attribute the discrepancy to the non-unity radiative quantum efficiency of the emitter and deviations in β, η_{PIC}, and η_{fiber} from independent measurements based on another device.

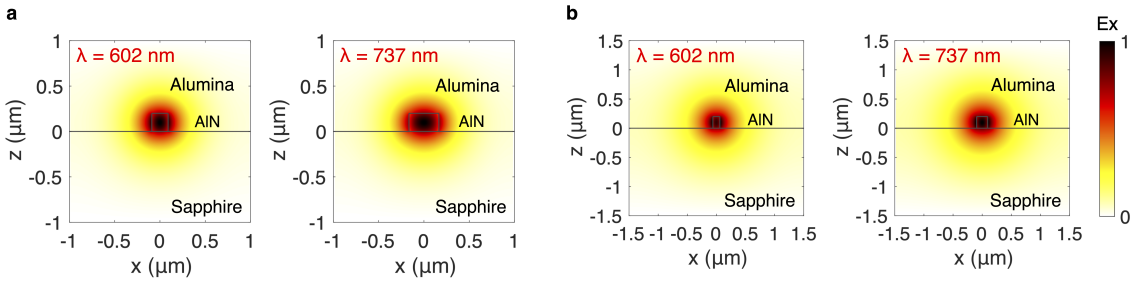

Figure 4-21: FDTD simulation showing the cross sectional E_x field component for an optimized edge coupler for (a) lensed fiber and (b) high NA fiber.

Now, we outline methods to improve the system efficiency. In our experiments, the uncladded microchip enables the heterogeneous integration of QMC but the mode-mismatch between the AlN-on-sapphire waveguide and the lensed (high NA) fiber causes at least 3 db (5 dB) insertion losses as characterized above. It is possible to improve the mode overlap by cladding the microchip with alumina or with materials with similar refractive indices as the underlying sapphire [44]. In such a scheme, we would taper down the AlN waveguides at the chip facet to better mode-match with the lensed fiber. Our cladded edge coupler design can significantly improve the coupling from the AlN waveguide to the lensed fiber to be 84% (84%) at 602 nm (737 nm), as well as improve the coupling to high NA fiber to be 89% (91%) at 602 nm (737 nm), using the present AlN-on-sapphire material and film thickness. In this design, we matched the mode field diameters and reduced the effective refractive index mismatch between the fundamental TE modes at AlN edge coupler facet and the lensed (high NA) fiber focus spot (facet). Figure 4-21 shows the E_x field component for the optimized edge couplers. Due to the index mismatch, the light coupling is limited by Fresnel reflections at the waveguide facet, which can be reduced using an index-matching environment. Finally, on-chip reflectors in diamond can increase the

photon collection efficiency by a factor of 2, and photonic crystal cavities can boost the emission into the waveguide mode.

4.8 Conclusions and Outlook

The large-scale integration of artificial atoms with photonics extends to a wide range of nanophotonic devices, in particular high-quality factor diamond photonic crystal cavities [143, 144, 160], and other optically active spins [6] such as NV centers [35], emerging diamond Group-IV quantum memories [161], quantum dots [162], and rare-earth ion dopants [39, 40]. The advances reported in this work should therefore encourage further integration of photonic and electronic components for large-scale QIP applications such as multiplexed quantum repeaters or modular quantum computers based on solid-state spins [11–14, 47, 149, 163, 164]. Key components have already been individually demonstrated, including photonic switch arrays and beamsplitter meshes [165–168] for reconfigurable qubit connectivity and heralded spin entanglement, AlN-based high-speed electro-optic modulators [52] and SNSPDs [130, 137], and custom CMOS electronics [169, 170] for color center spin control and low-latency processing. As PIC applications ranging from optical communications [171] to phased array lidar [172] to machine learning accelerators [165] are pushing systems beyond thousands of optical components, the high-yield integration with arrays of high-quality artificial atoms sets the stage to extend these scaling gains to quantum information processing with spins and photons.

Chapter 5

Integration of Single Photon Sources in 2D Materials and Detectors on AlN

This chapter will highlight my co-author works, led by my collaborators, that are relevant to the overall theme of my thesis. In particular, I will be showing the building blocks and other devices integrated onto AlN photonics that can be leveraged for quantum information processing.

5.1 Integration of Quantum Emitters in Layered Materials to AlN Photonic Circuits

5.1.1 Background and Introduction

Experimental implementations of hardware for quantum networks and quantum information processors require multiple single photons on a chip. So far, efforts have mainly been in 3D solid-state systems like shown previously in this thesis, where the single photon sources are embedded in the bulk 3D material, and nanophotonic structures are then fabricated into the semiconductor material. Recently, 2D materials are also gaining traction as hosts to high quality, ultrabright single photon emitters

(SPEs). 2D materials can in principle be transferred onto any photonic structures by exfoliation and stamping. Quantum emitters in 2D materials show remarkable photostability and emission efficiency despite their close proximity to surfaces, which allows for atomically-precise control of the atomic defects or even potentially the ability to control the spectral, charge, and spin properties of the atomic defect through heterostructure stacking of layered materials.

Quantum emission from hexagonal boron nitride (hBN) 2D monolayers and 3D multilayers have previously been shown to be ultrabright, polarized, and operational at room temperature [113]. It has further been gaining traction as a promising single photon emitter as researchers have demonstrated the ability to tune the emission of these defects [134] in order to control its inhomogeneous spectral distribution and to show that the emitters are stable after transfer to other substrates. Two-dimensional van der Waals materials have shown great promise as a heterogeneous assembly candidate for solid-state quantum technologies [173–175], but these previous demonstrations were limited to cryogenic temperature operations. Here, I will show the transfer and integration of hBN multilayers to AlN photonics to demonstrate the first photonic integration of room-temperature 2D material quantum emission sources. This work was led by our collaborators in Professor Igor Aharonovich's group at the University of Technology Sydney [116].

5.1.2 Results

Figure 5-1 shows the schematic and experimental device of the hBN flake with embedded single photon emitter transferred on top of an AlN ridge waveguide that is terminated with a grating coupler for output collection and detection. AlN has a refractive index ($n = 2.08$) close to that of hBN ($n = 2.1$), which minimizes the index mismatch and thus reflection at the AlN/hBN interface. As shown by the AFM cross-section measurement in Figure 5-1c, the hBN flake has a total height of ∼200 nm.

Figure 5-2a shows the confocal PL scan of the sample, measured with a CW green optical excitation laser (532 nm) through a 0.9 NA objective. For the confocal scan,

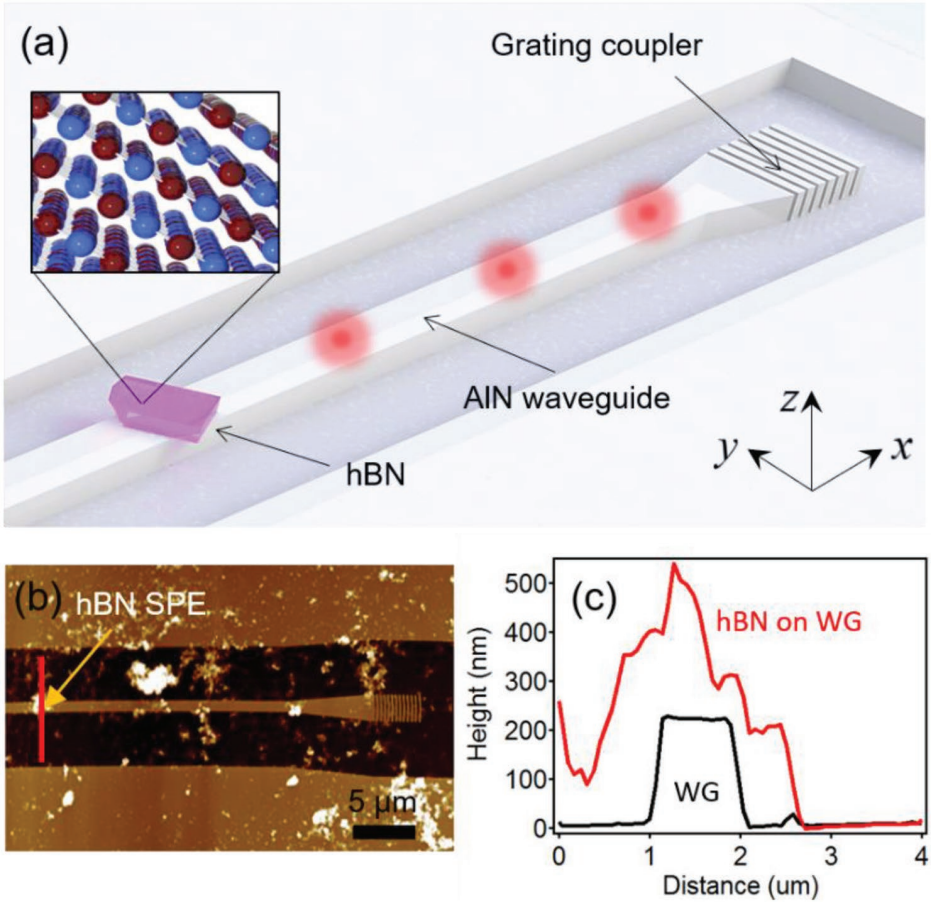

Figure 5-1: Coupling of the hBN emitter to the AlN waveguide. (a) Schematic view of the hybrid quantum photonic system showing a hBN flake (purple) positioned onto an AlN ridge waveguide (light gray). The inset shows the layered van der Waals hBN crystal. (b) Atomic force microscopy (AFM) image of the hBN-waveguide structure. The position of the hBN emitter onto the waveguide is indicated (yellow arrow). (c) AFM height measurement of the hBN emitter on the waveguide along the cross-section profile following the red line in (b); the ridge measured for the pristine waveguide is also shown (black trace).

the excitation and collection are from the same spot, while the sample is scanned using a piezo stage. The location of the SPE on the waveguide is identified and subsequently characterized. Figure 5-2b shows the zero-phonon line (ZPL) of the hBN SPE at 623 nm with a linewidth of 4.24 nm (full width at half maximum of the fitted Lorentzian). The spectrum was integrated for 60 seconds at an excitation power of 2 mW. The spectrum and second-order autocorrelation $g^{(2)}(\tau)$ measurements in Figure 5-2b were filtered using a bandpass filter (Semrock, (630 $\pm$ 28) nm) to spectrally reject the

chromium luminescence peak from sapphire and to isolate the emitter's ZPL (the regions shaded in gray in Figure 5-2b,d display the spectral regions that were filtered out). The insets in Figure 5-2b,d show the second-order autocorrelation measurement $g^{(2)}(\tau)$ performed using a Hanbury-Brown and Twiss interferometer and corrected for background and time jitter. A zero-delay time value of $g^{(2)}(0) = 0.12$ for the second-order autocorrelation measurement in Figure 5-2b, indicates the single-photon nature of the emitter.

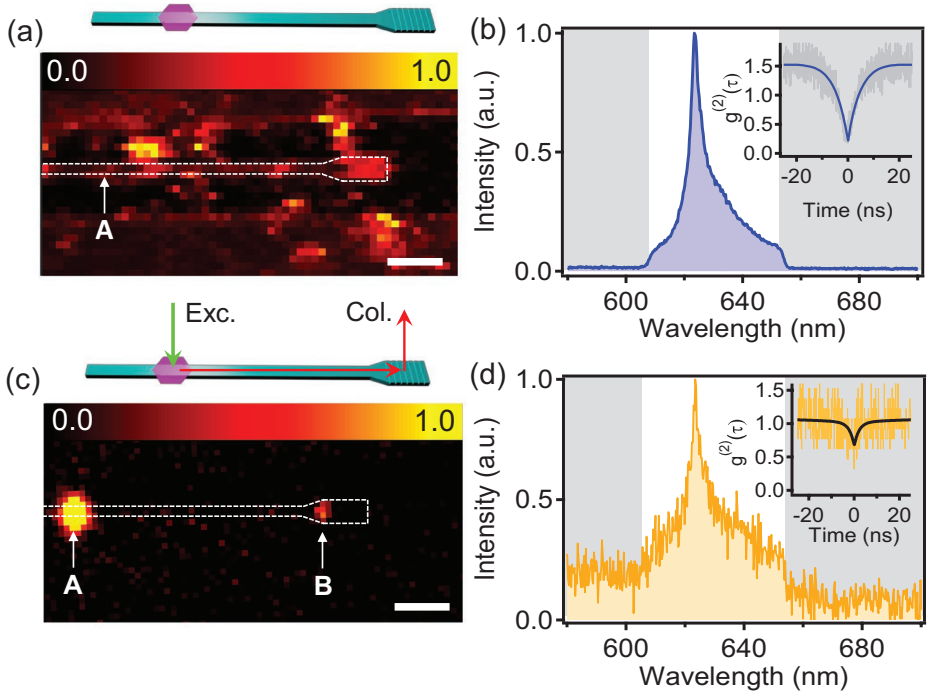

Figure 5-2: Optical characterization of the hBN-waveguide heterogeneously integrated structure. (a) Confocal map of the hybrid system under 532 nm CW laser excitation. The emitter at point A is dimmer compared to the overall intensity within the map, and therefore is not clearly visible in the map. (b) PL spectrum of the hBN emitter and its second-order autocorrelation $g^{(2)}(\tau)$ curve (inset) indicating single-photon emission ($g^{(2)}(0) < 0.5$). (c) Confocal map where the 532 nm laser excitation is fixed on the emitter (spot A) and the collection is scanned over the sample. In the collection scan, the 532 nm laser is filtered out. The map shows that photons from the emitter couple to the waveguide and are detected at the grating coupler (spot B). (d) PL spectrum and $g^{(2)}(\tau)$ curves (inset) are collected from the grating coupler (spot B) with excitation fixed at the emitter (spot A). Scale bars are 5 μm in both (a),(c). The collection spectral window is indicated by the unshaded areas in (b),(d). The $g^{(2)}(\tau)$ curves are corrected for background and time jitter.

Figure 5-2c shows a different measurement scheme in which the excitation laser (532 nm) is kept fixed at the location of the hBN SPE (spot A), while collection is acquired over a 30×30 μm^2 area using a scanning mirror with the 532 nm excitation laser filtered out. The resulting confocal scan reveals luminescence from the emitter both locally at spot A and at a lower intensity from the output grating at spot B. This demonstrates successful coupling and propagation of single photons from the hBN emitter, through the AlN waveguide, and output by the grating coupler. The bright emission from the spot B in Figure 5-2c is further analyzed with a spectrometer, revealing the same ZPL (623 nm) as from a spot A, as shown in Figure 5-2d. The intensity of the PL signal measured at the grating coupler (spot B) is 1.2% of the total PL intensity collected from spot A. The inset in Figure 5-2d shows the resulting autocorrelation function, which has a significantly higher $g^{(2)}(0)$ value. This is most likely due to the increased background compared to that the measurement configuration in Figure 5-2a,b. The $g^{(2)}(\tau)$ measurement was taken by changing the linear polarization of the excitation laser on spot A while optimizing for the count rate of the fluorescence at spot B. Instead, for future works, the background could be minimized by changing the polarization to minimize the amount of green excitation laser coupling to the waveguide.

5.2 Superconducting Nanowire Single-Photon Detector on AlN

5.2.1 Background and Introduction

High performance single-photon detectors are necessary for a complete integrated quantum photonics platform. The ability to efficiently detect single photons from the quantum emitters is critical for maximizing the rate of remote spin entanglement by heralded photon detection, for example. We can achieve this by having everything on a single chip to reduce significant loss factors from coupling to off-chip detectors. The superconducting nanowire single-photon detector (SNSPD) is the leading single-

photon detection technology for quantum information processing. They outperform other single-photon detection devices in many metrics, which typically include detection efficiency, count rate, dark-count rate, and jitter. Though shown in separate independent demonstrations, SNSPDs have been shown to have near-unity detection efficiency, GHz count rate, sub-1-cps dark count, and sub-20-ps timing jitter [176–179].

SNSPDs can be used to detect photons that are routed by nanophotonic waveguides. Waveguide-integrated SNSPDs absorb light evanescently, with their optical absorption increasing exponentially with the length of the nanowire. Hence, a high optical absorption can be achieved with a short nanowire by maximizing the mode overlap, which could also result in faster detection speed, reduced dark counts, lower timing jitter, and higher yield compared to a typical detector that is coupled to fiber, which requires a much larger detection area. Having these detectors on-chip would greatly improve the emitter-to-detector efficiency [180, 181], thus facilitating photon-mediated entanglement from distinct nodes.

One of the most well-studied high-performance SNSPDs are fabricated using polycrystalline niobium nitride (NbN), which has a relatively high critical temperature (T_c) of 8-12 K in the 4-6 nm thick thin-film typically used for SNSPD fabrication. Furthermore, the film quality of polycrystalline NbN is better if grown on a lattice-matched crystalline substrate. As our photonic platform is AlN-on-sapphire, the lattices of NbN and AlN are well-matched and should result in good film qualities. SNSPDs also operate at cryogenic temperatures compatible to the typical operating temperatures for color centers in diamond, which is another reason why it is advantageous for integrating to our quantum photonic system and operating everything together on one chip in a cryostat. Furthermore, NbN SNSPDs have broad spectrum response, operating into the visible spectrum which most promising solid state quantum emitters emit at [177]. Here, I will also show the development of NbN SNSPSDs grown on top AlN-on-sapphire substrates and introduce briefly on the efforts we had in integrating these SNSPDs to AlN waveguides. This work was led by our collaborators in Professor Karl Berggrens's group at MIT [130, 137]).

5.2.2 Results - SNSPDs on Bulk AlN

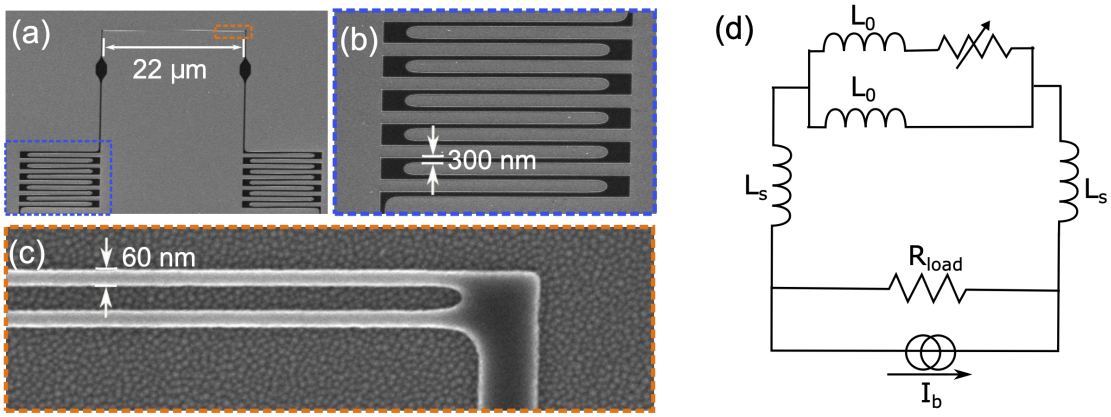

Figure 5-3: Device configuration. (a)-(c) SEM of the fabricated device. The detector consisted of two components: the active region and two serial inductors. The active region consisted of two parallel nanowires with 60 nm width, 80 nm gap, and 22 μm length (c), corresponding to the top two parallel inductors L_0 in the equivalent circuit in (d). The serial inductors were made of 300-nm-wide meander nanowires (b), corresponding to L_s in the circuit. The single strip configuration was designed for waveguide integration.

The NbN thin films are deposited on the AlN-on-sapphire substrate by reactive DC magnetron sputtering, with the substrate holder set to 840°C, using the recipe developed previously [178]. The resulting film has a critical temperature T_c of 10.6-11.4 K, sheet resistance R_S of 500-550 Ω/sq, residual resistance ratio (R_{300K}/R_{20K}) of 0.82-0.86, and thickness of ∼4.8 nm. We use a 2-element superconducting nanowire avalanche photodetector (2-SNAP design with 60 nm width) to achieve high quantum efficiency, high signal-to-noise ratio, and low timing jitter. First, we pattern the electrical contact pads and alignment markers using photolithography followed by metal liftoff (25 nm Au on top of 5 nm Ti). We use a bi-layer photoresist process of S1813 on top of PMGI-SF9, where the PMGI is an undercut layer that helps facilitate metal liftoff. Then, the superconducting nanowires are patterned using electron-beam lithography (Elionix ELS-F125) with a negative-tone resist (hydrogen silsesquioxane, HSQ), followed by development using 25% TMAH. HSQ pattern is then transferred to the NbN film using CF_4 reactive-ion etching. Figure 5-3a shows an overview of the scanning-electron micrograph (SEM) of the fabricated 2-SNAP, with the equivalent

circuit diagram shown in Figure 5-3d. The active area is made of two parallel 60 nm wide, 22 μm long nanowires designed for waveguide integration (Figure 5-3c). This 22 μm long detector can absorb 95% of 637 nm wavelength light propagating in a 450 nm × 200 nm AlN-on-sapphire waveguide. Figure 5-3b shows 300 nm wide meandering wires that function as serial inductors to prevent the detector from latching.

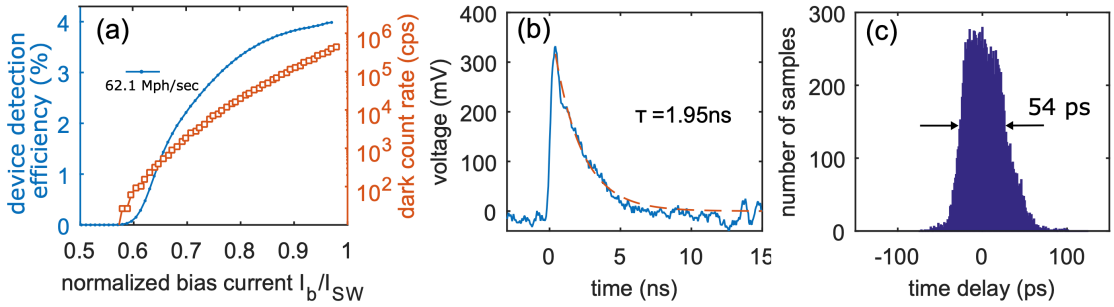

Figure 5-4: Device performance. (a) The saturation in DE is a signature of high internal quantum efficiency. The absolute value in DE was limited by the unpolished back surface of the chip. (b) A single-shot pulse trace of the same detector. (c) The instrument response function revealed a jitter of 54 ps.

We measured the device detection efficiency and dark count rate vs. bias current in a 2.45 K cryogenic probe station with 1550 nm wavelength back illumination by an optical fiber, with the results shown in Figure 5-4a. The detection efficiency entered the saturation region as the bias current approached the switching current of $I_{SW} = 23.5$ μA. However, this detection efficiency is not important since waveguide-integrated detectors would have a significantly higher absorption. We then measured the single-shot trace of the electrical pulse generated from the same detector biased at $0.95I_{SW}$, as shown in Figure 5-4b. The measured falling edge time constant is 1.95 ns, corresponding to a ∼6 ns reset time. Finally, we found the jitter to be 54 ps (Figure 5-4c) when the detector is biased at $0.95I_{SW}$.

5.2.3 Results - A Scalable Multi-Photon Coincidence Detector

Using the same fabrication process for making NbN SNSPDs on AlN-on-sapphire, we also demonstrated a two-terminal coincidence detector that enables scalable read-

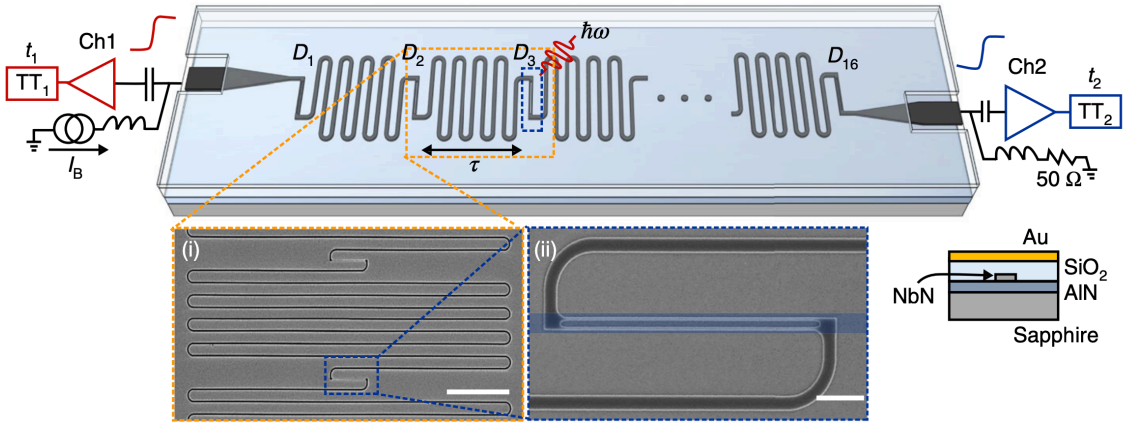

Figure 5-5: Device layout for a sixteen-element detector. The detector is a two-terminal array that connects a chain of single-photon detector segments using slow-wave nanowire delay lines. The nanowire was designed to be a microstrip waveguide with a dielectric spacer and a top ground plane. (i) SEM of the delay line, which consisted of a 300 nm wide meandered nanowire. Scale bar, 10 μm. (ii) SEM of a detector segment, which consisted of two 80 nm wide parallel nanowires. Scale bar = 1 μm. The blue band marks the site for future waveguide integration.

out of an array of detector segments using a superconducting nanowire microstrip transmission line, as shown in Figure 5-5 [130]. The detector connects a chain of single-photon detector segments using slow-wave nanowire delay lines. This sixteen-element detector was shown to resolve all 136 possible single-photon and two-photon coincidence events by taking advantage of timing logic. We also demonstrated photon-number-resolving capability by looking at the pulse shapes of the detector output. Figure 5-5(ii) shows the location of where waveguides would be pattern for waveguide integration of these detectors.

5.2.4 Results - Towards Integration of SNSPDs on AlN Waveguides

Finally, we developed a process for fabricating NbN SNSPDs integrated with AlN-on-sapphire nanophotonic waveguides. The process begins with deposition of NbN thin films on the AlN-on-sapphire substrate by the same method as mentioned previously [178]. Then, we patterned the electrical contact pads and alignment markers using the same bi-layer photoresist process of S1813 on top of PMGI-SF9. The first difference

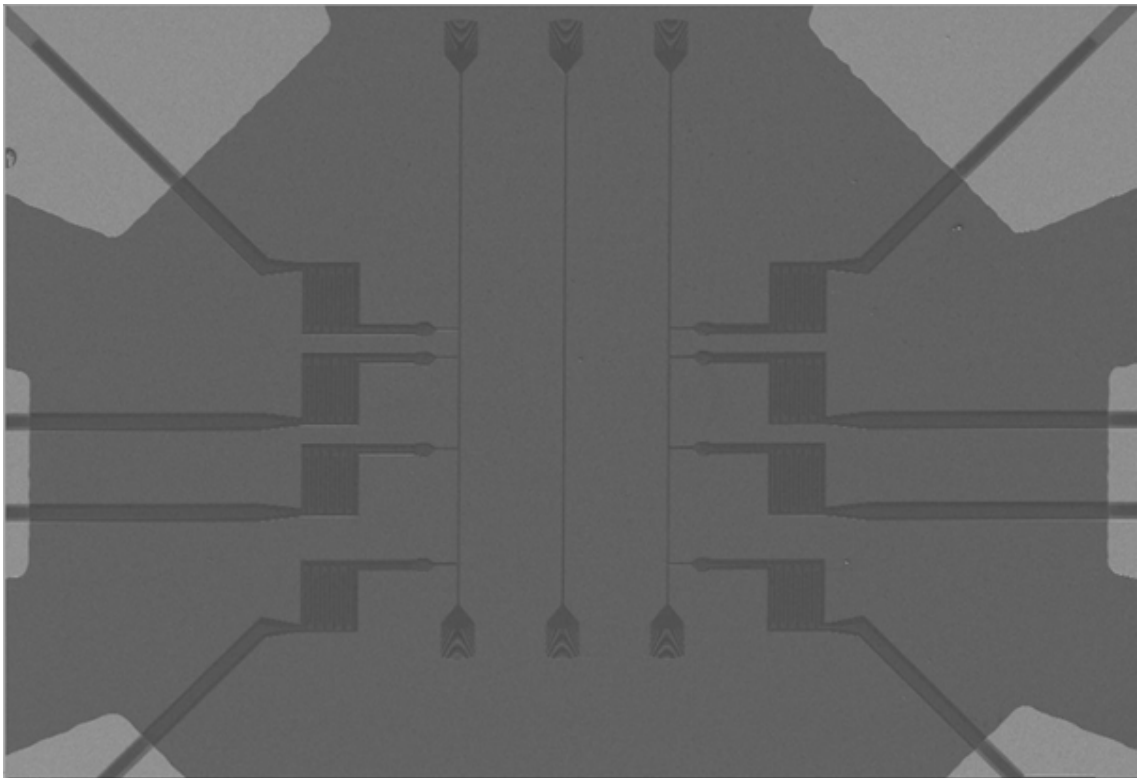

Figure 5-6: SEM image of the electron beam lithography patterning of the AlN waveguide with respect to the fabricated NbN SNSPD detector, showing the alignment between them

is that now the metal stack is composed of 50 nm SiO_2 on top of 5 nm Ti on top of 50 nm Au on top of 5 nm Ti. The top SiO_2 layer is to act as a protection for the NbN during the subsequent AlN etch, with the top-most Ti layer acting as an adhesion layer due to SiO_2's poor adhesion properties. Then, the NbN nanowires are patterned by electron-beam lithography using HSQ resist, followed by CF_4 reactive-ion etching, same as described before. Now that the majority of the NbN top surface is etched away, exposing the AlN, with only the intended NbN nanowires left, we proceed with the AlN waveguide fabrication. Following oxygen plasma treatment, we spincoat 2% XR-1541 HSQ, followed by Espacer conductive polymer. Using the Elionix ELS-F125 once again with dose of 10,000 $\mu C/cm^2$, the waveguides and grating couplers are patterned with 1 nA beam current while we also pattern a capping layer over the superconducting inductors and leads with 5 nA beam current to protect them during subsequent AlN etch. The HSQ was then developed in salty developer (1 wt%

NaOH and 4 wt% NaCl). Figure 5-6 shows an SEM image of the resulting sample up to this step, with the detector region well-aligned to the AlN waveguides. Finally, the chip is etched using the chlorine chemistry reported in Chapter 2 of this thesis [44], resulting in the final device shown in Figure 5-7. Systematic measurements of SNSPDs fabricated on AlN photonic integrated circuits will need to be completed in future works, with the on-chip detection efficiency of the integrated detectors being the key metric.

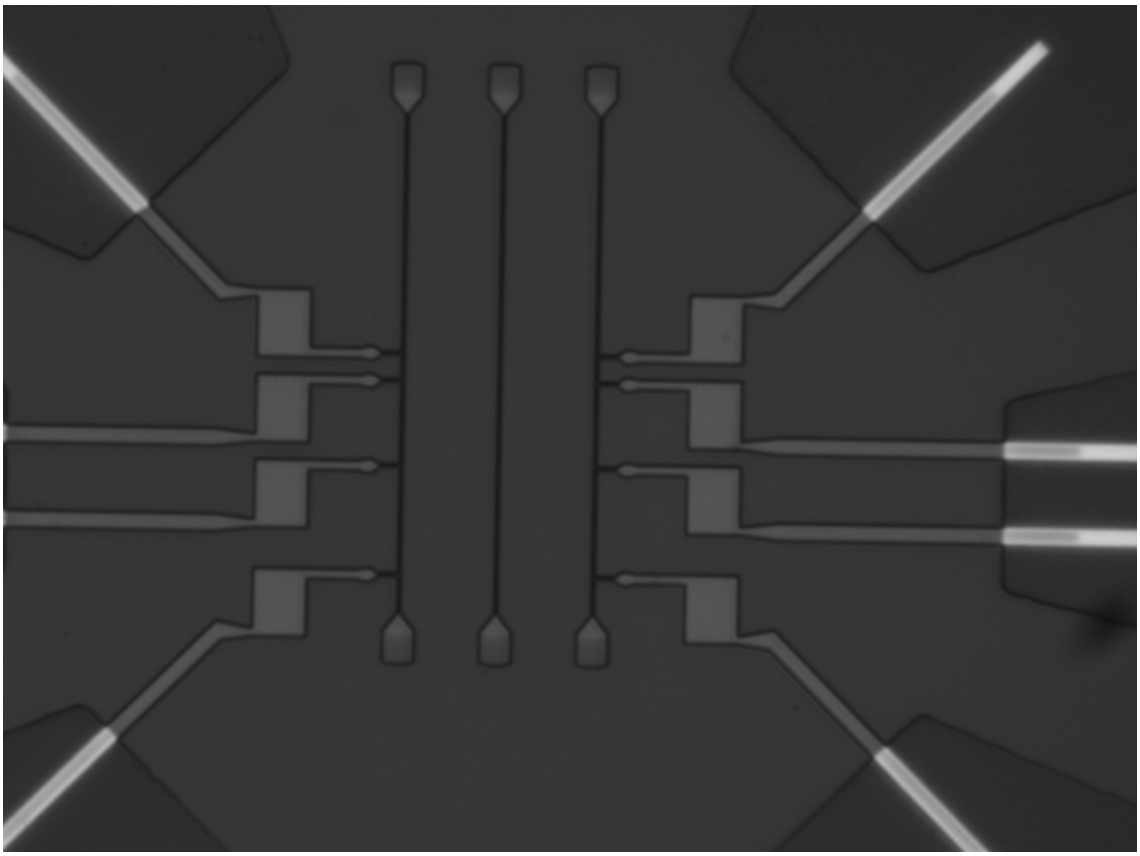

Figure 5-7: Optical microscope image of the complete fabrication of NbN SNSPD detectors integrated with AlN waveguides.

Chapter 6

Conclusion and Outlook

In this thesis, we developed a wide-bandgap integrated photonics platform based on AlN-on-sapphire with transparency and low-loss optical propagation from the UV to the infrared wavelength regime. Then, we demonstrated the versatility of this integrated photonics platform for interfacing with various quantum devices operating in a wide range of wavelengths, thus showing its potential to serve as a photonic multi-chip module backbone for realizing scalable quantum technologies. Solid-state quantum technologies have long been touted for its scalability promise, but proof-of-concept experiments to-date have been limited to just a handful of qubits per chip due to device inhomogeneities, low device yield, and complex device requirements. We show the first-ever proof-of-concept demonstration of large-scale integration of quantum emitters to our photonics platform that can potentially leverage the production capabilities of the III-nitride industry, akin to the widely-used silicon photonics of today that take advantage of CMOS foundry manufacturing. Here, we will discuss about outlook and future directions of each work in this thesis

6.1 AlN-on-Sapphire Integrated Photonics

In Chapter 2, we developed a novel integrated photonics platform based on AlN-on-sapphire. We showed that with the significantly better crystallinity in the material by growing on top of single crystal Al_2O_3 (sapphire) instead of what was used in

previous works where AlN was grown on amorphous SiO_2, we can reduce loss from Rayleigh scattering due to surface roughness and material loss caused by unwanted defect absorption that is prevalent in samples of low crystalline quality, allowing us to show UV propagation loss at 369.5 nm that is several tens of orders of magnitude lower than the propagation loss previously shown at 400 nm using an AlN on SiO_2 platform [78]. However, there is still lots of room for improvements as the nanocrystalline film morphology of our wafers in this work was not the best possible. Single crystalline AlN can be grown on sapphire and would certainly exhibit significantly better film quality. Furthermore, as mentioned previously, Rayleigh scattering ($\propto \lambda^{-4}$) can be dramatically reduced by photonic engineering to design the waveguide dimensions such that the optical mode overlaps minimally with the sidewalls in order to minimize light scattering from the waveguide faces.

Being the first to show that material film quality of AlN would have a large effect on light propagation in the UV to visible wavelength regime, this work led to follow-up works from other groups. For example, there was a paper afterwards showing microring quality factors of 2.1×10^5 at 390 nm (corresponding to an optical loss of $\sim$8 dB/cm) with a 500 nm thick single-crystalline AlN grown on c-plane sapphire by metal-organic chemical vapor deposition (MOCVD), with the large waveguide dimensions resulting in small mode overlap with the sidewalls [136]. With extremely low propagation loss being a requirement for quantum photonics, further AlN-on-sapphire integrated photonics research is necessary to obtain better crystallinity in the AlN film, to achieve improved fabrication techniques to minimize side-wall roughness, and to understand the material properties to gain insights for material treatments to eliminate unwanted absorptive defects. We hope that the culmination of these developments would result in waveguide propagation losses in AlN approaching the levels of sub-dB/cm that Si-on-SiO_2 has (though that is in telecom wavelength where Rayleigh scattering is much less of an issue).

6.2 Quantum Emitters in AlN Integrated Photonics

In Chapter 3, we also report on a novel high-purity, ultra-bright quantum emitter in thin film AlN grown on top of sapphire, along with waveguide integration. However, there is a lot more to be done to further warrant its use for quantum information processing applications. A key experiment would be to perform an on-chip second-order autocorrelation measurement in which the capability would be a building block for other linear-optic processing, as well as two-photon interference. To fully take advantage of the readily-integrable aspect would be to show on-chip filtering of pump light, integration with a cavity for Purcell enhancement, and maximizing the collection efficiency to the point of beating the efficiency of the high-efficiency setup we used to do the emitter spectroscopy and characterization experiments. For on-chip filtering of pump light, we can use distributed Bragg reflectors, a ring resonator in a drop port configuration, or a directional coupler that sends the majority of green light into one port and the majority of the single photon signal into another port. There needs to be a significant 50-60 dB isolation or more in order to collect pure single photon signals without additional off-chip filtering. The further development of the passive and active photonic components in the AlN-on-sapphire platform would allow for more functionalities for both the quantum emitters created monolithically and the quantum emitters integrated heterogeneously (diamond, 2D materials, III-V semiconductors, etc.).

In addition, there are also lots of studies needed to understand the optical and spin properties of the emitter. Photoluminescence excitation measurement of the emitter would be important to study the optical coherence of the emitter. Coherent excitation allows accurate measurement of the emission linewidths and photophysical properties of the emitters. It is also necessary for generation of indistinguishable photons, entanglement, and coherent control of the emitter's quantum states. A narrow linewidth from resonant excitation could give insight on the ZPL broadening mechanism when pumped with an off-resonant laser (the typical measured lifetime of

the emitter in AlN is ∼3 ns, which corresponds to a FT-limited linewidth of about 55 MHz). We would need to experimentally observe and verify the theoretically predicted spin properties, along with investigating the exact origin of the emitter. Doing so would allow us to better understand the electron spin levels of the emitter. Furthermore, currently, there is a broad inhomogeneous distribution of the emitter zero-phonon line wavelength, which is also characteristic of quantum emitters in other III-N materials [113, 114]. For quantum entanglement applications, the wavelengths will need to be indistinguishable, so an inhomogeneous distribution of over 40 nm could be too large of a variation to be useful for quantum entanglement. There will either need to be a mechanism to tune the zero-phonon line of two emitters to be on-resonance with each other or to reduce the inhomogeneous distribution.

6.3 Large-Scale Integration of Quantum Memories in Diamond to AlN Photonic Circuits

In Chapter 4, we presented a method to scalably produce connected arrays of diamond waveguides with each channel containing high quality quantum emitters with nearly-indistinguishable emission. Utilizing our 'quantum microchiplet' and 'multi-chip module' framework, we achieved the largest number of photonic channels integrated with solid-state quantum memories fabricated on a single chip, while maintaining near-transform-limited linewidths for all the emitters. As nitrogen vacancy centers in diamond were used in previous demonstrations working towards a distributed quantum network, the frequency of their zero phonon emission can be controlled by Stark tuning [182, 183]. However, this is not possible with the GeVs and SiVs we used in this work due to their inversion symmetry. Instead, the GeV and SiV's electronic structures are affected by strain within the diamond crystal lattice, meaning that we can strain the diamond waveguides through deformation to change the wavelength of the zero phonon emission [153–155]. As such, we also developed nanoelectromechanical system (NEMS) designs that use electrostatic forces acting on the diamond

waveguides to tune the GeVs, while maintaining compatibility with our quantum microchiplet framework. We showed experimentally that these devices can be designed to tune two GeVs to the same wavelength. Future works would need to extend the strain tuning aspect to SiV, as well as to demonstrate on-chip two-photon interference and even entanglement between two spatially separated GeV or SiV centers.

For future work beyond this thesis, we envision the AlN backbone to have sufficiently fast photonic switches in a mesh configuration for multiplexed entanglement, as well as integration of additional technologies that have been demonstrated separately, such as the on-chip detectors presented in this thesis [130, 137, 184], and CMOS electrical control, which will enhance the overall scalability and functionality of this platform. The inclusion of CMOS electronics in our modular architecture would also provide a path towards large-scale chip-integrated quantum control [169, 170]. Another potential goal for future works is to work towards an all-fiber photonic packaging of these large-scale heterogeneously integrated systems in order to operate the system in dilution refrigerators to reach temperatures low enough to suppress phonon-induced decoherence [23, 138]. These advances, taken together with the deterministic assembly of large-scale artificial atoms with AlN PICs containing phase-stable interferometers [44, 185] and modulators [52, 186, 187], set the stage for high-rate photon-mediated entanglement generation that underpins applications from multiplexed quantum repeaters [163, 164] to modular quantum computing [13, 14, 47].

6.4 Integration of Single Photon Emitters in hBN to AlN Waveguides

Then, in Chapter 5, we also demonstrated integration of room-temperature SPEs in a 2D van der Waals crystal, specifically hBN, to an AlN waveguide. This hybrid system constitutes the first step towards room-temperature, multifunctional photonic circuitry based on 2D material quantum light sources. Further optimization can be achieved by improving the coupling efficiency. Better nanophotonic components can

be designed by inverse-design principles [188] and fabricated for more efficient and functional on-chip photonic operations. Using monolayers of hBN would also dramatically improve the coupling efficiency to the AlN waveguide due to the increased overlap of the AlN waveguide mode to the emitter. Research into strain engineered quantum emitters may enable engineering the spectral characteristics of the emitter on-demand for indistinguishability while being in a precise location on the waveguide [189–191]. New developments of SPEs in hBN grown by chemical vapor deposition (CVD) have been shown to have an unimodal distribution of quantum emission at (580 ± 10) nm with 2 per μm^2 spatial densities that allow both spatial and spectral overlap with a cavity fabricated in a heterogeneous material [192], further showing the promise of forming ultra-bright, room-temperature, indistinguishable single photon sources using hBN.

6.5 Towards Integration of SNSPDs on AlN Waveguides

Finally, we showed the development towards AlN waveguide-integrated SNSPDs to our quantum photonics system. The high quantum efficiency and low timing jitter demonstrated with NbN SNSPDs grown on top of AlN would enable accurate on-chip photon correlation measurements. As we show a process for co-fabrication of NbN and AlN on a single chip, we can also use NbN as superconducting electronics for fast optical modulation of the AlN waveguides using the AlN's electro-optic properties, low-loss transmission lines and antennas to deliver microwave signals for the integrated quantum memories, and acoustic control of quantum emitters using AlN's piezoelectric properties. The 16-element detector architecture and operating scheme would be useful for multi-photon coincidence detection in large-scale photonic integrated circuits, fitting the theme of this thesis of scalably manufacturing all the necessary components for a large quantum photonic system. Furthermore, AlN's piezoelectricity can potentially be used to frequency transduce between the microwave

domain and optical domain to interface photonic waveguides with superconducting qubits that can be fabricated out of NbN. This would be done by coupling the vibrational mode of an AlN opto-mechanical resonator that uses AlN's piezo-electric properties with a superconducting circuit to transduce microwave photons to optical photons. This would allow the two leading solid-state quantum information processing technologies to combine where the superconducting qubits are excellent for local quantum gate operations and quantum computation while atomic defect center qubits are excellent quantum memories to form a quantum network or for tasks requiring synchronization and quantum state storage.

6.6 Scalable Foundry Level Production of AlN Integrated Photonics

The long-term goal for our wide-bandgap photonics platform based on AlN is to extend it into foundry production so that we can go beyond just individual device development and focus on making large systems. Silicon and SiN integrated photonics have seen tremendous growth in a short amount of time due to those materials already being available in commercial foundry processes. Fortunately (and part of the reason for our selection of the material), AlN already exists in commercial CMOS fabrication as an insulator for high voltage electronics. However, the material and material patterning process do not result in the optical qualities necessary for low-loss integrated photonics, mainly due to the fact that the AlN is deposited on SiO_2, which results in an amorphous or polycrystalline material that would have significant scattering loss from grain boundaries and absorption from defects in the UV regime. Something similar to Smart-Cut® technology or growth of single-crystal AlN on two dimensional materials on top of a substrate with low lattice mismatch with the AlN that can then subsequently be transferred to any substrate [193] would be crucial to make commercial-level production of this material in CMOS foundries possible. Hopefully more wide-spread use of AlN for quantum technologies would inspire

further developments towards this.

Bibliography

[1] S. Wehner, D. Elkouss, and R. Hanson, "Quantum internet: A vision for the road ahead," *Science*, vol. 362, p. 303, 2018.

[2] M. Atatüre, D. Englund, N. Vamivakas, S.-Y. Lee, and J. Wrachtrup, "Material platforms for spin-based photonic quantum technologies," *Nature Reviews Materials*, vol. 3, p. 38–51, 2018.

[3] J. Cramer, N. Kalb, M. A. Rol, B. Hensen, M. S. Blok, M. Markham, D. J. Twitchen, R. Hanson, and T. H. Taminiau, "Repeated quantum error correction on a continuously encoded qubit by real-time feedback," *Nature Communications*, vol. 7, p. 11526, 2016.

[4] D. L. Moehring, P. Maunz, S. Olmschenk, K. C. Younge, D. N. Matsukevich, L.-M. Duan, and C. Monroe, "Entanglement of single-atom quantum bits at a distance," *Nature*, vol. 449, p. 68–71, 2007.

[5] S. Ritter, C. Nölleke, C. Hahn, A. Reiserer, A. Neuzner, M. Uphoff, M. Mücke, E. Figueroa, J. Bochmann, and G. Rempe, "An elementary quantum network of single atoms in optical cavities," *Nature*, vol. 484, p. 195–200, 2012.

[6] D. D. Awschalom, R. Hanson, J. Wrachtrup, and B. B. Zhou, "Quantum technologies with optically interfaced solid-state spins," *Nature Photonics*, vol. 12, p. 516–527, 2018.

[7] C. Bradley, J. Randall, M. Abobeih, R. Berrevoets, M. Degen, M. Bakker, M. Markham, D. Twitchen, and T. Taminiau, "A Ten-Qubit Solid-State Spin Register with Quantum Memory up to One Minute," *Physical Review X*, vol. 9, no. 3, p. 031045, 2019.

[8] B. Hensen, H. Bernien, A. E. Dréau, A. Reiserer, N. Kalb, M. S. Blok, J. Ruitenberg, R. F. L. Vermeulen, R. N. Schouten, C. Abellán, W. Amaya, V. Pruneri, M. W. Mitchell, M. Markham, D. J. Twitchen, D. Elkouss, S. Wehner, T. H. Taminiau, and R. Hanson, "Loophole-free Bell inequality violation using electron spins separated by 1.3 kilometres," *Nature*, vol. 526, p. 682–686, 2015.

[9] P. C. Humphreys, N. Kalb, J. P. J. Morits, R. N. Schouten, R. F. L. Vermeulen, D. J. T. M. Markham, and R. Hanson, "Deterministic delivery of remote entanglement on a quantum network," *Nature*, vol. 558, p. 268–273, 2018.

[10] M. K. Bhaskar, R. Riedinger, B. Machielse, D. S. Levonian, C. T. Nguyen, E. N. Knall, H. Park, D. Englund, M. Lončar, D. D. Sukachev, and M. D. Lukin, "Experimental demonstration of memory-enhanced quantum communication," *Nature*, vol. 580, p. 60–64, 2019.

[11] W. J. Munro, K. A. Harrison, A. M. Stephens, S. J. Devitt, and K. Nemoto, "From quantum multiplexing to high-performance quantum networking," *Nature Photonics*, vol. 4, p. 792–796, 2010.

[12] S. Muralidharan, L. Li, J. Kim, N. Lütkenhaus, M. D. Lukin, and L. Jiang, "Optimal architectures for long distance quantum communication," *Scientific Reports*, vol. 6, p. 20463, 2016.

[13] K. Nemoto, M. Trupke, S. J. Devitt, A. M. Stephens, B. Scharfenberger, K. Buczak, T. Nöbauer, M. S. Everitt, J. Schmiedmayer, and W. J. Munro, "Photonic Architecture for Scalable Quantum Information Processing in Diamond," *Physical Review X*, vol. 4, no. 3, p. 031022, 2014.

[14] C. Monroe, R. Raussendorf, A. Ruthven, K. R. Brown, P. Maunz, L.-M. Duan, and J. Kim, "Large-scale modular quantum-computer architecture with atomic memory and photonic interconnects," *Physical Review A*, vol. 89, no. 2, p. 022317, 2014.

[15] N. H. Nickerson, J. F. Fitzsimons, and S. C. Benjamin, "Freely Scalable Quantum Technologies Using Cells of 5-to-50 Qubits with Very Lossy and Noisy Photonic Links," *Physical Review X*, vol. 4, no. 4, p. 041041, 2014.

[16] L. Robledo, L. Childress, H. Bernien, B. Hensen, P. F. A. Alkemade, and R. Hanson, "High-fidelity projective read-out of a solid-state spin quantum register," *Nature*, vol. 477, p. 574–578, 2011.

[17] M. W. Doherty, N. B. Manson, P. Delaney, F. Jelezko, J. Wrachtrup, and L. C. L. Hollenberg, "The nitrogen-vacancy colour centre in diamond," *Physics Reports*, vol. 528, no. 1, pp. 1–45, 2013.

[18] N. Bar-Gill, L. M. Pham, A. Jarmola, D. Budker, and R. L. Walsworth, "Solid-state electronic spin coherence time approaching one second," *Nature Communications*, vol. 4, p. 1743, 2013.

[19] S. D. Barrett and P. Kok, "Efficient high-fidelity quantum computation using matter qubits and linear optics," *Physical Review A*, vol. 71, no. 6, p. 060310(R), 2005.

[20] L. Li, T. Schr$\acute{}$oder, E. H. Chen, M. Walsh, I. Bayn, J. Goldstein, O. Gaathon, M. E. Trusheim, M. Lu, J. Mower, M. Cotlet, M. L. Markham, D. J. Twitchen, and D. Englund, "Coherent spin control of a nanocavity-enhanced qubit in diamond," *Nature Communications*, vol. 6, p. 6173, 2015.

[21] L. J. Rogers, K. D. Jahnke, M. W. Doherty, A. Dietrich, L. P. McGuinness, C. Ḿuller, T. Teraji, H. Sumiya, J. Isoya, N. B. Manson, and F. Jelezko, "Electronic structure of the negatively charged silicon-vacancy center in diamond," *Physical Review B*, vol. 89, p. 235101, 2014.

[22] T. Ḿuller, C. Hepp, B. Pingault, E. Neu, S. Gsell, M. Schreck, H. Sternschulte, D. Steinḿuller-Nethl, C. Becher, and M. Atat́ure, "Optical signatures of silicon-vacancy spins in diamond," *Nature Communications*, vol. 5, p. 3328, 2014.

[23] D. Sukachev, A. Sipahigil, C. Nguyen, M. Bhaskar, R. Evans, F. Jelezko, and M. Lukin, "Silicon-Vacancy Spin Qubit in Diamond: A Quantum Memory Exceeding 10 ms with Single-Shot State Readout," *Physical Review Letters*, vol. 119, no. 22, p. 223602, 2017.

[24] M. Bhaskar, D. Sukachev, A. Sipahigil, R. Evans, M. Burek, C. Nguyen, L. Rogers, P. Siyushev, M. Metsch, H. Park, F. Jelezko, M. Lončar, and M. Lukin, "Quantum Nonlinear Optics with a Germanium-Vacancy Color Center in a Nanoscale Diamond Waveguide," *Physical Review Letters*, vol. 118, no. 22, p. 223603, 2017.

[25] Y.-I. Sohn, S. Meesala, B. Pingault, H. A. Atikian, J. Holzgrafe, M. Gündoğan, C. Stavrakas, M. J. Stanley, A. Sipahigil, J. Choi, M. Zhang, J. L. Pacheco, J. Abraham, E. Bielejec, M. D. Lukin, M. Atatüre, and M. Lončar, "Controlling the coherence of a diamond spin qubit through its strain environment," *Nature Communications*, vol. 9, p. 2012, 2018.

[26] M. H. Metsch, K. Senkalla, B. Tratzmiller, J. Scheuer, M. Kern, J. Achard, A. Tallaire, M. B. Plenio, P. Siyushev, and F. Jelezko, "Initialization and Readout of Nuclear Spins via a Negatively Charged Silicon-Vacancy Center in Diamond," *Physical Review Letters*, vol. 122, p. 190503, 2019.

[27] R. E. Evans, A. Sipahigil, D. D. Sukachev, A. S. Zibrov, and M. D. Lukin, "Narrow-Linewidth Homogeneous Optical Emitters in Diamond Nanostructures via Silicon Ion Implantation," *Physical Review Applied*, vol. 5, p. 044010, 2016.

[28] S. B. van Dam, M. Walsh, M. J. Degen, E. Bersin, S. L. Mouradian, A. Galiullin, M. Ruf, M. IJspeert, T. H. Taminiau, R. Hanson, and D. R. Englund, "Optical coherence of diamond nitrogen-vacancy centers formed by ion implantation and annealing," *Physical Review B*, vol. 99, p. 161203(R), 2019.

[29] M. E. Trusheim, N. H. Wan, K. C. Chen, C. J. Ciccarino, J. Flick, R. Sundararaman, G. Malladi, E. Bersin, M. Walsh, B. Lienhard, H. Bakhru, P. Narang, and D. Englund, "Lead-related quantum emitters in diamond," *Physical Review B*, vol. 99, no. 7, p. 075430, 2019.

[30] M. E. Trusheim, B. Pingault, N. H. Wan, M. Gündoğan, L. D. Santis, R. Debroux, D. Gangloff, C. Purser, K. C. Chen, M. Walsh, J. J. Rose, J. N. Becker,

B. Lienhard, E. Bersin, I. Paradeisanos, G. Wang, D. Lyzwa, A. R.-P. Montblanch, G. Malladi, H. Bakhru, A. C. Ferrari, I. A. Walmsley, M. Atatüre, and D. Englund, "Transform-Limited Photons From a Coherent Tin-Vacancy Spin in Diamond," *Physical Review Letter*, vol. 124, no. 2, p. 023602, 2020.

[31] B. J. Metcalf, J. B. Spring, P. C. Humphreys, N. Thomas-Peter, M. Barbieri, W. S. Kolthammer, X.-M. Jin, N. K. Langford, D. Kundys, J. C. Gates, B. J. Smith, P. G. R. Smith, and I. A. Walmsley, "Quantum teleportation on a photonic chip," *Nature Photonics*, vol. 8, p. 770–774, 2014.

[32] J.-H. Kim, S. Aghaeimeibodi, C. J. K. Richardson, R. P. Leavitt, D. Englund, and E. Waks, "Hybrid Integration of Solid-State Quantum Emitters on a Silicon Photonic Chip," *Nano Letter*, vol. 17, no. 12, pp. 7394–7400, 2017.

[33] A. W. Elshaari, I. E. Zadeh, A. Fognini, M. E. Reimer, D. Dalacu, P. J. Poole, V. Zwiller, and K. D. Jöns, "On-chip single photon filtering and multiplexing in hybrid quantum photonic circuits," *Nature Communications*, vol. 8, p. 379, 2017.

[34] F. Najafi, J. Mower, N. C. Harris, F. Bellei, A. Dane, C. Lee, X. Hu, P. Kharel, F. Marsili, S. Assefa, K. K. Berggren, and D. Englund, "On-chip detection of non-classical light by scalable integration of single-photon detectors," *Nature Communications*, vol. 6, p. 5873, 2015.

[35] S. L. Mouradian, T. Schröder, C. B. Poitras, L. Li, J. Goldstein, E. H. Chen, M. Walsh, C. Cardenas, M. L. Markham, D. J. Twitchen, M. Lipson, and D. Englund, "Freely Scalable Quantum Technologies Using Cells of 5-to-50 Qubits with Very Lossy and Noisy Photonic Links," *Physical Review X*, vol. 5, no. 3, p. 031009, 2015.

[36] I. E. Zadeh, A. W. Elshaari, K. D. Jöns, A. Fognini, D. Dalacu, P. J. Poole, M. E. Reimer, and V. Zwiller, "Deterministic Integration of Single Photon Sources in Silicon Based Photonic Circuits," *Nano Letter*, vol. 16, no. 14, pp. 2289–2294, 2016.

[37] E. R. Schmidgall, S. Chakravarthi, M. Gould, I. R. Christen, K. Hestroffer, F. Hatami, and K.-M. C. Fu, "Frequency Control of Single Quantum Emitters in Integrated Photonic Circuits," *Nano Letter*, vol. 18, no. 2, pp. 1175–1179, 2018.

[38] K. K. Mehta, C. D. Bruzewicz, R. McConnell, R. J. Ram, J. M. Sage, and J. Chiaverini, "Integrated optical addressing of an ion qubit," *Nature Nanotechnology*, vol. 11, p. 1066–1070, 2016.

[39] A. Dibos, M. Raha, C. Phenicie, and J. Thompson, "Atomic Source of Single Photons in the Telecom Band," *Physical Review Letters*, vol. 120, no. 24, p. 243601, 2018.

[40] T. Zhong, J. M. Kindem, J. G. Bartholomew, J. Rochman, I. Craiciu, V. Verma, S. W. Nam, F. Marsili, M. D. Shaw, A. D. Beyer, and A. Faraon, "Optically Addressing Single Rare-Earth Ions in a Nanophotonic Cavity," *Physical Review Letters*, vol. 121, no. 18, p. 183603, 2018.

[41] T. J. A. Mori, R. D. D. Pace, A. M. H. de Andrade, M. A. Corrêa, P. Stamenov, L. F. Schelp, and L. S. Dorneles, "Growth of *c*-axis-oriented aluminum nitride thin films onto different substrates and buffer layers," *Surface and Interface Analysis*, vol. 47, pp. 447–453, 2014.

[42] Z. Chen, S. Newman, D. Brown, R. Chung, S. Keller, U. K. Mishra, S. P. Denbaars, , and S. Nakamura, "High quality AlN grown on SiC by metal organic chemical vapor deposition," *Applied Physics Letters*, vol. 93, p. 191906, 2008.

[43] H. Seo, M. Govoni, and G. Galli, "Design of defect spins in piezoelectric aluminum nitride for solid-state hybrid quantum technologies," *Scientific Reports*, vol. 6, p. 20803, 2016.

[44] T.-J. Lu, M. Fanto, H. Choi, P. Thomas, J. Steidle, S. Mouradian, W. Kong, D. Zhu, H. Moon, K. Berggren, J. Kim, M. Soltani, S. Preble, and D. Englund, "Aluminum nitride integrated photonics platform for the ultraviolet to visible spectrum," *Optics Express*, vol. 26, no. 9, pp. 11147–11160, 2018.

[45] R. Krischek, W. Wieczorek, A. Ozawa, N. Kiesel, P. Michelberger, T. Udem, and H. Weinfurter, "Ultraviolet enhancement cavity for ultrafast nonlinear optics and high-rate multiphoton entanglement experiments," *Nature Photonics*, vol. 4, no. 3, pp. 170–173, 2010.

[46] M. Soltani, R. Soref, T. Palacios, and D. Englund, "AlGaN/AlN integrated photonics platform for the ultraviolet and visible spectral range," *Optics Express*, vol. 24, no. 22, pp. 25415–25423, 2016.

[47] H. Choi, M. Pant, S. Guha, and D. Englund, "Percolation-based architecture for cluster state creation using photon-mediated entanglement between atomic memories," *NPJ Quantum Information*, vol. 5, p. 104, 2019.

[48] L.-M. Duan and C. Monroe, "*Colloquium*: quantum networks with trapped ions," *Review of Modern Physics*, vol. 82, no. 2, pp. 1209–1224, 2010.

[49] E. Togan, Y. Chu, A. S. Trifonov, L. Jiang, J. Maze, L. Childress, M. V. G. Dutt, A. S. Sørensen, P. R. Hemmer, A. S. Zibrov, and M. D. Lukin, "Quantum entanglement between an optical photon and a solid-state spin qubit," *Nature*, vol. 466, no. 7307, pp. 730–734, 2010.

[50] L. Childress, R. Walsworth, and M. Lukin, "Atom-like crystal defects: From quantum computers to biological sensors," *Physics Today*, vol. 67, no. 10, pp. 38–43, 2014.

[51] C. Xiong, W. H. P. Pernice, X. Sun, C. Schuck, K. Y. Fong, and H. X. Tang, "Aluminum nitride as a new material for chip-scale optomechanics and nonlinear optics," *New Journal of Physics*, vol. 14, p. 095014, 2012.

[52] C. Xiong, W. H. P. Pernice, and H. X. Tang, "Low-Loss, Silicon Integrated, Aluminum Nitride Photonic Circuits and Their Use for Electro-Optic Signal Processing," *Nano Letter*, vol. 12, no. 7, pp. 3562–3568, 2012.

[53] C. Xiong, X. Sun, K. Y. Fong, and H. X. Tang, "Integrated high frequency aluminum nitride optomechanical resonators," *Applied Physics Letters*, vol. 100, no. 17, p. 171111, 2012.

[54] S. P. Fang and H. F. Taylor, "High-performance single-mode fiber-optic switch," *Optics Letters*, vol. 19, pp. 1204–1206, 1994.

[55] W. H. P. Pernice, C. Xiong, C. Schuck, and H. X. Tang, "Second harmonic generation in phase matched aluminum nitride waveguides and micro-ring resonators," *Applied Physics Letters*, vol. 100, no. 22, p. 223501, 2012.

[56] Y. Fujii, S. Yoshida, S. Misawa, S. Maekawa, and T. Sakudo, "Nonlinear optical susceptibilities of AlN film," *Applied Physics Letters*, vol. 31, no. 12, pp. 815–816, 1977.

[57] H. Jung, C. Xiong, K. Y. Fong, X. Zhang, and H. X. Tang, "Optical frequency comb generation from aluminum nitride microring resonator," *Optics Letters*, vol. 38, no. 15, pp. 2810–2813, 2013.

[58] H. Jung, R. Stoll, X. Guo, D. Fischer, and H. X. Tang, "Green, red, and IR frequency comb line generation from single IR pump in AlN microring resonator," *Optica*, vol. 1, no. 6, pp. 396–399, 2014.

[59] X. Guo, C.-L. Zou, H. Jung, and H. X. Tang, "On-Chip Strong Coupling and Efficient Frequency Conversion between Telecom and Visible Optical Modes," *Physical Review Letters*, vol. 117, no. 12, p. 123902, 2016.

[60] X. Liu, C. Sun, B. Xiong, L. Wang, J. Wang, Y. Han, Z. Hao, H. Li, Y. Luo, J. Yan, T. Wei, Y. Zhang, and J. Wang, "Integrated continuous-wave aluminum nitride Raman laser," *Optica*, vol. 4, no. 8, pp. 893–896, 2017.

[61] T. Troha, M. Rigler, D. Alden, I. Bryan, W. Guo, R. Kirste, S. Mita, M. D. Gerhold, R. Collazo, Z. Sitar, and M. Zgonik, "UV second harmonic generation in AlN waveguides with modal phase matching," *Optics Material Express*, vol. 6, no. 6, pp. 2014–2023, 2016.

[62] H. Jung and H. X. Tang, "Aluminum nitride as nonlinear optical material for on-chip frequency comb generation and frequency conversion," *Nanophotonics*, vol. 5, no. 2, pp. 263–271, 2016.

[63] X. Guo, C.-L. Zou, C. Schuck, H. Jung, R. Cheng, and H. X. Tang, "Parametric down-conversion photon-pair source on a nanophotonic chip," *Light: Science & Applications*, vol. 6, no. 5, p. e16249, 2017.

[64] X. Liu, C. Sun, B. Xiong, L. Wang, J. Wang, Y. Han, Z. Hao, H. Li, Y. Luo, J. Yan, T. Wei, Y. Zhang, and J. Wang, "Integrated High-Q Crystalline AlN Microresonators for Broadband Kerr and Raman Frequency Combs," *ACS Photonics*, vol. 5, no. 5, pp. 1943–1950, 2018.

[65] P. T. Lin, H. Jung, L. C. Kimerling, A. Agarwal, and H. X. Tang, "Low-loss aluminium nitride thin film for mid-infrared microphotonics," *Laser & Photonics Review*, vol. 8, no. 2, pp. L23–L28, 2014.

[66] A. Patra, R. E. Tallman, and B. A. Weinstein, "Effect of crystal structure and dopant concentration on the luminescence of Cr^{3+} in Al_2O_3 nanocrystals," *Optical Materials*, vol. 27, no. 8, pp. 1396–1401, 2005.

[67] I. Parkhomenko, L. Vlasukova, F. Komarov, O. Milchanin, M. Makhavikou, A. Mudryi, V. Zhivulko, J. Żuk, P. Kopyciński, and D. Murzalinov, "Origin of visible photoluminescence from Si-rich and N-rich silicon nitride films," *Thin Solid Films*, vol. 626, pp. 70–75, 2017.

[68] C. Monroe and J. Kim, "Scaling the ion trap quantum processor," *Science*, vol. 339, no. 6124, pp. 1164–1169, 2013.

[69] A. Goban, C.-L. Hung, S.-P. Yu, J. D. Hood, J. A. Muniz, J. H. Lee, M. J. Martin, A. C. McClung, K. S. Choi, D. E. Chang, O. Painter, and H. J. Kimble, "Atom-light interactions in photonic crystals," *Nature Communications*, vol. 5, p. 3808, 2014.

[70] J. K. W. Yang and K. K. Berggren, "Using high-contrast salty development of hydrogen silsesquioxane for sub-10-nm half-pitch lithography," *Journal of Vacuum Science & Technology B*, vol. 25, no. 6, p. 2025, 2007.

[71] S. A. Miller, M. Yu, X. Ji, A. G. Griffith, J. Cardenas, A. L. Gaeta, and M. Lipson, "Low-loss silicon platform for broadband mid-infrared photonics," *Optica*, vol. 4, no. 7, pp. 707–712, 2017.

[72] A. Yariv, "Critical coupling and its control in optical waveguide-ring resonator systems," *IEEE Photonics Technology Letters*, vol. 14, no. 4, pp. 483–485, 2002.

[73] A. Yariv, "Universal relations for coupling of optical power between microresonators and dielectric waveguides," *Electronics Letters*, vol. 36, no. 4, pp. 321–322, 2000.

[74] J. Levy, "Integrated nonlinear optics in silicon nitride waveguides and resonators," *PhD Thesis*, 2011.

[75] A. Dutt, "On-chip Quantum and Nonlinear Optics: From Squeezing to Spectroscopy," *PhD Thesis*, 2017.

[76] J. Mower, N. C. Harris, G. R. Steinbrecher, Y. Lahini, and D. Englund, "High-fidelity quantum state evolution in imperfect photonic integrated circuits," *Physical Review A*, vol. 92, no. 3, p. 032322, 2015.

[77] J. C. Mikkelsen, W. D. Sacher, and J. K. S. Poon, "Dimensional variation tolerant silicon-on-insulator directional couplers," *Optics Express*, vol. 22, no. 3, pp. 3145–3150, 2014.

[78] M. Stegmaier, J. Ebert, J. M. Meckbach, K. Ilin, M. Siegel, and W. H. P. Pernice, "Aluminum nitride nanophotonic circuits operating at ultraviolet wavelengths," *Applied Physics Letters*, vol. 104, no. 9, p. 091108, 2014.

[79] X. Liu, C. Sun, B. Xiong, L. Wang, J. Wang, Y. Han, Z. Hao, H. Li, Y. Luo, J. Yan, T. Wei, Y. Zhang, and J. Wang, "Aluminum nitride-on-sapphire platform for integrated high-Q microresonators," *Optics Express*, vol. 25, no. 2, pp. 587–594, 2017.

[80] A. Gorin, A. Jaouad, E. Grondin, V. Aimez, and P. Charette, "Fabrication of silicon nitride waveguides for visible-light using PECVD: a study of the effect of plasma frequency on optical properties," *Optics Express*, vol. 16, no. 18, pp. 13509–13516, 2008.

[81] L. Hoffman, A. Subramanian, P. Helin, B. D. Bois, R. Baets, P. V. Dorpe, G. Gielen, R. Puers, and D. Braeken, "Low Loss CMOS-Compatible PECVD Silicon Nitride Waveguides and Grating Couplers for Blue Light Optogenetic Applications," *IEEE Photonics Journal*, vol. 8, no. 5, p. 2701211, 2016.

[82] D. Y. Oh, K. Y. Yang, C. Fredrick, G. Ycas, S. A. Diddams, and K. J. Vahala, "Coherent ultra-violet to near-infrared generation in silica ridge waveguides," *Nature Communications*, vol. 8, p. 13922, 2017.

[83] H. Lee, T. Chen, J. Li, O. Painter, and K. J. Vahala, "Ultra-low-loss optical delay line on a silicon chip," *Nature Communications*, vol. 3, p. 867, 2012.

[84] M. J. R. Heck, J. F. Bauters, M. L. Davenport, D. T. Spencer, and J. E. Bowers, "Ultra-low loss waveguide platform and its integration with silicon photonics," *Laser Photonics Review*, vol. 8, no. 5, pp. 667–686, 2014.

[85] G. Poberaj, R. Degl'Innocenti, C. Medrano, and P. Günter, "UV integrated optics devices based on beta-barium borate," *Optical Materials*, vol. 31, no. 7, pp. 1049–1053, 2009.

[86] J. Schroeder, R. Mohr, C. J. Montrose, and P. B. Macedo, "Light Scattering in a Number of Optical Grade Glasses," *Journal of Non-Crystalline Solids*, vol. 13, no. 2, pp. 313–320, 1980.

[87] B. Aspar, H. Moriceau, E. Jalaguier, C. Lagahe, A. Soubie, B. Biasse, A. M. Papon, A. Claverie, J. Grisolia, G. Benassayag, F. Letertre, O. Rayssac, T. Barge, C. Maleville, and B. Ghyselen, "The Generic Nature of the Smart-Cut® Process for Thin Film Transfer," *Journal of Electronic Materials*, vol. 30, pp. 834–840, 2001.

[88] H. Miyake, C. H. Lin, K. Tokoro, and K. Hiramatsu, "Preparation of high-quality AlN on sapphire by high-temperature face-to-face annealing," *Journal of Crystal Growth*, vol. 456, pp. 155–159, 2016.

[89] B. Karunagaran, S. J. Chung, S. Velumani, and E.-K. Suh, "Effect of rapid thermal annealing on the properties of PECVD SiN_x thin films," *Materials Chemistry and Physics*, vol. 106, no. 1, pp. 130–133, 2007.

[90] M. Feneberg, R. A. R. Leute, B. Neuschl, K. Thonke, and M. Bickermann, "High-excitation and high-resolution photoluminescence spectra of bulk AlN," *Physical Review B*, vol. 82, no. 7, p. 075208, 2010.

[91] R. H. French, "Electronic Band Structure of Al_2O_3, with Comparison to AlON and AlN," *Journal of the American Ceramic Society*, vol. 73, no. 3, pp. 477–489, 1990.

[92] A. Majkić, U. Puc, A. Franke, R. Kirste, R. Collazo, Z. Sitar, and M. Zgonik, "Optical properties of aluminum nitride single crystals in the THz region," *Optical Materials Express*, vol. 5, no. 10, pp. 2106–2111, 2015.

[93] A. Majkić, U. Puc, A. Franke, R. Kirste, R. Schlesser, R. Collazo, Z. Sitar, and M. Zgonik, "Optical nonlinear and electro-optical coefficients in bulk aluminium nitride single crystals," *Physica Status Solidi B*, vol. 254, no. 9, p. 1700077, 2017.

[94] D. J. Moss, R. Morandotti, A. L. Gaeta, and M. Lipson, "New CMOS-compatible platforms based on silicon nitride and Hydex for nonlinear optics," *Nature Photonics*, vol. 7, pp. 597–607, 2013.

[95] J. S. Levy, A. Gondarenko, M. A. Foster, A. C. Turner-Foster, A. L. Gaeta, and M. Lipson, "CMOS-compatible multiple wavelength oscillator for on-chip optical interconnects," *Nature Photonics*, vol. 4, no. 1, pp. 37–40, 2009.

[96] D. Néel, I. Roland, X. Checoury, M. E. Kurdi, S. Sauvage, P. Boucaud, C. Brimont, T. Guillet, B. Gayral, and F. Semond, "AlN photonic crystals and microdisks for UV nanophotonics," *Advances in Natural Sciences: Nanoscience and Nanotechnology*, vol. 5, p. 023001, 2014.

[97] J. Sellés, C. Brimont, G. Cassabois, P. Valvin, T. Guillet, I. Roland, Y. Zeng, X. Checoury, P. Boucaud, M. Mexis, F. Semond, and B. Gayral, "Deep-UV nitride-on-silicon microdisk lasers," *Scientific Reports*, vol. 6, p. 21650, 2016.

[98] G. Piazza, P. J. Stephanou, and A. P. Pisano, "Piezoelectric aluminum nitride vibrating contour-mode MEMS resonators," *Journal of Microelectromechanical Systems*, vol. 15, no. 6, pp. 1406–1418, 2006.

[99] C. M. Lueng, H. L. W. Chan, C. Surya, and C. L. Choy, "Piezoelectric coefficient of aluminum nitride and gallium nitride," *Journal of Applied Physics*, vol. 88, no. 9, pp. 5360–5363, 2000.

[100] S. Miller, Y.-H. D. Lee, J. Cardenas, A. L. Gaeta, and M. Lipson, "Electro-optic effect in silicon nitride," *Conference on Lasers and Electro-Optics, SF1G.4*, 2015.

[101] A. Z. Subramanian, P. Neutens, A. Dhakal, R. Jansen, T. Claes, X. Rottenberg, F. Peyskens, S. Selvaraja, P. Helin, B. D. Bois, K. Leyssens, S. Severi, P. Deshpande, R. Baets, and P. V. Dorpe, "Low-loss singlemode PECVD silicon nitride photonic wire waveguides for 532-900 nm wavelength window fabricated within a CMOS pilot line," *IEEE Photonics Journal*, vol. 5, no. 6, p. 2202809, 2013.

[102] P. Muellner, A. Maese-Novo, E. Melnik, R. Hainberger, G. Koppitsch, J. Kraft, and G. Meinhardt, "CMOS-compatible low-loss silicon nitride waveguide integration platform for interferometric sensing," *European Conference on Integrated Optics*, 2016.

[103] K. Ikeda, R. E. Saperstein, N. Alic, and Y. Fainman, "Thermal and Kerr nonlinear properties of plasma-deposited silicon nitride/ silicon dioxide waveguides," *Optics Express*, vol. 16, no. 17, pp. 12987–12994, 2008.

[104] P. M. Thomas, M. Fanto, J. Serafini, J. Steidle, S. Preble, T.-J. Lu, and D. Englund, "Ion milled facet for direct coupling to optical waveguides," *Micro-and Nanotechnology Sensors, Systems, and Applications XI, 109823H*, 2019.

[105] T.-J. Lu, B. Lienhard, K.-Y. Jeong, H. Moon, A. Iranmanesh, G. Grosso, and D. Englund, "Bright high-purity quantum emitters in aluminium nitride integrated photonics," *arXiv:2006.16276*, 2020.

[106] P. Siyushev, M. H. Metsch, A. Ijaz, J. M. Binder, M. K. Bhaskar, D. D. Sukachev, A. Sipahigil, R. E. Evans, C. T. Nguyen, M. D. Lukin, P. R. Hemmer, Y. N. Palyanov, I. N. Kupriyanov, Y. M. Borzdov, L. J. Rogers, and F. Jelezko, "Optical and microwave control of germanium-vacancy center spins in diamond," *Physical Review B*, vol. 96, no. 8, p. 081201(R), 2017.

[107] J. Becker and C. Becher, "Coherence Properties and Quantum Control of Silicon Vacancy Color Centers in Diamond," *Physica Status Solidi A*, vol. 214, no. 11, p. 1700586, 2017.

[108] B. Lienhard, T. Schröder, S. Mouradian, F. Dolde, T. T. Tran, I. Aharonovich, and D. Englund, "Bright and photostable single-photon emitter in silicon carbide," *Optica*, vol. 3, no. 7, pp. 768–774, 2016.

[109] S. Castelletto, B. C. Johnson, V. Ivády, N. Stavrias, T. Umeda, A. Gali, and T. Ohshima, "A silicon carbide room-temperature single-photon source," *Nature Materials*, vol. 13, p. 151–156, 2014.

[110] G. Wolfowicz, C. P. Anderson, B. Diler, O. G. Poluektov, F. J. Heremans, and D. D. Awschalom, "Vanadium spin qubits as telecom quantum emitters in silicon carbide," *Science Advances*, vol. 6, no. 18, p. eaaz1192, 2020.

[111] J. R. Weber, W. F. Koehl, J. B. Varley, A. Janotti, B. B. Buckley, C. G. V. de Walle, and D. D. Awschalom, "Quantum computing with defects," *Proceedings of the National Academy of Sciences*, vol. 107, no. 19, pp. 8513–8518, 2010.

[112] S. Zaiser, T. Rendler, I. Jakobi, T. W. nad S.-Y. Lee, S. Wagner, V. Bergholm, T. Schulte-Herbrüggen, P. Neumann, and J. org Wrachtrup, "Enhancing quantum sensing sensitivity by a quantum memory," *Nature Communications*, vol. 7, p. 12279, 2016.

[113] T. T. Tran, K. Bray, M. J. Ford, M. Toth, and I. Aharonovich, "Quantum emission from hexagonal boron nitride monolayers," *Nature Nanotechnology*, vol. 11, p. 37–41, 2016.

[114] A. M. Berhane, K. Jeong, Z. Bodrog, S. Fiedler, T. Schröder, N. V. Triviño, T. Palacios, A. Gali, M. Toth, D. Englund, and I. Aharonovich, "Bright Room-Temperature Single-Photon Emission from Defects in Gallium Nitride," *Advanced Materials*, vol. 29, no. 12, p. 1605092, 2017.

[115] B. Lienhard, T.-J. Lu, K.-Y. Jeong, H. Moon, A. Iranmanesh, G. Grosso, and D. Englund, "High-Purity Single Photon Emitter in Aluminum Nitride Photonic Integrated Circuit," *European Conference on Lasers and Electro-Optics and European Quantum Electronics Conference, EA_6_6*, 2017.

[116] S. Kim, N. M. H. Duong, M. Nguyen, T. Lu, M. Kianinia, N. Mendelson, A. Solntsev, C. Bradac, D. R. Englund, and I. Aharonovich, "Integrated on Chip Platform with Quantum Emitters in Layered Materials," *Advanced Optical Materials*, vol. 7, no. 23, p. 1901132, 2019.

[117] S. Maity, L. Shao, S. Bogdanović, S. Meesala, Y.-I. Sohn, N. Sinclair, B. Pingault, M. Chalupnik, C. Chia, L. Zheng, K. Lai, and M. Lončar, "Coherent acoustic control of a single silicon vacancy spin in diamond," *Nature Communications*, vol. 11, p. 193, 2020.

[118] J. H. Harris, "Sintered aluminum nitride ceramics for high-power electronic applications," *The Journal of The Minerals, Metals & Materials Society (TMS)*, vol. 50, no. 6, p. 56–60, 1998.

[119] Y. Hou, M. Zhang, G. Han, C. Si, Y. Zhao, and J. Ning, "A review: Aluminum nitride MEMS contour-mode resonator," *Journal of Semiconductors*, vol. 37, no. 10, p. 101001, 2016.

[120] N. H. Wan, T.-J. Lu, K. C. Chen, M. P. Walsh, M. E. Trusheim, L. D. Santis, E. A. Bersin, I. B. Harris, S. L. Mouradian, I. R. Christen, E. S. Bielejec, and D. Englund, "Large-scale integration of artificial atoms in hybrid photonic circuits," *Nature*, vol. 583, no. 7815, pp. 226–231, 2020.

[121] L. I. Berger, *Semiconductor Materials*. CRC Press, 1996.

[122] W. T. Silfvast, *Laser Fundamentals*. Cambridge University Press, 1996.

[123] E. Neu, M. Agio, and C. Becher, "Photophysics of single silicon vacancy centers in diamond: implications for single photon emission," *Optics Express*, vol. 20, no. 18, pp. 19956–19971, 2012.

[124] V. Hizhnyakov and P. Reineker, "Optical dephasing by fluctuations of long-range interactions in defect-rich crystals," *Journal of Luminescence*, vol. 83-84, pp. 351–355, 1999.

[125] S. C. Kitson, P. Jonsson, J. G. Rarity, and P. R. Tapster, "Intensity fluctuation spectroscopy of small numbers of dye molecules in a microcavity," *Physical Review A*, vol. 58, p. 620, 1998.

[126] I. Aharonovich, S. Castelletto, B. C. Johnson, J. C. McCallum, D. A. Simpson, A. D. Greentree, and S. Prawer, "Chromium single-photon emitters in diamond fabricated by ion implantation," *Physical Review B*, vol. 81, no. 12, p. 121201(R), 2010.

[127] Y. Xue, H. Wang, N. Xie, Q. Yang, F. Xu, B. Shen, J.-J. Shi, D. Jiang, X. Dou, T. Yu, and B.-Q. Sun, "Single-Photon Emission from Point Defects in Aluminum Nitride Films," *The Journal of Physical Chemistry Letters*, vol. 11, no. 7, p. 2689–2694, 2020.

[128] G. Grosso, H. Moon, C. Ciccarino, J. Flick, N. Mendelson, L. Mennel, M. Toth, I. Aharonovich, P. Narang, and D. R. Englund, "Low-Temperature Electron–Phonon Interaction of Quantum Emitters in Hexagonal Boron Nitride," *ACS Photonics*, vol. 7, no. 6, p. 1410–1417, 2020.

[129] J. Miao, P. Ercius, and S. J. L. Billinge, "Atomic electron tomography: 3D structures without crystals," *Science*, vol. 353, no. 6306, p. aaf2157, 2016.

[130] D. Zhu, Q.-Y. Zhao, H. Choi, T.-J. Lu, A. E. Dane, D. Englund, and K. K. Berggren, "A scalable multi-photon coincidence detector based on superconducting nanowires," *Nature Nanotechnology*, vol. 13, p. 596–601, 2018.

[131] W. Bi, H. Kuo, P. Ku, and B. Shen, *Handbook of GaN Semiconductor Materials and Devices*. CRC Press, 2017.

[132] Y. Nagasawa and A. Hirano, "A Review of AlGaN-Based Deep-Ultraviolet Light-Emitting Diodes on Sapphire," *Applied Sciences*, vol. 8, no. 8, p. 1264, 2018.

[133] L. C. Popa and D. Weinstein, "Switchable piezoelectric transduction in AlGaN/GaN MEMS resonators," *Transducers & Eurosensors XXVII: The 17th International Conference on SolidState Sensors, Actuators and Microsystems*, pp. 2461–2464, 2013.

[134] G. Grosso, H. Moon, B. Lienhard, S. Ali, D. K. Efetov, M. M. Furchi, P. Jarillo-Herrero, M. J. Ford, I. Aharonovich, and D. Englund, "Tunable and high-purity room temperature single-photon emission from atomic defects in hexagonal boron nitride," *Nature Communications*, vol. 8, p. 705, 2017.

[135] A. Osada, Y. Ota, R. Katsumi, M. Kakuda, S. Iwamoto, and Y. Arakawa, "Strongly Coupled Single-Quantum-Dot–Cavity System Integrated on a CMOS-Processed Silicon Photonic Chip," *Physical Review Applied*, vol. 11, no. 2, p. 024071, 2019.

[136] X. Liu, A. W. Bruch, Z. Gong, J. Lu, J. B. Surya, L. Zhang, J. Wang, J. Yan, and H. X. Tang, "Ultra-high-Q UV microring resonators based on a single-crystalline AlN platform," *Optica*, vol. 5, no. 10, pp. 1279–1282, 2018.

[137] D. Zhu, H. Choi, T.-J. Lu, Q.-Y. Zhao, A. Dane, F. Najafi, D. R. Englund, and K. K. Berggren, "Superconducting Nanowire Single-Photon Detector on Aluminum Nitride," *Conference on Lasers and Electro-Optics, FTu4C.1*, 2016.

[138] J. N. Becker, B. Pingault, D. Groß, M. Gündoğan, N. Kukharchyk, M. Markham, A. Edmonds, M. Atatüre, P. Bushev, and C. Becher, "All-Optical Control of the Silicon-Vacancy Spin in Diamond at Millikelvin Temperatures," *Physical Review Letters*, vol. 120, no. 5, p. 053603, 2018.

[139] C. Nguyen, D. Sukachev, M. Bhaskar, B. Machielse, D. Levonian, E. Knall, P. Stroganov, R. Riedinger, H. Park, M. Lončar, and M. Lukin, "Quantum Network Nodes Based on Diamond Qubits with an Efficient Nanophotonic Interface," *Physical Review Letters*, vol. 123, no. 18, p. 183602, 2019.

[140] T. Schröder, M. E. Trusheim, M. Walsh, L. Li, J. Zheng, M. Schukraft, A. Sipahigil, R. E. Evans, D. D. Sukachev, C. T. Nguyen, J. L. Pacheco, R. M. Camacho, E. S. Bielejec, M. D. Lukin, and D. Englund, "Scalable focused ion beam creation of nearly lifetime-limited single quantum emitters in diamond nanostructures," *Nature Communications*, vol. 8, p. 15376, 2017.

[141] J. F. Ziegler, M. D. Ziegler, and J. P. Biersack, "SRIM - The stopping and range of ions in matter," *Nuclear Instruments and Methods in Physics Research Section B Beam Interactions with Materials and Atoms*, vol. 268, no. 11-12, pp. 1818–1823, 2010.

[142] N. H. Wan, B. J. Shields, D. Kim, S. Mouradian, B. Lienhard, M. Walsh, H. Bakhru, T. Schröder, and D. Englund, "Efficient Extraction of Light from a Nitrogen-Vacancy Center in a Diamond Parabolic Reflector," *Nano Letters*, vol. 18, no. 5, pp. 2787–2793, 2018.

[143] S. Mouradian, N. H. Wan, T. Schröder, and D. Englund, "Rectangular photonic crystal nanobeam cavities in bulk diamond," *Applied Physics Letters*, vol. 111, no. 2, p. 021103, 2017.

[144] N. H. Wan, S. Mouradian, and D. Englund, "Two-dimensional photonic crystal slab nanocavities on bulk single-crystal diamond," *Applied Physics Letters*, vol. 112, no. 14, p. 141102, 2018.

[145] A. Badolato, K. Hennessy, M. Atatüre, J. Dreiser, E. Hu, P. M. Petroff, and A. Imamoğlu, "Deterministic Coupling of Single Quantum Dots to Single Nanocavity Modes," *Science*, vol. 308, no. 5725, pp. 1158–1161, 2005.

[146] O. Gazzano, S. M. de Vasconcellos, C. Arnold, A. Nowak, E. Galopin, I. Sagnes, L. Lanco, A. Lemaître, and P. Senellart, "Bright solid-state sources of indistinguishable single photons," *Nature Communications*, vol. 4, p. 1425, 2013.

[147] M. Gschrey, F. Gericke, A. Schüßler, R. Schmidt, J.-H. Schulze, T. Heindel, S. Rodt, A. Strittmatter, and S. Reitzensteina), "*In situ* electron-beam lithography of deterministic single-quantum-dot mesa-structures using low-temperature cathodoluminescence spectroscopy," *Applied Physics Letters*, vol. 102, p. 251113, 2013.

[148] L. Sapienza, M. Davanço, A. Badolato, and K. Srinivasan, "Nanoscale optical positioning of single quantum dots for bright and pure single-photon emission," *Nature Communications*, vol. 6, p. 7833, 2015.

[149] H. Bernien, B. Hensen, W. Pfaff, G. Koolstra, M. S. Blok, L. Robledo, T. H. Taminiau, M. Markham, D. J. Twitchen, L. Childress, and R. Hanson, "Heralded entanglement between solid-state qubits separated by three metres," *Nature*, vol. 497, p. 86–90, 2013.

[150] H. Thyrrestrup, G. Kiršanskė, H. L. Jeannic, T. Pregnolato, L. Zhai, L. Raahauge, L. Midolo, N. Rotenberg, A. Javadi, R. Schott, A. D. Wieck, A. Ludwig, M. C. Löbl, I. Söllner, R. J. Warburton, and P. Lodahl, "Quantum Optics with Near-Lifetime-Limited Quantum-Dot Transitions in a Nanophotonic Waveguide," *Nano Letters*, vol. 18, no. 3, pp. 1801–1806, 2018.

[151] D. E. Chang, A. S. Sørensen, E. A. Demler, and M. D. Lukin, "A single-photon transistor using nanoscale surface plasmons," *Nature Physics*, vol. 3, p. 807–812, 2007.

[152] L. Rogers, K. Jahnke, T. Teraji, L. Marseglia, C. Müller, B. Naydenov, H. Schauffert, C. Kranz, J. Isoya, L. McGuinness, and F. Jelezko, "Multiple intrinsically identical single-photon emitters in the solid state," *Nature Communications*, vol. 5, p. 4739, 2014.

[153] S. Meesala, Y.-I. Sohn, B. Pingault, L. Shao, H. A. Atikian, J. Holzgrafe, M. Gündoğan, C. Stavrakas, A. Sipahigil, C. Chia, R. Evans, M. J. Burek,

M. Zhang, L. Wu, J. L. Pacheco, J. Abraham, E. Bielejec, M. D. Lukin, M. Atatüre, and M. Lončar, "Strain engineering of the silicon-vacancy center in diamond," *Physical Review B*, vol. 97, no. 20, p. 205444, 2018.

[154] S. Maity, L. Shao, Y.-I. Sohn, S. Meesala, B. Machielse, E. Bielejec, M. Markham, and M. Lončar, "Spectral Alignment of Single-Photon Emitters in Diamond using Strain Gradient," *Physical Review Applied*, vol. 10, no. 2, p. 024050, 2018.

[155] B. Machielse, S. Bogdanovic, S. Meesala, S. Gauthier, M. Burek, G. Joe, M. Chalupnik, Y. Sohn, J. Holzgrafe, R. Evans, C. Chia, H. Atikian, M. Bhaskar, D. Sukachev, L. Shao, S. Maity, M. Lukin, and M. Lončar, "Quantum Interference of Electromechanically Stabilized Emitters in Nanophotonic Devices," *Physical Review X*, vol. 9, no. 3, p. 031022, 2019.

[156] F. Maier, M. Riedel, B. Mantel, J. Ristein, and L. Ley, "Origin of Surface Conductivity in Diamond," *Physical Review Letters*, vol. 85, no. 16, p. 3472, 2000.

[157] A. Sipahigil, K. Jahnke, L. Rogers, T. Teraji, J. Isoya, A. Zibrov, F. Jelezko, and M. Lukin, "Indistinguishable Photons from Separated Silicon-Vacancy Centers in Diamond," *Physical Review Letters*, vol. 113, no. 11, p. 113602, 2014.

[158] C. K. Hong, Z. Y. Ou, and L. Mandel, "Measurement of subpicosecond time intervals between two photons by interference," *Physical Review Letters*, vol. 59, no. 18, p. 2044, 1987.

[159] T. Grange, N. Somaschi, C. Antón, L. D. Santis, G. Coppola, V. Giesz, A. Lemaître, I. Sagnes, A. Auffèves, , and P. Senellart, "Reducing Phonon-Induced Decoherence in Solid-State Single-Photon Sources with Cavity Quantum Electrodynamics," *Physical Review Letters*, vol. 118, no. 25, p. 253602, 2017.

[160] S. Mouradian and D. Englund, "A tunable waveguide-coupled cavity design for scalable interfaces to solid-state quantum emitters," *APL Photonics*, vol. 2, no. 4, p. 046103, 2017.

[161] C. Bradac, W. Gao, J. Forneris, M. E. Trusheim, and I. Aharonovich, "Quantum nanophotonics with group IV defects in diamond," *Nature Communications*, vol. 10, p. 5625, 2019.

[162] P. Lodahl, S. Mahmoodian, and S. Stobbe, "Interfacing single photons and single quantum dots with photonic nanostructures," *Review of Modern Physics*, vol. 87, no. 2, p. 347, 2015.

[163] N. L. Piparo, W. J. Munro, and K. Nemoto, "Quantum multiplexing," *Physical Review A*, vol. 99, no. 2, p. 022337, 2019.

[164] E. Bersin, M. Walsh, S. L. Mouradian, M. E. Trusheim, T. Schröder, and D. Englund, "Individual control and readout of qubits in a sub-diffraction volume," *NPJ Quantum Information*, vol. 5, p. 38, 2019.

[165] N. C. Harris, J. Carolan, D. Bunandar, M. Prabhu, M. Hochberg, T. Baehr-Jones, M. L. Fanto, A. M. Smith, C. C. Tison, P. M. Alsing, and D. Englund, "Linear programmable nanophotonic processors ," *Optica*, vol. 5, no. 12, pp. 1623–1631, 2018.

[166] C. Taballione, T. A. W. Wolterink, J. Lugani, A. Eckstein, B. A. Bell, R. Grootjans, I. Visscher, D. Geskus, C. G. H. Roeloffzen, J. J. Renema, I. A. Walmsley, P. W. H. Pinkse, and K.-J. Boller, "8×8 reconfigurable quantum photonic processor based on silicon nitride waveguides," *Optics Express*, vol. 27, no. 19, pp. 26842–26857, 2019.

[167] T.-J. Seok, N. Quack, S. Han, R. S. Muller, and M. C. Wu, "Large-scale broadband digital silicon photonic switches with vertical adiabatic couplers," *Optica*, vol. 3, no. 1, pp. 64–70, 2016.

[168] P. R. Stanfield, A. J. Leenheer, C. P. Michael, R. Sims, and M. Eichenfield, "CMOS-compatible, piezo-optomechanically tunable photonics for visible wavelengths and cryogenic temperatures," *Optics Express*, vol. 27, no. 20, pp. 28588–28605, 2019.

[169] B. Patra, R. M. Incandela, J. P. G. van Dijk, H. A. R. Homulle, L. Song, M. Shahmohammadi, R. B. Staszewski, A. Vladimirescu, M. Babaie, F. Sebastiano, and E. Charbon, "Cryo-CMOS Circuits and Systems for Quantum Computing Applications," *IEEE Journal of Solid-State Circuits*, vol. 53, no. 1, pp. 309–321, 2018.

[170] D. Kim, M. I. Ibrahim, C. Foy, M. E. Trusheim, R. Han, and D. R. Englund, "A CMOS-integrated quantum sensor based on nitrogen–vacancy centres," *Nature Electronics*, vol. 2, p. 284–289, 2019.

[171] A. H. Atabaki, S. Moazeni, F. Pavanello, H. Gevorgyan, J. Notaros, L. Alloatti, M. T. Wade, C. Sun, S. A. Kruger, H. Meng, K. A. Qubaisi, I. Wang, B. Zhang, A. Khilo, C. V. Baiocco, M. A. Popović, V. M. Stojanović, and R. J. Ram, "Integrating photonics with silicon nanoelectronics for the next generation of systems on a chip," *Nature*, vol. 556, p. 349–354, 2018.

[172] J. Sun, E. Timurdogan, A. Yaacobi, E. S. Hosseini, and M. R. Watts, "Large-scale nanophotonic phased array," *Nature*, vol. 493, p. 195–199, 2013.

[173] P. Tonndorf, O. D. Pozo-Zamudio, N. Gruhler, J. Kern, R. Schmidt, A. I. Dmitriev, A. P. Bakhtinov, A. I. Tartakovskii, W. Pernice, S. M. de Vasconcellos, and R. Bratschitsch, "On-Chip Waveguide Coupling of a Layered Semiconductor Single-Photon Source," *Nano Letter*, vol. 17, no. 9, p. 5446–5451, 2017.

[174] D. White, A. Branny, R. J. Chapman, R. Picard, M. Brotons-Gisbert, A. Boes, A. Peruzzo, C. Bonato, and B. D. Gerardot, "Atomically-thin quantum dots integrated with lithium niobate photonic chips," *Optical Materials Express*, vol. 9, no. 2, pp. 441–448, 2019.

[175] F. Peyskens, C. Chakraborty, M. Muneeb, D. V. Thourhout, and D. Englund, "Integration of single photon emitters in 2D layered materials with a silicon nitride photonic chip," *Nature Communications*, vol. 10, p. 4435, 2019.

[176] F. Marsili, V. B. Verma, J. A. Stern, S. Harrington, A. E. Lita, T. Gerrits, I. Vayshenker, B. Baek, M. D. Shaw, R. P. Mirin, and S. W. Nam, "Detecting single infrared photons with 93% system efficiency," *Nature Photonics*, vol. 7, p. 210–214, 2013.

[177] F. Marsili, F. Bellei, F. Najafi, A. E. Dane, E. A. Dauler, R. J. Molnar, and K. K. Berggren, "Efficient Single Photon Detection from 500 nm to 5 μm Wavelength," *Nano Letter*, vol. 12, no. 9, p. 4799–4804, 2012.

[178] F. Najafi, A. Dane, F. Bellei, Q. Zhao, K. A. Sunter, A. N. McCaughan, and K. K. Berggren, "Fabrication Process Yielding Saturated Nanowire Single-Photon Detectors With 24-ps Jitter," *IEEE Journal of Selected Topics in Quantum Electronics*, vol. 21, no. 2, p. 1–7, 2015.

[179] G. N. Gol'tsman, O. Okunev, G. Chulkova, A. Lipatov, A. Semenov, K. Smirnov, B. Voronov, and A. Dzardanov, "Picosecond superconducting single-photon optical detector," *Applied Physics Letters*, vol. 79, p. 705, 2001.

[180] S. Ferrari, C. Schuck, and W. Pernice, "Waveguide-integrated superconducting nanowire single-photon detectors," *Nanophotonics*, vol. 7, no. 11, p. 1725–1758, 2018.

[181] J. P. Sprengers, A. Gaggero, D. Sahin, S. Jahanmirinejad, G. Frucci, F. Mattioli, R. Leoni, J. Beetz, M. Lermer, M. Kamp, S. Höfling, R. Sanjines, and A. Fiore, "Waveguide superconducting single-photon detectors for integrated quantum photonic circuits," *Applied Physics Letters*, vol. 99, p. 181110, 2011.

[182] H. Bernien, L. Childress, L. Robledo, M. Markham, D. Twitchen, and R. Hanson, "Two-Photon Quantum Interference from Separate Nitrogen Vacancy Centers in Diamond," *Physical Review Letters*, vol. 108, no. 4, p. 043604, 2012.

[183] A. Sipahigil, M. L. Goldman, E. Togan, Y. Chu, M. Markham, D. J. Twitchen, A. S. Zibrov, A. Kubanek, and M. D. Lukin, "Quantum Interference of Single Photons from Remote Nitrogen-Vacancy Centers in Diamond," *Physical Review Letters*, vol. 108, no. 14, p. 143601, 2012.

[184] S. Ferrari, V. Kovalyuk, W. Hartmann, A. Vetter, O. Kahl, C. Lee, A. Korneev, C. Rockstuhl, G. Gol'tsman, and W. Pernice, "Hot-spot relaxation time current dependence in niobium nitride waveguide-integrated superconducting nanowire single-photon detectors," *Optics Express*, vol. 25, no. 8, pp. 8739–8750, 2017.

[185] M. Stegmaier and W. H. P. Pernice, "Broadband directional coupling in aluminum nitride nanophotonic circuits," *Optics Express*, vol. 21, no. 6, pp. 7304–7315, 2013.

[186] S. Zhu and G.-Q. Lo, "Aluminum nitride electro-optic phase shifter for backend integration on silicon," *Optics Express*, vol. 24, no. 12, pp. 12501–12506, 2016.

[187] S. Ghosh and G. Piazza, "Piezoelectric actuation of aluminum nitride contour mode optomechanical resonators," *Optics Express*, vol. 23, no. 12, pp. 15477–15490, 2015.

[188] S. Molesky, Z. Lin, A. Y. Piggott, W. Jin, J. Vucković, and A. W. Rodriguez, "Inverse design in nanophotonics," *Nature Photonics*, vol. 12, p. 659–670, 2018.

[189] N. V. Proscia, Z. Shotan, H. Jayakumar, P. Reddy, C. Cohen, M. Dollar, A. Alkauskas, M. Doherty, C. A. Meriles, and V. M. Menon, "Near-deterministic activation of room-temperature quantum emitters in hexagonal boron nitride," *Optica*, vol. 5, no. 9, pp. 1128–1134, 2018.

[190] J. Kern, I. Niehues, P. Tonndorf, R. Schmidt, D. Wigger, R. Schneider, T. Stiehm, S. M. de Vasconcellos, D. E. Reiter, T. Kuhn, and R. Bratschitsch, "Nanoscale Positioning of Single-Photon Emitters in Atomically Thin WSe_2," *Advanced Materials*, vol. 28, no. 33, pp. 7101–7105, 2016.

[191] Y. Luo, G. D. Shepard, J. V. Ardelean, D. A. Rhodes, B. Kim, K. Barmak, J. C. Hone, and S. Strauf, "Deterministic coupling of site-controlled quantum emitters in monolayer WSe_2 to plasmonic nanocavities," *Nature Nanotechnology*, vol. 13, p. 1137–1142, 2018.

[192] J. E. Fröch, S. Kim, N. Mendelson, M. Kianinia, M. Toth, and I. Aharonovich, "Coupling Hexagonal Boron Nitride Quantum Emitters to Photonic Crystal Cavities," *ACS Nano*, vol. 14, no. 6, p. 7085–7091, 2020.

[193] S.-H. Bae, H. Kum, W. Kong, Y. Kim, C. Choi, B. Lee, P. Lin, Y. Park, and J. Kim, "Integration of bulk materials with two-dimensional materials for physical coupling and applications," *Nature Materials*, vol. 18, p. 550–560, 2019.